8-2010

Measurement, Simulation, and Analysis of the Mechanical Response of Railroad Track

Curt J. Greisen
University of Nebraska at Lincoln, curtgreisen@gmail.com

MEASUREMENT, SIMULATION, AND ANALYSIS OF THE MECHANICAL RESPONSE OF RAILROAD TRACK

by

Curt Greisen

A THESIS

Presented to the Faculty of

The Graduate College at the University of Nebraska

In Partial Fulfillment of Requirements

For the Degree of Master of Science

Major: Mechanical Engineering

Under the Supervision of Professor Shane M. Farritor

Lincoln, Nebraska

August, 2010

MEASUREMENT, SIMULATION, AND ANALYSIS OF THE MECHANICAL RESPONSE OF RAILROAD TRACK

Curt Greisen, M.S.

University of Nebraska, 2010

Adviser: Shane M. Farritor

Increased railroad traffic volumes, speeds, and axle loads have created a need to better measure track quality. Previous research has indicated that the vertical track deflection provides a meaningful indicator of track integrity. The measured deflection can be related to the bending stresses in the rail as well as characterize the mechanical response of the track.

This investigation summarizes the simulation, analysis and development of a measurement system at the University of Nebraska (UNL) to measure vertical track deflection in real-time from a car moving at revenue speeds. The UNL system operates continuously over long distances and in revenue service. Using a camera and two line lasers, the system establishes three points of the rail shape beneath the loaded wheels and over a distance of 10 ft. The resulting rail shape can then be related to the actual bending stress in the rail and estimate the track support through beam theory.

Finite element simulations are used to characterize the track response as related to the UNL measurement system. The results of field tests using bondable resistance strain gages illustrate the system's capability of approximating the actual rail bending stresses under load.

ACKNOWLEDGEMENT

I would like to thank my adviser, Dr. Shane Farritor, for his guidance, direction and support throughout the completion of my graduate study. Dr. Richard Arnold has been a valuable mentor and provided sound, practical advice. Dr. Sheng Lu and Haoliang Duan have been exceptional colleagues to work with. Beyond collaborating with me on my graduate project, they have shared their culture for which I will always be grateful.

I would like to thank my parents for their ongoing support. They have made my entire education possible and have provided a strong foundation for my life. My siblings also deserve credit for shaping my character and setting the bar high.

This work has been performed under a grant from the Federal Railway Administration (FRA). Special thanks are extended to Union Pacific Railroad and BNSF Railway for operational support and track access for testing.

Table of Contents

LIST OF FIGURES

Chapter 1, INTRODUCTION

Spanning back to the middle of the 19th century, railways have been a staple of both freight and passenger transportation. This dependency on rail traffic is expected to continue into the foreseeable future. Considering the recent emphasis on fuel efficiency, no other mode of transportation provides greater benefits. For example, one gallon of diesel fuel can move one ton of freight an average of 406 miles by rail (UPRR, 2006).

In order to attain greater efficiencies and to compensate for increasing customer demands, the railroad industry has increased traffic and moved toward higher speed trains with heavier axle loads. The resulting effect on the infrastructure is higher rail stresses and a corresponding increase in track deterioration. Therefore, improved maintenance procedures as well as a better understanding of the track response are needed.

Several variables influence the condition of railroad track. Rail profile, internal rail defects, rail stress, cross-level, gage, gage restraint, and track modulus are just some of the factors that shape the overall quality of the track (Kerr, 2003). Many of these parameters are interrelated and a decline in one can lead to a corresponding effect in the others. Therefore, both measurement and simulation of how the track state is affected by each of these quantities has become a priority in the railroad industry.

Since manual inspection methods are capable of covering only short specified distances and require track downtime, automation has become necessary for the determination of the track state. Therefore, automated systems have been developed to measure most of the track parameters (Li et al., 2002). For example, the Federal Railroad Administration's (FRA) T-18 high-speed track geometry vehicle is capable of collecting

data at speeds up to 50 mph (FRA, 2006). Such systems not only identify areas of needed maintenance but also provide the input necessary to create realistic and useful computer simulations of rail/vehicle dynamics (Hogan et al., 2008; Klauser, 2007).

Despite advances in automated track measurement, no vehicle is currently capable of measuring the vertical track support at revenue speeds. Yet, the quality of the vertical track support and its variation over a length of track is widely considered to be one of the most important indicators of track quality (Sussman et al., 2001). Most often, this support is described by the vertical track modulus. Track modulus is defined as the coefficient of proportionality between the rail deflection and the vertical contact pressure between the rail base and the track foundation. The track modulus represents the effects of all the track components beneath the rail (Cai et al., 1994). These components include the subgrade, ballast, subballast, ties, and tie fasteners.

Previous investigations have shown that the determination of track modulus is possible by measuring the deflection of the track under known loads (Kerr, 2003). Although most methods rely on static measurements, at least one system has been developed to operate with a moving vehicle (Thompson & Li, 2002). Unfortunately, the slow speed and high cost associated with the operation of this vehicle has limited its usefulness. However, a new system developed over the past few years at the University of Nebraska (UNL) and sponsored by the FRA has shown the ability to successfully measure vertical track deflection in real-time from a car moving at revenue speeds.

The UNL system measures the rail height relative to the line created by the wheel/rail contact points. Using a non-contact vision sensor system, it establishes three points of the rail shape beneath the loaded wheels and over a distance of 10 ft. This

direct measurement of the rail shape can then be used to determine important information regarding the track and its support. Primarily, the vertical track modulus can be related to the UNL deflection measurement through elastic foundation models. Furthermore, since the rail shape is determined at the location of high bending stress beneath the loaded wheels, the measurement can be mapped into rail bending stress through the rail curvature and beam theory.

This thesis summarizes the simulation, development and usefulness of the UNL system for measuring vertical track response. The relationship between the UNL deflection measurement and the actual bending stress in the rail is developed and described in detail. Validation of this association is performed through field tests using the UNL system along with bondable resistance strain gages attached to the rail flange. Finite element simulations are used to characterize the track response from the perspective of the UNL measurement. These simulations indicate that the UNL system is capable of distinguishing between several types of track support and geometry problems.

Chapter 2, BACKGROUND

Track quality and the parameters influencing it have been increasingly scrutinized as the railroad industry strives to meet consumer demands. Although the evolution of track geometry vehicles has allowed for a thorough inspection of the geometrical defects of the rail, an important piece of the puzzle remains missing. A valid method to measure and characterize the underlying track support would provide a missing tool in track design and maintenance. In fact, previous research has shown that the locations of poor track support and geometry profile often coincide (Sussman et al., 2001). Understanding the track support and how it relates to track response may provide for better maintenance methods and techniques to augment current practices.

Several mathematical models have been derived in an attempt to describe the relationship between the load and deflection of the railroad track (Kerr, 1964; Hetényi, 1946). In spite of their limitations, these models have historically been used to characterize the track support modulus. A brief outline of these models is presented followed by a summary of the methods used to measure track response.

2.1 Problem Definition

Analyzing track response requires some form of mathematical model. Such models are needed for analytical calculations as well as relating field measurements to physical parameters associated with the track. Most mathematical models for characterizing railroad track response have a basis in the bending theory of an elastic beam.

The bending theory of an elastic beam can be described by considering an infinite, continuous beam supported by an elastic foundation and subjected to a single point load.

This situation is similar to that of a railroad track under a single wheel load as illustrated in Figure 2-1.

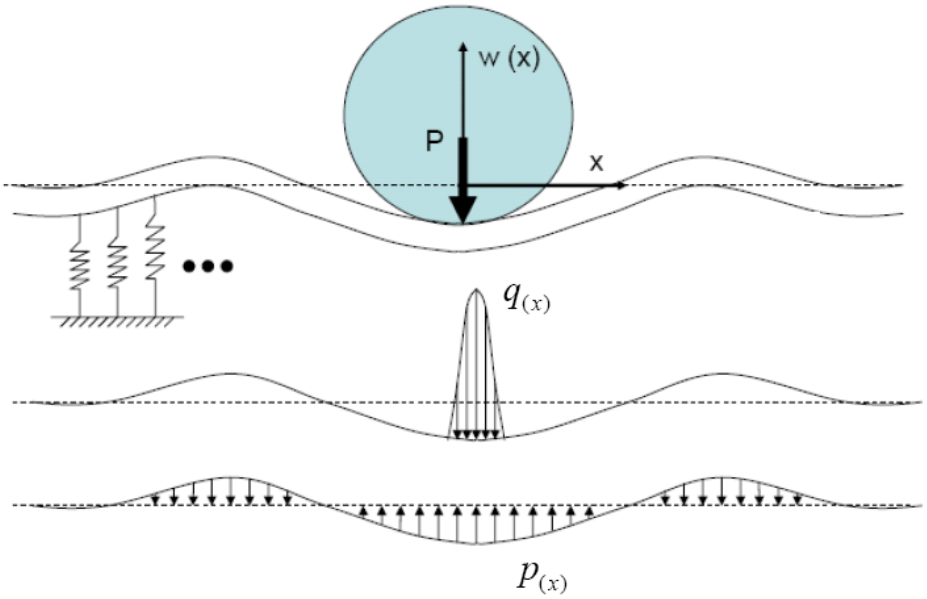

Figure 2-1. Track response under one-wheel load (Lu et al., 2007).

Here the track support is modeled as a series of continuous, independent springs. The differential equation describing this situation is given by:

$$EI\frac{d^4w}{dx^4} + p(x) = q(x) \qquad \text{Equation 2-1}$$

Initially for longitudinal tie tracks, *EI* represented the combined flexural rigidity of the rail and the longitudinal tie, *w(x)* represented the vertical beam (rail) deflection at location *x*, *q(x)* represented the vertical wheel load, and *p(x)* represented the continuous foundation reaction distributed force. A detailed derivation of Equation 2-1 can be found in Hetényi, 1946. For crosstie tracks, *EI* represents the flexural rigidity of the rail alone.

2.2 Winkler Track Model

The simplest track model based on Equation 2-1 is attributed to Winkler, who proposed that the distributed reaction force of the track foundation is linearly proportional to the vertical rail deflection. With this assumption, Equation 2-1 becomes:

$$EI\frac{d^4w}{dx^4} + uw(x) = q(x) \qquad \text{Equation 2-2}$$

This equation can be solved for the response of the track to a given load. The free-body diagram illustrating the load representation is shown in Figure 2-2.

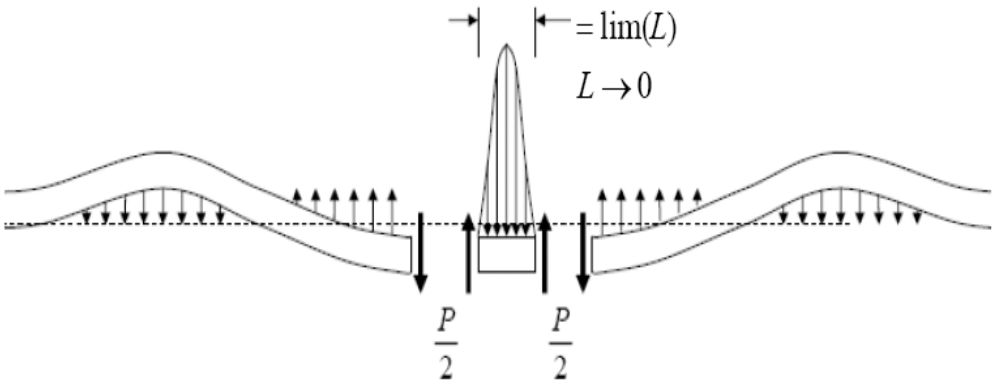

Figure 2-2. Free body diagram for Winkler model (Lu et al., 2007).

Four boundary conditions defined by the following equations are used to solve this fourth-order linear differential equation:

$$w(\pm\infty) = 0 \qquad \text{Equation 2-3}$$

$$\left.\frac{dw}{dx}\right|_{x=0} = 0 \qquad \text{Equation 2-4}$$

$$\int_0^\infty p(x)dx = \frac{P}{2} \qquad \text{Equation 2-5}$$

Applying these boundary conditions, Equation 2-2 can be solved for the vertical deflection along the length of the track. The resulting expression is shown in Equation 2-6.

$$w(x) = -\frac{P\beta}{2u} e^{-\beta|x|} \left[\cos(\beta|x| + \sin(\beta|x|)\right] \qquad \text{Equation 2-6}$$

where: $\beta = \sqrt[4]{\frac{u}{4EI}}$ Equation 2-7

P is the load on the track

u is the track modulus

E is the modulus of elasticity of the rail

I is the second moment of area of the rail section

x is the longitudinal distance along the track

The expression in Equation 2-6 is plotted for a range of modulus values as shown in Figure 2-3. In this case, the flexural rigidity of 132 lb rail is used with a typical coal hopper wheel load of 32,500 lb. Apparent in the figure is the fact that the rail deflects more with a decrease in modulus. What may not be obvious by intuition, however, is that the rail actually lifts up from its original position over sections of track some distance away from the application of the load. This phenomenon is observed in real track resulting in the loosening of cut spike fasteners (Kerr, 2003). One potential pitfall of the linear Winkler model is that the base foundation "pulls down" on the rail at these locations. The magnitude of this "pull down" effect is expected to be less in real track. Therefore, the rail lift may actually be greater than predicted by the Winkler model.

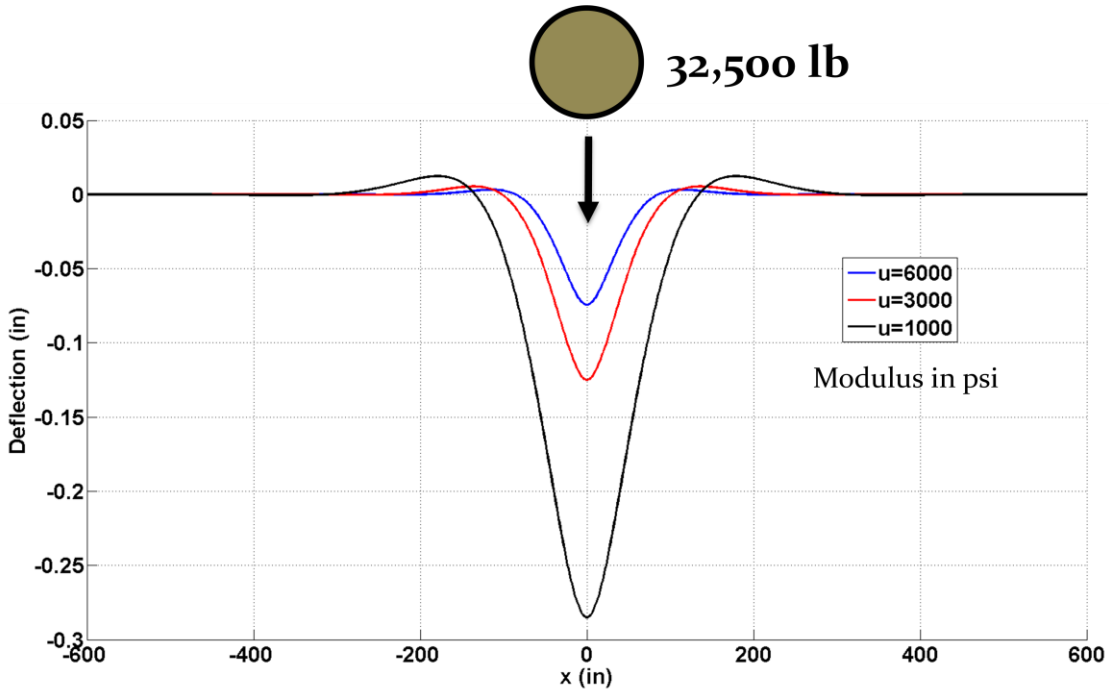

Figure 2-3. Winkler track model showing the effect of varying modulus.

The linearity of the Winkler model allows for the combination of multiple axle loads through the property of superposition. This is particularly useful for rail track analysis since loading conditions usually include a number of adjacent axles. The influence of multiple axles is obvious as displayed in Figure 2-4. In particular, the overall deflection increases while the location of maximum deflection moves slightly away from the points of load application. The multiple-axle trucks on the same car seem to have little effect on one another. However, trucks between adjacent cars have enough interaction such that they should be included in the analysis.

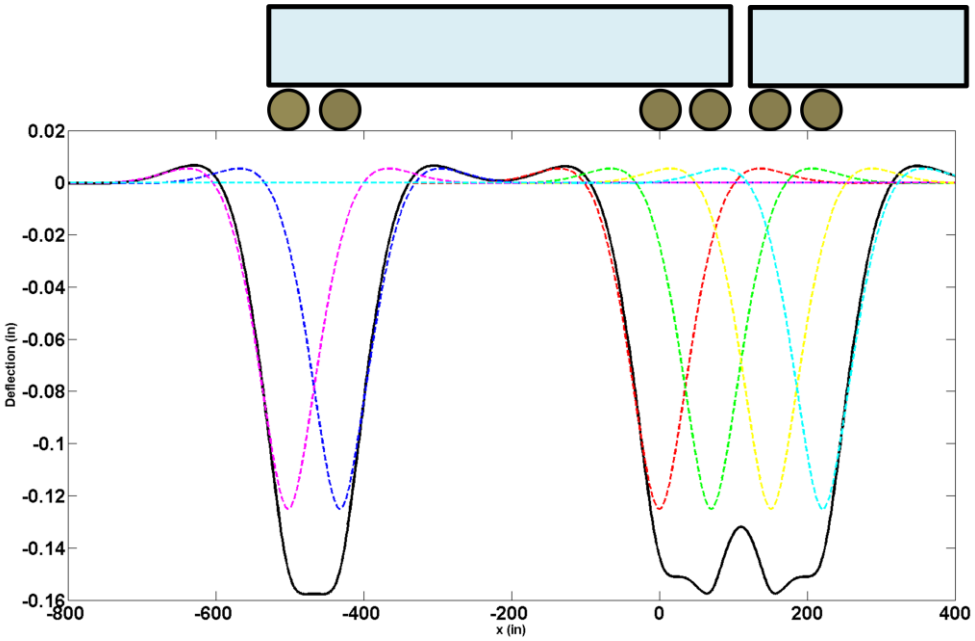

Figure 2-4. Superposition of loads in Winkler model.

Despite the usefulness of superposition for railway analysis, it is widely accepted that the track response is nonlinear (Sussman et al., 2001; Lu, 2008). This limitation and the fact that the spring elements in the foundation act independently have led to the formulation of several additional track models (Kerr, 1964).

2.3 Alternative Track Models

Several alternative track and foundation models have been developed through the years (Kerr, 1964). Some of these were developed as extensions of the Winkler model while others used distinct approaches. The Pasternak foundation was an extension of the Winkler model where shear interactions were included between the vertical spring elements. This introduced a second modulus term, the "shear modulus" *G*. Viscous elements were later added to create a viscoelastic Pasternak foundation.

Discrete foundation models have also been created (Norman, 2004). The advantage of a discrete model is that it allows variation of the stiffness from support to

support (tie to tie) along the foundation. Such variation replicates measured data, which indicates that the support modulus can change significantly over short distances of railroad track (Ebersöhn & Selig, 1994; Lu, 2008).

In order to introduce the nonlinearity of the track foundation, a cubic approach was adopted for use with the bending theory of an elastic beam (Lu, 2008). This model found its basis by determining that a cubic polynomial provided excellent agreement with experimental measurements of track deflection as shown in Figure 2-5.

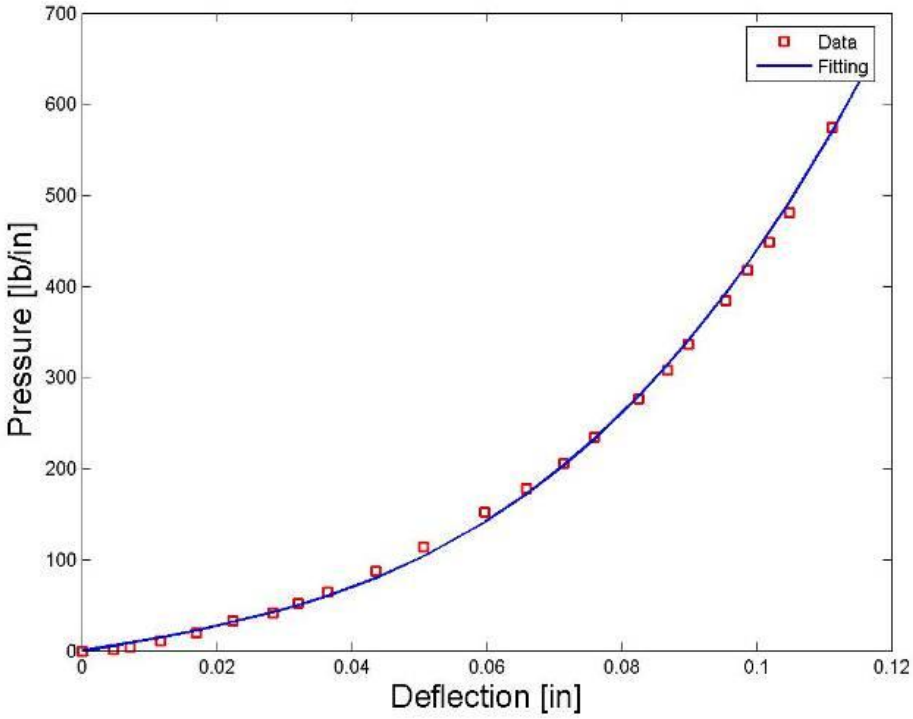

Figure 2-5. Empirical data (Zarembski & Choros, 1980) with cubic curve fit (Lu, 2008).

A new expression was then proposed for the foundation reaction distributed force:

$$p(x) = u_1 w(x) + u_3 w^3(x) \qquad \text{Equation 2-8}$$

Substituting this expression into Equation 2-1 yields the following differential equation for the track foundation:

$$EI\frac{d^4w}{dx^4} + u_1 w + u_3 w^3 = q \qquad \text{Equation 2-9}$$

Equation 2-9 is a nonlinear differential equation and a closed-form solution is not straightforward. However, numerical techniques such as the "bvp4c" function in MATLAB® have been used to obtain a solution (Lu, 2008). The results indicate several advantages over the Winkler model. For example, the deflection more closely represents real measurements where the track deflects more under an initially soft support due to slack and voids in the foundation. Further deflection results in stiffening of the foundation, which is typical of real track. Additional improvements are that track lift is not deterred by the foundation pulling down on the rail with significant force. The main disadvantages are that superposition is no longer valid and the current solution is limited to only one axle load.

Further progress has been achieved through models based on finite element analysis (FEA). These models add further complexity while taking advantage of computing resources to create more realistic representations of the track. Typical FEA models solve for the relationship between nodal displacements and applied forces by using differential equations or energy theorems. One custom FEA program, titled GBEAM, displayed the usefulness of this method by considering dynamic effects on the track model (Carr, 1999). The results indicate that above certain train speeds dynamic effects should not be ignored in the track response.

Despite the numerous models available, each track foundation representation seems to have limitations. Although FEA models provide greater complexity, their implementation and scale is limited by the computing power available (Chang et al., 1980). Therefore, FEA models seem to be developed with regard to their specific use

and are limited in their generality. For the purpose of track modulus measurement, the industry has leaned toward methods based on the Winkler approach (Kerr, 2003). Even commercial simulation programs such as Vampire® rail vehicle dynamic software have opted for rather simple track models based on individual springs interacting with the vehicle masses (Hogan, 2007; Klauser, 2007).

2.4 Measurement of Track Response

Analytical models provide a great tool for the design of railroad track and are a means to better understand the track response under loads. However, to truly identify with real track mechanics, empirical measurements of the track response are required. Traditionally, vertical track deflection has been used to characterize the track support and corresponding response to loads (Kerr, 2003). Studies have shown that deflection measurements related to the vertical track modulus can provide an important tool for track maintenance (Lu, 2008; Priest & Powrie, 2009; Ebersöhn & Selig, 1994). Currently accepted methods rely mainly on static measurements to determine the vertical modulus of a short section of track.

The simplest of the static methods is the Beam on Elastic Foundation (BOEF) Method. In this case, the vertical deflection of the track is measured at the location of a known applied load. This essentially provides a stiffness measurement, which can be related to the track modulus using the Winkler model (Cai et al., 1994). The resulting expression for the track modulus is given by:

$$u = \frac{1}{4}\left(\frac{1}{EI}\right)^{\frac{1}{3}}\left(\frac{P}{w_0}\right)^{\frac{4}{3}} \qquad \text{Equation 2-10}$$

where: u is the track modulus

E is the modulus of elasticity of the rail

I is the moment of inertia of the rail

P is the load applied to the track

w_0 is the deflection of the rail at the loading point

Although this method has been suggested as the best technique for field measurement (Zarembski & Choros, 1980), it has several limitations. The method relies on the Winkler model, which does not capture the nonlinear behavior of real track. In addition, the single measurement does not consider the large variations in modulus that occur over relatively short distances of track. Conducting manual measurements of this type over long sections of track is unreasonable and would require unacceptable track downtime.

Another static method that has been widely used to determine track modulus is the Deflection Basin Method, represented in Figure 2-6. This technique considers the vertical equilibrium of the rail under an applied load. The applied load can be shown to be proportional to the integral of the area formed by the deflected rail (Cai et al., 1994). This is represented as:

$$P - \int_{-\infty}^{+\infty} uw(x)dx = 0 \qquad \text{Equation 2-11}$$

In the field, the deflections are often measured at the tie locations, and the sum of the applied loads is used in the equilibrium equation to determine the support modulus (Kerr, 2003). The resulting expression for modulus becomes:

$$u = \frac{\sum P}{a\sum_{i=1}^{m} w_i(x)}$$ Equation 2-12

where: u is the track modulus

ΣP is the sum of the applied loads

a is the tie spacing

$w_i(x)$ is the rail deflection at each tie location

m is the number of ties in the deflected region

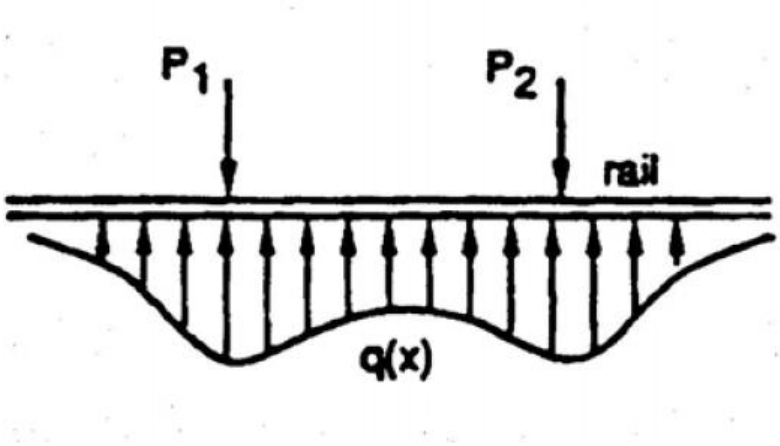

Figure 2-6. Deflection Basin Method (Selig & Li, 1994).

Some researchers have challenged the validity of the Deflection Basin Method due to some questionable assumptions. They dispute the belief that light wheel loads can be used to eliminate slack along the entire track section affected as recommended in (Cai et al., 1994). The assumption that the tie deflections are directly proportional to the loading is also contested by the same investigation (Kerr & Shenton, 1985). Furthermore, the method requires a multitude of displacement measurements that makes it tedious and

time-consuming. As a result, the method is not very conducive to maintenance planning covering numerous miles of track.

One proposed solution that attempts to account for the nonlinear track behavior is the Heavy/Light Load Method. This technique is similar to the BOEF method with two separate loads applied. The method allows for a piecewise-linear representation of the track response as shown in Figure 2-7.

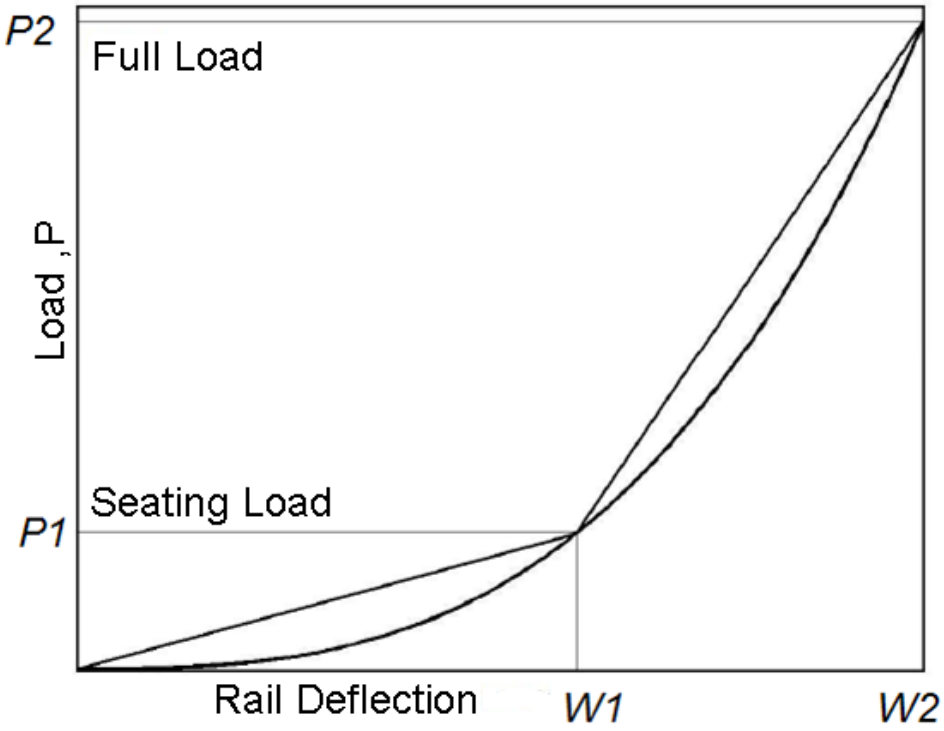

Figure 2-7. Piecewise-linear representation of track response (Lu, 2008).

The resulting expression for the track stiffness, which can be related to modulus through the Winkler model, is given by:

$$k = \frac{P_2 - P_1}{w_2 - w_1} \qquad \text{Equation 2-13}$$

where: k is the track stiffness

P_i are the applied loads

w_i are the corresponding deflections

The obvious weakness of this approach is apparent from Figure 2-7. The selection of the two applied loads will undoubtedly affect the results of the piecewise approximation of the track response. Similar to the other static measurements, this method results in fouling of the track and requires too much time and resources to become a valid inspection tool.

Automated track modulus measurement systems have been attempted and suggested as a way to gather information regarding track support for maintenance and planning. One system that has been successfully applied, although not widely implemented, is the Track Loading Vehicle (TLV) operated by the Transportation Technology Center Inc. (TTCI) (Thompson & Li, 2002). The system applies loads ranging from 4.45 kN to 267 kN (1 to 60 kips) while traveling at speeds up to 16.1 km/hr (10 mph). Center-load bogies located on each of two cars apply the loads. The leading vehicle applies a light load of 13.3 kN (3 kips) while the trailing vehicle applies 44.5 kN (10 kips) on a first pass and then 178 kN (40 kips) on a second pass over a single section of track. Laser-based systems on each vehicle measure the track deflections associated with the applied loads.

The limitations of the TLV have restricted its use. Due to its slow speed and the requirement of two passes over the same section of track, the TLV offers only minor gains over static measurements. Significant expense and personnel are also required to operate the vehicle.

Another automated system that has been proposed but not built was suggested based on walking-beam techniques developed by the military and used in highway research. The suggested system would employ standard freight car trucks as the reference systems to record deflection measurements of a third loaded axle. Similar to the TLV, both a heavy and light load would be applied but apparently in such a fashion that only one vehicle and one pass would be necessary. An optical system in conjunction with a laser beam would be used to record the deflection of a target mounted to the loaded wheel (Carr, 1999).

Disadvantages associated with the hypothetical model are the requirement that each reference truck would need to follow an identical path (Carr, 1999). Such a necessity means that special cylindrical wheelsets would have to be fabricated. Furthermore, the system requires specially loaded axles in contact with the rails, which would require the construction of a custom vehicle. Such a contact measurement system could also be limited in speed and functionality.

Over the past few years, UNL has developed a system to measure vertical track deflection that overcomes many of the pitfalls found in previous measurement techniques. The system uses non-contact laser beams in conjunction with a camera to determine the rail displacement relative to the wheel/rail contact point. Measurements are made from a modified hopper car in real-time while traveling at revenue speeds. The non-invasive, robust operation of the UNL system makes it superior to previously proposed methods of track deflection measurement.

The principal goal of the UNL system is to use the track deflection measurements to identify locations of poor track support. However, studies suggest that a wealth of

additional information regarding the track condition may be gleaned from the UNL data. Vertical track modulus may be derived from the primary measurement using the Winkler or cubic models (Lu, 2008). Dynamic rail vehicle simulations may be improved when used in conjunction with data from the UNL system (Hogan et al., 2008; Hogan, 2007). Furthermore, the actual bending stress in the rails can be approximated through extension of the bending theory of an elastic beam (Greisen et al., 2009).

2.5 Stress in Rails

Complex loading conditions lead to the stress distribution found in railroad rails. Cyclic wheel loads, temperature-induced longitudinal loads, and shear loads caused by the wheels and ties combine to create the compound stress environment found in the rails. Rail cant and gage widening further lead to eccentric and unusual forces on the rails. Despite the multitude of factors, cyclic axial forces most often govern the rail stresses leading to crack growth and fatigue failure.

Axial stresses primarily develop from temperature-based longitudinal stress, bending stresses from the wheel loads, and contact stresses from the wheel/rail contact patch. The contact stress can be estimated based on the typical wheel loads on a given track by considering known tonnage rates. Unfortunately, temperature-based stresses and bending stresses are much more difficult to determine. Each of these two stress factors can independently lead to rail failure.

Flexural bending stress has historically been recognized as one of the main causes of fatigue failures in rail. Therefore, much emphasis has been placed on an expanded understanding of stress related rail failure. The Association of American Railroads (AAR) has developed theoretical equations for combining flexural bending stress, Hertzian

contact stress and longitudinal thermal stress with the classical fatigue theory of the Modified Goodman Diagram (Spotts et al., 2004). Further modeling has been completed with computer programs developed by the AAR to analyze rail stresses (Steele & Muhlenberg, 1992; Steele & Joerms, 1988).

The theoretical models and programs developed by the AAR as well as testing conducted by TTCI have led to an overall increase in rail stress knowledge. However, each model requires input concerning the rail stresses. Therefore, any calculations based on these models will be limited by the details known about actual rail stresses. Unfortunately, data concerning bending stresses over significant amounts of actual track are limited.

The vertical track deflection measurement system developed by UNL has shown the capability to autonomously collect data over hundreds of miles of heavy-haul track in revenue service (Lu, 2008). The relationship between data measured by the UNL system and the actual rail bending stress is developed in a later chapter of this thesis investigation. Such a relationship, which has been validated with field measurements, provides important information for modeling, design and maintenance work concerning stresses in rails.

Chapter 3, UNL MEASUREMENT SYSTEM

Experts agree that continuous measurement of track support over vast distances would provide a significant addition to the maintenance tools available to railroad personnel (Sussman et al., 2001; Ebersöhn et al., 1993; Carr 1999). However, as discussed in Chapter 2, methods for collecting data concerning track support conditions over many miles of track are currently unavailable. Over the past few years, UNL has developed a system to measure vertical track deflection autonomously from a moving railcar traveling at revenue speeds. This measurement system has successfully conducted tests over hundreds of miles of track and has preemptively identified several derailment locations (Lu, 2008). The following chapter discusses the UNL method of measurement and recent improvements to the system.

3.1 Method of Measurement

The UNL measurement system uses cameras and line lasers mounted to a stable reference frame to determine the vertical deflection of the rail. The following sections describe how this system is implemented on a modified hopper car to create a robust, autonomous measurement system for recording the response of the railroad track under typical loading conditions.

3.1.1 Sensor Geometry & Output

Deflection of the rail is recorded relative to the wheel/rail contact point as shown in Figure 3-1. The instrumentation enclosure is mounted so that the sensor reading is measured 48” away from the inboard axle of a modified hopper car. Included in the enclosure are a camera and two line lasers mounted at a fixed height, *H*, above the

wheel/rail contact line. Line lasers are used to compensate for any lateral movement of the instrumentation. This distance, *H*, can also be considered as the height of the sensors above a perfectly stiff rail with no deflection. As the rail deflects under load, the sensor system measures its new height, *h*, above the rail. The difference between the fixed height, *H*, and the varying height, *h*, is given by:

$$Yrel = H - h \qquad \text{Equation 3-1}$$

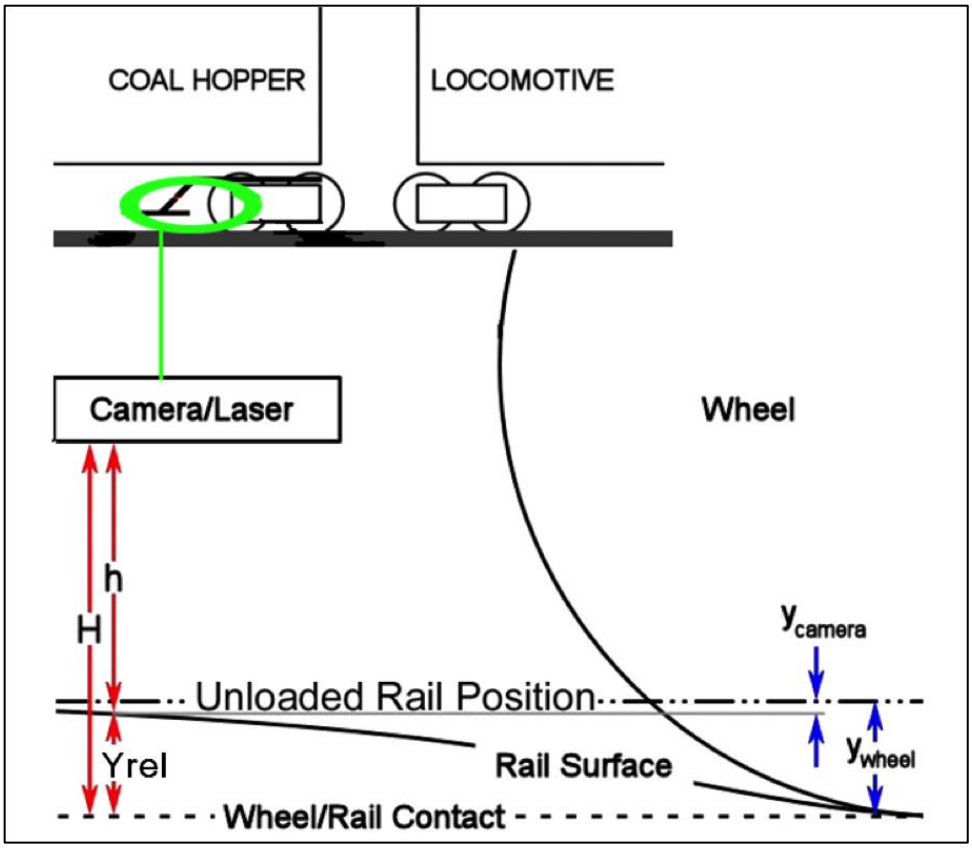

Figure 3-1. Schematic of UNL measurement method (Norman, 2004).

The track deflection is fully characterized by considering the other variables shown in Figure 3-1. The deflection of the rail directly beneath the camera/laser assembly is defined as y_{camera}, while the deflection directly beneath the wheel/rail contact point is y_{wheel}. This maximum deflection, y_{wheel}, at the wheel/rail contact point can be

related to the relative deflection, *Yrel*, using the Winkler track model. Before this can be completed, *Yrel* must be determined from the direct sensor measurement. As shown in Figure 3-2, the line lasers are projected at an acute angle toward the rail. The distance between the two line lasers, *d*, at their intersection with the rail provides the output needed to determine *Yrel*.

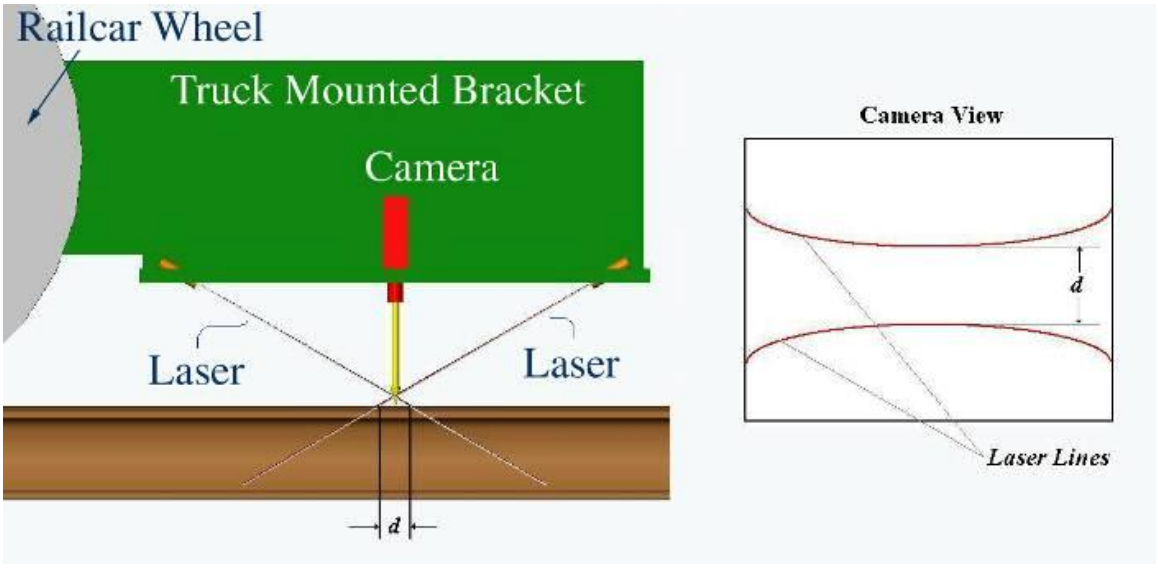

Figure 3-2. Camera and laser placement with ideal sensor image (Norman, 2004).

The camera captures an image of the line lasers intersecting with the rail. Curved lines appear in the image because of the curved profile of the railhead. The minimum distance, *d*, between the two laser lines can be related to the distance, *h*, by considering the geometry of the camera and lasers as shown in Figure 3-3.

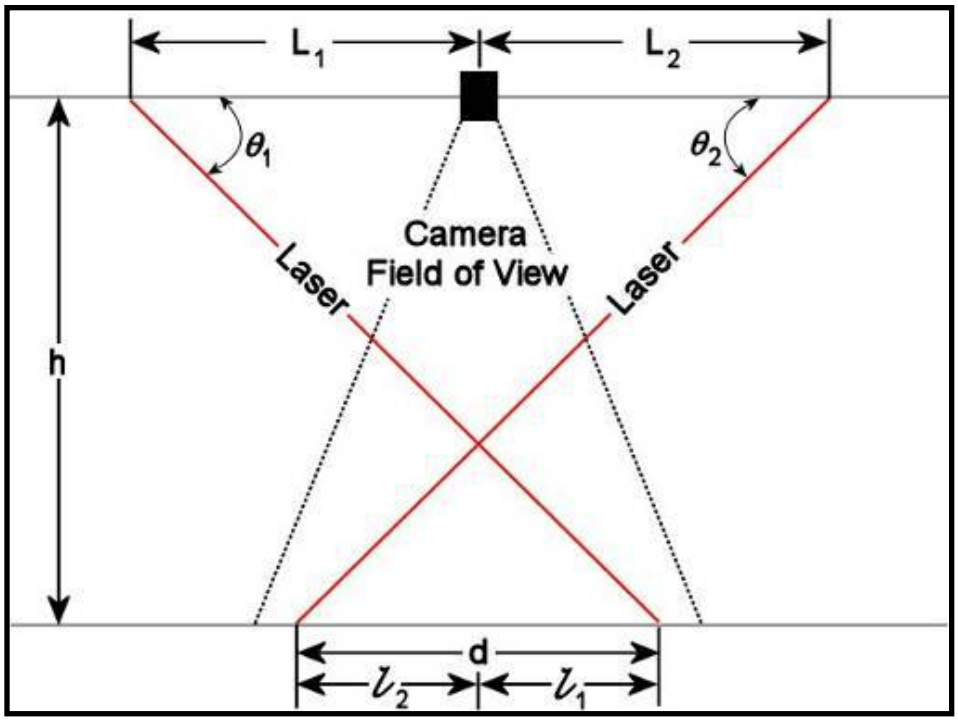

Figure 3-3. Geometry of sensor system (Norman, 2004).

The geometry of the system can be described with the following equations:

$$h = (L_1 + l_1)\tan\theta_1 \qquad \text{Equation 3-2}$$

$$h = (L_2 + l_2)\tan\theta_2 \qquad \text{Equation 3-3}$$

$$d = l_1 + l_2 \qquad \text{Equation 3-4}$$

In this case, the variables are defined by the geometry shown in Figure 3-3. An image-processing program determines the distance, *d*, between the laser lines in the camera image (Lu, 2008). The height of the sensor assembly above the rail is then found relative to this distance by solving the previous three equations for the following:

$$h = \frac{d + (L_1 + L_2)}{\cot\theta_1 + \cot\theta_2} \qquad \text{Equation 3-5}$$

Combining Equation 3-5 with Equation 3-1, the deflection of the rail relative to the wheel/rail contact line, *Yrel*, can be determined from the sensor system's output. On soft track, the rail will deflect more beneath the wheel/rail contact point such that the

sensor system moves closer to the rail and the distance between the laser lines decreases. In contrast, the laser lines will move further apart on stiffer track. Track modulus can then be estimated by considering the calculated relative deflection, *Yrel*, in conjunction with the Winkler track model.

3.1.2 Measurement Related to Vertical Track Modulus

The UNL measurement of *Yrel* can be related to the vertical track modulus, *u*, by applying the superposition property of the Winkler track model as shown in Figure 3-4.

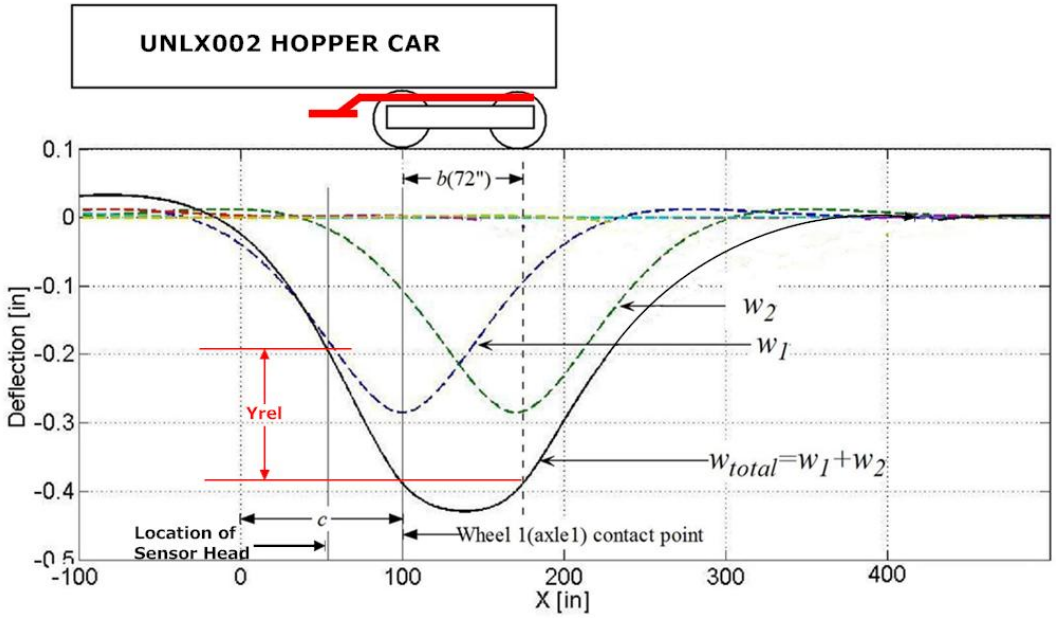

Figure 3-4. Determination of *Yrel* from the Winkler track model (Lu, 2008).

The modified hopper car used in the UNL measurement system has a known weight of approximately 262,000 lb. The distances between each axle and between the inboard axle and the sensor system are 70" and 48" respectively. Typically, the rail's second moment of area and Young's modulus for the particular track under consideration are known. This information can be substituted into the Winkler track model, which can then be solved for the deflection of the track as represented in Equation 2-6. Considering

only the two loads shown in Figure 3-4, superposition of the Winkler track deflection yields the following:

$$w_{total}(x) = w_1(x) + w_2(x) \qquad \text{Equation 3-6}$$

where $w_1(x)$ is the deflection due to axle 1

$w_2(x)$ is the deflection due to axle 2

The deflections beneath the sensor assembly and beneath the wheel/rail contact point are given by Equation 3-7 and Equation 3-8 respectively. Note that these expressions are relevant to the abscissa in Figure 3-4. The appropriate modifications must be made for a change in the reference axis.

$$w_{sensor} = w_{total}(x)\big|_{x=c-48"} \qquad \text{Equation 3-7}$$

$$w_{wheel/rail} = w_{total}(x)\big|_{x=c} \qquad \text{Equation 3-8}$$

Now, *Yrel* can be determined based on its definition and the calculated deflections, which yields the following:

$$Yrel = w_{wheel/rail} - w_{sensor} \qquad \text{Equation 3-9}$$

The explicit relationship between *Yrel* and track modulus, *u*, is more apparent by assuming a constant track modulus and expanding the previous equation to give:

$$\begin{aligned} Yrel = \frac{P\beta}{2u}\{1 + e^{-\beta b}\left[\cos(\beta b) + \sin(\beta b)\right] \\ - e^{-48"\beta}\left[\cos(48"\beta) + \sin(48"\beta)\right] \\ - e^{-\beta(b+48")}\left[\cos(\beta(b+48")) + \sin(\beta(b+48"))\right]\ \} \end{aligned} \qquad \text{Equation 3-10}$$

where $\beta = \left(\frac{u}{4EI}\right)^{\frac{1}{4}}$

Successive substitution of increasing modulus values into Equation 3-10 along with the known values of axle loads, geometry, and rail properties yields the graphical relationship between modulus and *Yrel* as shown in Figure 3-5. This data can be compiled into a look-up table that can be used to directly transform measured *Yrel* data into modulus approximations for a section of track.

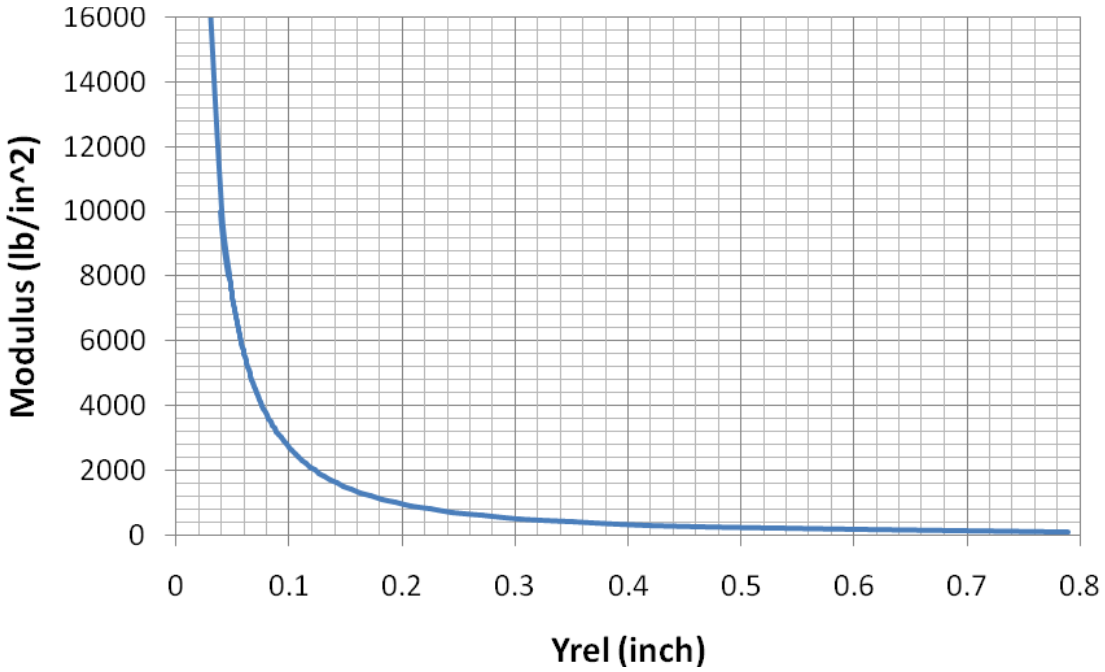

Figure 3-5. Relationship between Yrel and modulus from Winkler (Lu, 2008).

3.1.3 Eliminating Track Geometry Effects

The theoretical measurement of *Yrel* as shown in Figure 3-1 includes the basic assumption that the unloaded rail is perfectly straight. However, it is easy to speculate that some pre-existing geometry of the rail could affect the actual measured value of *Yrel* by the UNL system. Unloaded geometry variations such as those shown in Figure 3-6 can sometimes occur along mainline track. The effect of such vertical track variations must be accounted for to ensure the integrity of the vertical track deflection measurement.

Figure 3-6. Geometry variation in track profile.

In a previous investigation (Lu, 2008), a case study was performed to determine the effect of significant pre-existing rail geometry on the *Yrel* measurement. This analysis examined an existing site where the rail contained an unloaded dip of 0.5" over a length of 200". The study indicated that the total *Yrel* measurement included combined effects from the pre-existing geometry and actual track deflection due to poor support conditions. Using the Winkler model, the depth and length of an unloaded dip in the rail geometry was varied and the subsequent effect on *Yrel* was determined (Lu, 2008). The results of the investigation suggest that only large vertical geometry defects over a short distance contribute to the *Yrel* measurement and that both geometry and modulus defects are generally present for large values of *Yrel*.

Rail profile data supplied by track geometry measurement vehicles is used to isolate the track deflection measurement from pre-existing geometry effects. Track geometry vehicles measure various geometrical properties of the track including position, curvature, alignment, cross-level and profile, among others. The vertical rail profile is

determined with the use of multiple on-board, high-precision accelerometers. This data can be used to account for pre-existing geometry variations in the *Yrel* measurement.

The rail profile is used to calculate a 10 ft End Chord Offset (*ECO*) as shown in Figure 3-7. The calculation of *ECO* corresponds directly to the determination of *Yrel*, except that the rail profile, rather than the instantaneous rail shape, is used in the computation. Therefore, 70" is the spacing between the two truck axles (Figure 3-4) and 48" is the distance between the inboard axle and the location of the sensor assembly.

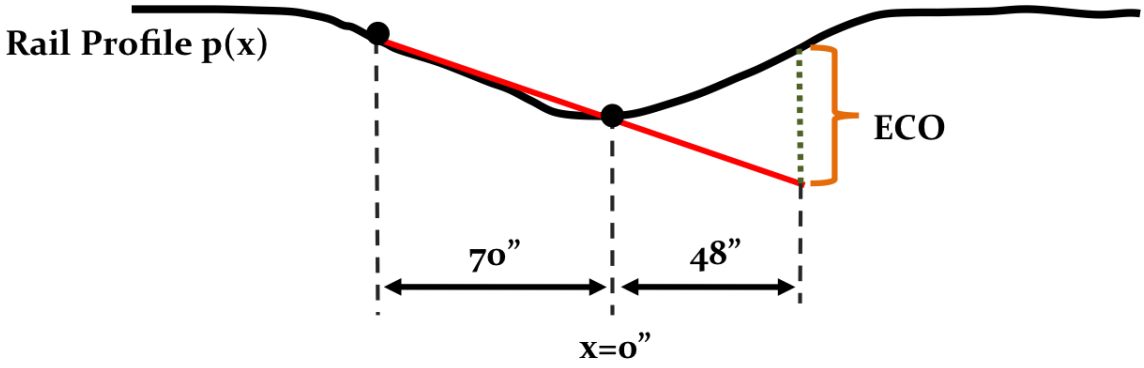

Figure 3-7. Calculating End Chord Offset (*ECO*) from rail profile.

Note that the *ECO* has been referenced over 10 ft when in actuality the chord extends over 9 ft, 10 in. This is done to simplify the calculation of *ECO* without any noticeable effect on the results. Assuming the axles are spaced 72" apart makes this simplification. Then, the expression for *ECO* is given by

$$ECO = \frac{5}{3}p(x) - \frac{2}{3}p(x-72") - p(x+48") \qquad \text{Equation 3-11}$$

where *p(x)* is the rail profile at the inboard axle

p(x-72") is the rail profile at the trailing axle

p(x+48") is the rail profile at the sensor assembly

The rail profile, *p(x)*, should not be confused with the instantaneous rail deflection as shown in Figure 3-8. In the figure, the axles travel from left to right. The rail profile is the loaded path traversed by both axles. The assumption that both axles follow the same path has been justified in previous investigations (Lu, 2008; Norman, 2004). For example, the leading axle is currently in position *p(x)*, the trailing axle is currently in position *p(x-70")*, and the sensor assembly is currently in position *p(x+48")*. After traveling another 48", the leading axle will be in position *p(x+48")*. The trailing axle will be in position *p(x)* after 70" of travel and *p(x+48")* after 118" of travel. Conversely, the instantaneous rail deflection, *w(x)*, defines the current rail shape. The instantaneous deflection matches the rail profile only at the location of the axles. Again, this is based on the assumption that both axles follow the same path. At every other location, the instantaneous deflection is typically different than the loaded rail profile.

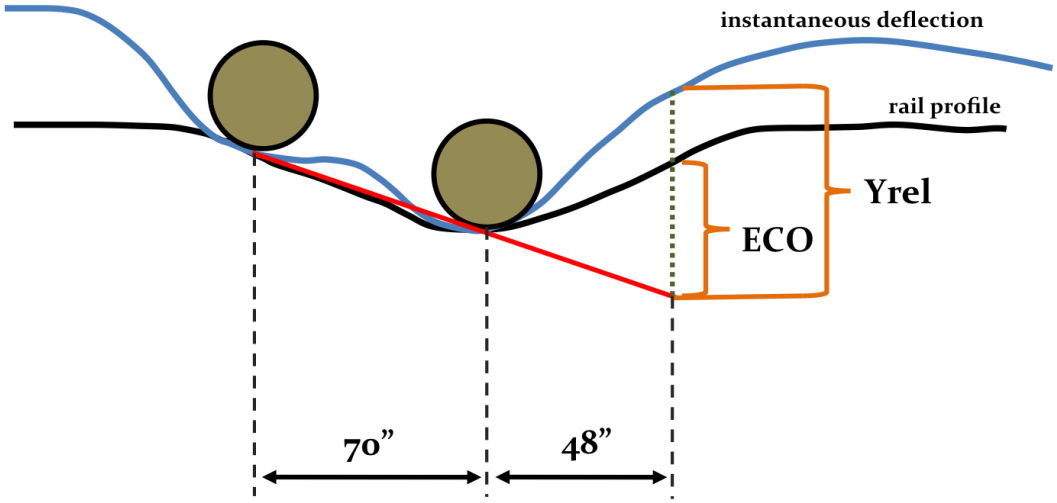

Figure 3-8. Relationship between Yrel and ECO.

The instantaneous rail deflection 48" ahead of the inboard axle, *w(x+48")*, will differ from the maximum, absolute deflection of the rail, *p(x+48")*, when the inboard

axle is actually at this location. The difference between these two deflections was derived in (Lu, 2008) and is defined as:

$$"Deflection" = Yrel - ECO \qquad \text{Equation 3-12}$$

In this equation, both *Yrel* and *ECO* are defined by the geometry shown in Figure 3-8. In other words, by this definition, both *Yrel* and *ECO* are positive when the chord extends beneath the rail and negative otherwise. The resulting value represents a relative deflection of the rail from partially loaded (when the axle is four feet away) to fully loaded (when the axle has advanced four feet).

The relationship between track deflection and track geometry is complex. Consolidating the preceding information, *Yrel* can be accounted for by two parts. The first part is the geometry contribution defined with *ECO*. The second part is the track deflection related to the vertical support modulus.

3.2 Instrumentation

The instrumentation for the UNL measurement system is mounted on a refurbished hopper car as shown in Figure 3-9. Sand is added to the covered hopper car in order to maintain a constant weight of 260,000 lb. The cover is used to prevent the collection of rainwater. The sensors themselves are supported from two (one above each rail) massive beams attached to the side frames of the trailing truck on the "A" end of the hopper car. Modification of the side frames is not required since the beams are clamped to the side frames and held firmly in place with high-durometer rubber padding. These rigid beams are painted red as shown in Figure 3-9.

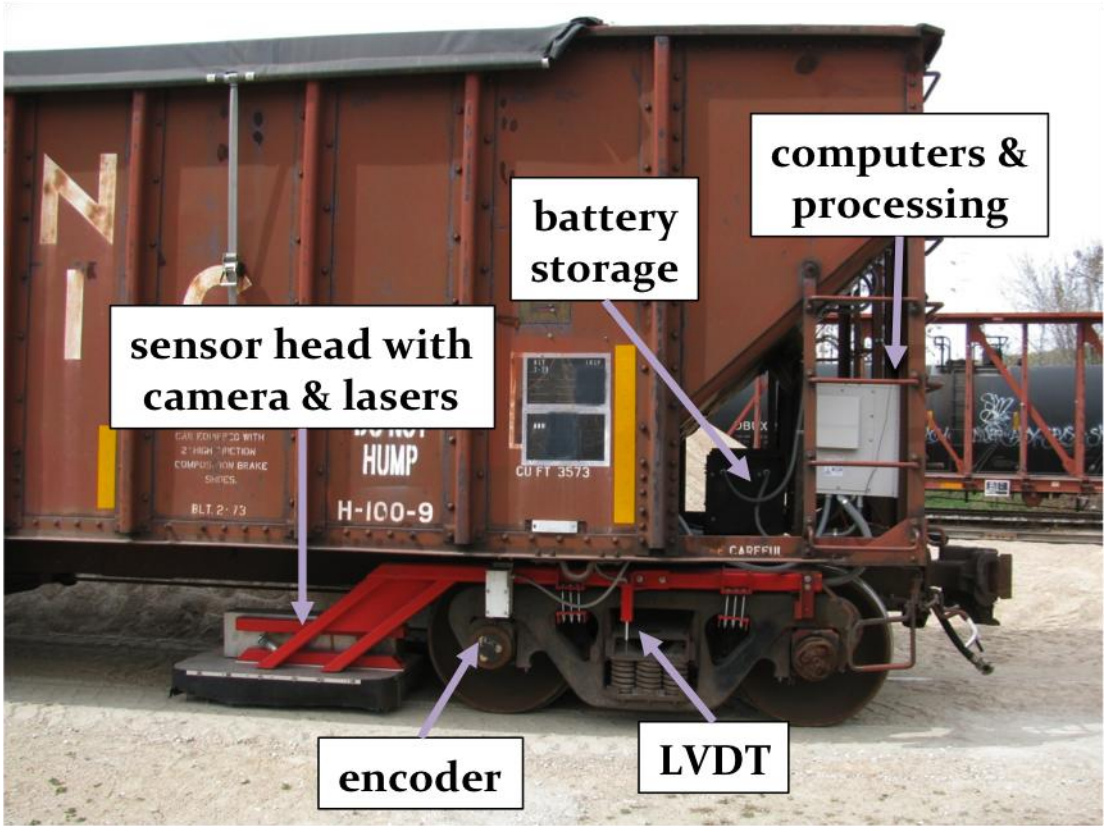

Figure 3-9. Instrumentation arrangement for UNL measurement system.

The system is comprised of the deflection measurement sensors, auxiliary measurement devices, power management, and onboard computational equipment. These components work together to make an accurate and repeatable vertical deflection measurement of the rail in real-time. Each of these elements is briefly described.

The deflection measurement sensors, consisting of a digital vision system and two line lasers, are enclosed in a sensor head bolted to the gage side of the red beam at a fixed distance from the inboard axle. Excessive ambient light distorts the camera image and may lead to inaccurate or erroneous measurements. Therefore, sunlight is shielded from the camera image with shrouds bolted to the bottom of the red beam as shown in Figure 3-9. The shrouds themselves consist of flexible, plastic landscaping material wrapped

around a frame of steel tubing. The top of the shroud frame is covered with stainless steel sheet metal.

Multiple mounting holes allow for positional adjustment of the camera and lasers inside the sensor head as shown in Figure 3-10. Separate mounting holes, rather than slots, ensure that the instruments are rigidly attached. The laser beams are projected at approximately 40 ° angles from the horizontal. These beams cross and subsequently create curves across the top surface of the rail as shown in the right image of Figure 3-10.

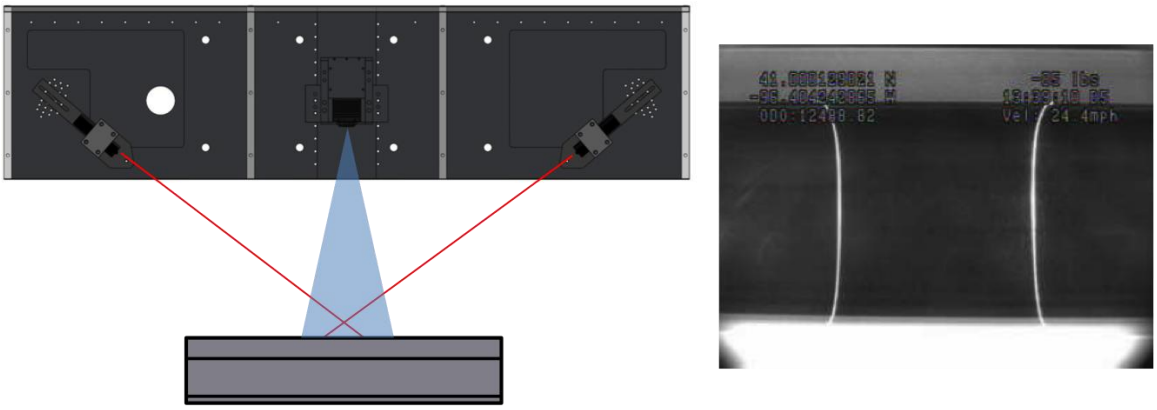

Figure 3-10. Sensor arrangement with resulting camera image.

The minimum distance between the curves in the real image shown in Figure 3-10 corresponds to the distance, *d*, defined earlier and illustrated in Figure 3-2 and Figure 3-3. The camera captures this image and an image-processing program is used to determine the minimum distance between the two curves (Lu, 2008). As described earlier, the distance between the laser lines is directly related to the vertical track deflection. On soft track, the rail deflects a greater amount and the laser lines move closer together. On stiff track, the rail does not deflect much and the laser lines are further apart.

Several auxiliary measurement devices are used to complement the vertical deflection measurement. These include an encoder, linear variable differential transformers (LVDT's) and accelerometers as shown in Figure 3-11. A global

positioning system (GPS) is also used with the corresponding antenna mounted to the top of the car as shown in Figure 3-12.

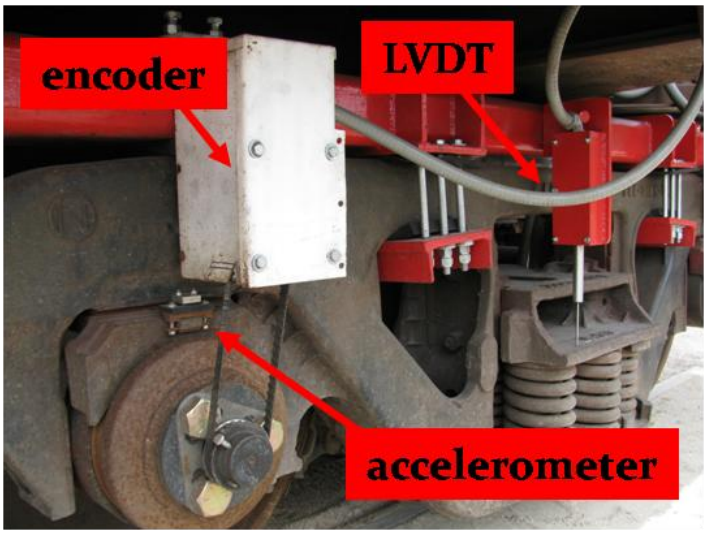

Figure 3-11. Auxiliary measurement devices on UNL system.

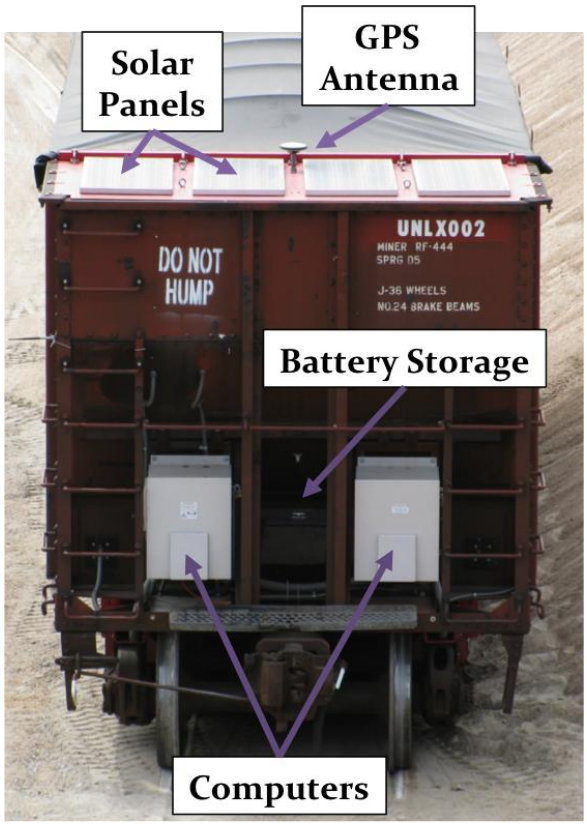

Figure 3-12. On-board computation, power supply, and GPS antenna.

The GPS receiver is located inside one of the sealed white Purcell® boxes mounted on the "A" end of the hopper car as displayed in Figure 3-12. The GPS adds real-time longitude and latitude data to the corresponding deflection measurements. This positional information is used to correlate milepost information with Precision Measurement Vehicle (PMV) data. Therefore, the location of measurement exceptions can be accurately identified. Any data that exceeds thresholds based on various criteria defined in section 3.4 qualifies as an exception. Exception locations usually correlate to poor track quality and are further investigated with site visits requiring accurate location information.

Error in the GPS data may lead to misalignment of the deflection data with the corresponding track mileposts. This alignment is needed to match the UNL measurements with PMV data and to locate exception sites. The exact magnitude of this error can vary depending on a variety of factors related to the satellite clock, signal delay, signal reception, and weather. The combined effects can lead to errors of up to 60 ft (Lu, 2008). Therefore, the encoder shown in Figure 3-11 was added to correct errors made by the GPS. In addition to improving the precision of the location data, the encoder has been used to wake the computers from sleep mode.

Linear variable differential transformers (LVDT's) are mounted to each red beam as displayed in Figure 3-11. The purpose of these devices is to determine the dynamic response of the car body during travel. They measure the car body roll by making a deflection measurement between the side frame of the truck and the bolster. This approach has been in development for several years without definitive results (McVey,

2006). However, the LVDT's and their mounting placement have recently been updated. Further field measurements and data processing are needed to verify their operation.

Another recent addition to the UNL system includes accelerometers mounted to the bearing adapters on each side of the inboard axle as shown in Figure 3-11. The accelerometers are Dytran Instruments 7500A5 variable capacitance models capable of measuring accelerations up to 50 g's. Their purpose is to record the vertical acceleration of the inboard axle. The vertical acceleration may then be filtered and integrated twice to determine the vertical rail profile needed to calculate *ECO*. This will ultimately eliminate the process of acquiring rail profile data from separate track geometry vehicles. Although current data processing has indicated the potential of these accelerometers, the results do not yet match track geometry profile data. Alternative mounting positions are under exploration to avoid the influence of vibration from the bearing adapters.

Onboard computation and data processing is completed with three rugged computers stored inside the sealed white Purcell® boxes mounted on the "A" end of the car. In addition to the computers, two data acquisition (DAQ) boards, two relays, and a wireless router are stored in the Purcell® boxes. Two of the computers are used to manage the digital vision systems and lasers for each rail. The third computer manages the auxiliary equipment including the LVDT's and accelerometers. The encoder data is read by a Rabbit 3000 micro-controller, also stored in the Purcell® box.

3.3 Additions & Improvements

Several additions and improvements have been made in recent years as part of the ongoing development of the UNL vertical track deflection measurement system. Some new and modified devices have been added as part of the auxiliary measurement

equipment already described. New LVDT's with a modified mounting configuration have been added as shown in Figure 3-11. The new LVDT's have a longer stroke than previous versions while the mounting configuration ensures direct contact of the piston with the bolster. Earlier versions required a second bracket mounted to the bolster. Excessive car body roll also presented the possibility of interference between the LVDT housing and bolster, which has been eliminated in the new design.

Accelerometers have also been mounted above the bearing adapters on the inboard axle as displayed in Figure 3-11. The goal of the accelerometers consists of determining the vertical space curve of each rail. The space curve data is needed to compute the *ECO* used to remove geometry effects in the vertical deflection measurement. Currently, separate track geometry vehicles operated by the railroad companies provide the space curve data. Incorporating this measurement into the UNL system would allow the geometry effects to be eliminated in real-time. Real-time measurement of the space curve eliminates the possibility of track variations between the time the UNL and track geometry car measurements are made. Further field-testing and data processing are needed to verify that the accelerometers can successfully reproduce the vertical space curve of each rail.

Additional improvements have been completed with the design of new red beams as shown in Figure 3-13. The original red beams were designed for use with a tank car, requiring the removal of material from the beam section (McVey, 2006) as shown in Figure 3-13 (b). Deterioration of the welds around the modified section of the red beams created a concern regarding their structural integrity. Since the beams are now mounted

on a modified hopper car, the removed material is no longer necessary. Therefore, the new beams have a continuous section as illustrated in Figure 3-13 (a).

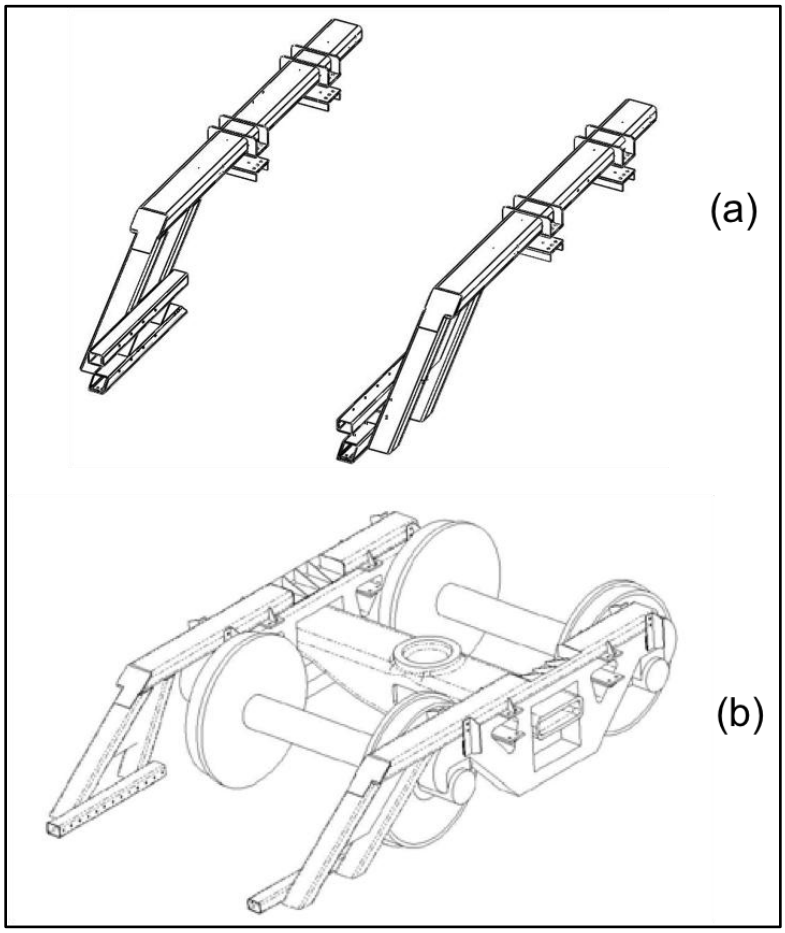

Figure 3-13. (a) Modified vs. (b) original red mounting beams.

Another modification to the red beams includes the new, continuously welded and gusseted mounting plates visible in Figure 3-13 (a). The original red beams employed small triangular gussets supporting the top mounting plate only, without any gussets supporting the bottom mounting plate. The addition of two more holes per mounting plate allows six, rather than four, half-inch bolts to clamp the red beams firmly to the side frames.

Several more modifications to the red beams make the system more robust while easing maintenance and troubleshooting tasks. The addition of a second horizontal member at the sensor head location eliminates the need for an extra adapter plate as shown in Figure 3-14. Previously, the sensor heads were not of the same construction. Fabrication of a new sensor head has made the system more uniform, modular, and quickly removable.

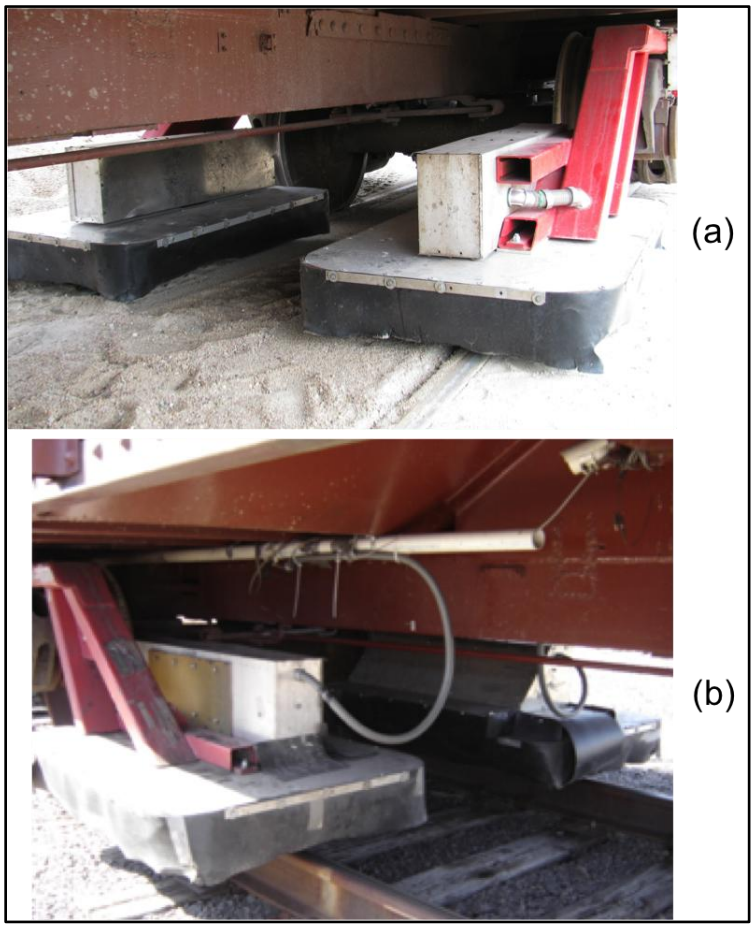

Figure 3-14. (a) Modified vs. (b) original sensor heads and conduit.

As displayed in Figure 3-14, even the electrical conduit has been updated. The original conduit was placed along the bottom of the hopper car and extended from a PVC pipe. The new conduit was enlarged from 1" to 2" and routed inside the red beam itself with a small section exposed going into the sensor head as shown in Figure 3-14 (a).

These improvements allow wiring with larger connectors while minimizing weathering effects and external damage.

Recently, the shroud design was updated as shown in Figure 3-15. The shroud on the right beam illustrates the modified design while the shroud on the left beam represents the original shroud structure. Both existing shrouds have been remade to match the updated version. The changes included reduction of the shroud width by eight inches and the addition of two gusseted brackets at the front and rear ends of the shroud. The overall effect results in less overall weight and less weight cantilevered away from the mounting bolts underneath the red beam. The gussets provide further structural stability and reduce vibration.

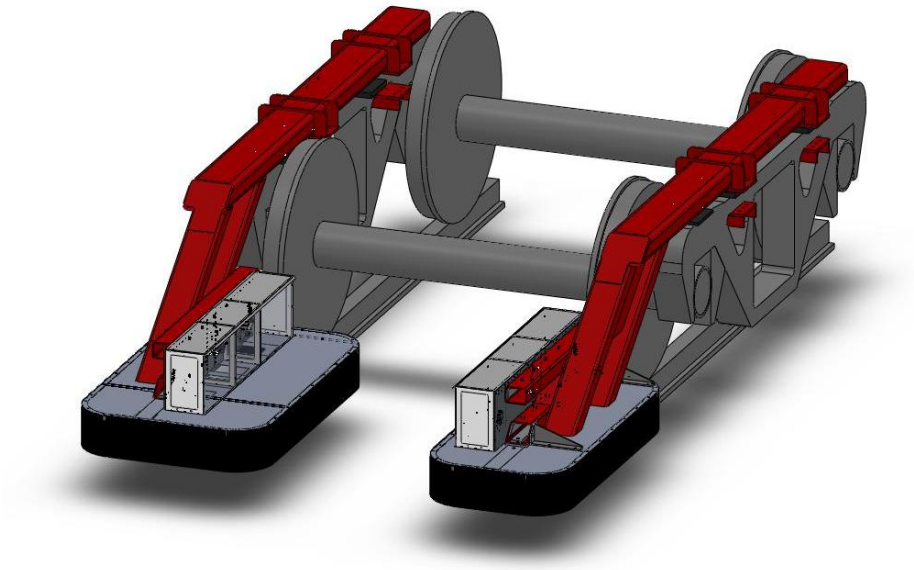

Figure 3-15. Modifications to shrouds.

The last modification to mention is the addition of another set of high-durometer rubber padding near the angled portion of the red beam on the top of the side frames. The other two sets of rubber padding positioned at the mounting plate locations were already in place. However, without the third set of rubber pads, the red beam was

actually cantilevered over a much greater distance than necessary. The additional padding provides more support to the red beams. This modification was seen as a simple way to enhance the mounting arrangement of the red beams to the side frames. Previous studies of the beams' rigidity have shown that they provide a stable reference frame for the measurement equipment (Norman, 2004).

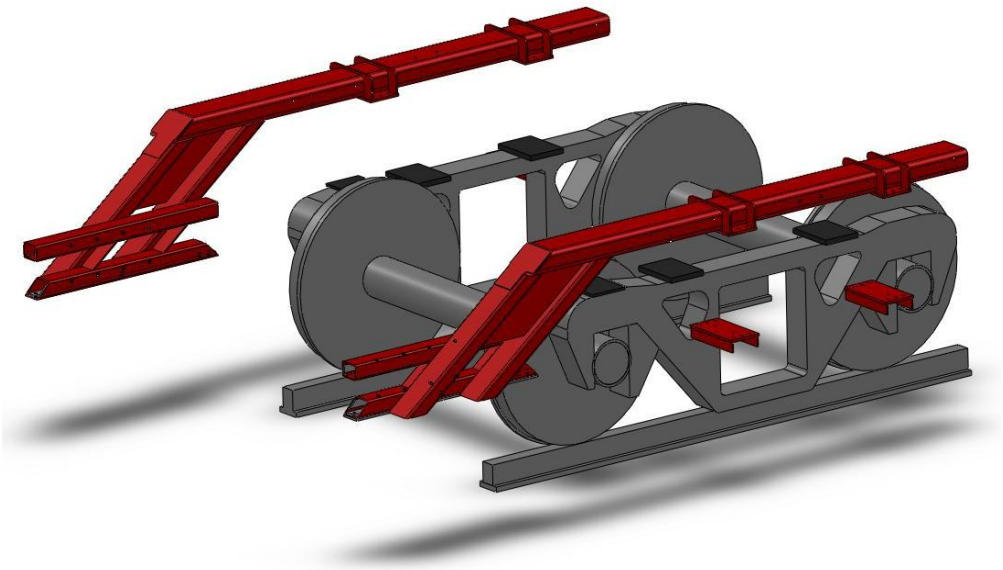

Figure 3-16. Method of mounting red beams to side frames.

3.4 Outline of Field Data

The UNL vertical track deflection measurement system has been tested over thousands of miles of track over the past several years. The results have yielded a wealth of data and have provided a basis to begin classifying defects and setting exception thresholds. Current exception criteria include computing a deviation ratio, σ_{ratio}, computing the difference between an individual data point and the mean, Δ, and analyzing the difference between *Yrel* and *ECO* (Lu, 2008). The deviation ratio is

calculated by forming a ratio of the difference criterion, Δ, with the standard deviation in the data over 0.1 miles of track.

The current exception criteria have proven successful in identifying defective areas in track. For example, one test conducted in 2007 on the South Morrill subdivision of the UPRR independently identified three derailment locations (Lu, 2008). Although the UNL system is building a solid reputation for identifying problem areas in track, further understanding of the data is required to make the system a more robust tool for maintenance activities.

The following sections briefly summarize three different exception sites identified by the UNL system. These sites encompass some of the variety of magnitudes and shapes found in the UNL data as well as the range of defects discovered. The locations of these sites are not discussed. Instead, emphasis is placed on the relative shape of the data and how this might be used to identify the level and type of defects.

3.4.1 Site A: Failing Insulated Joint

The first exception location discussed is referred to as site "A" at the position of a failing insulated joint. The data for this site are displayed in Figure 3-17 and a photo of the actual site is shown in Figure 3-18. The data reveals a large peak of 1.2" in *Yrel* with only a 0.3" measurement in *ECO* on the south rail. The data for the north rail do not reveal any significant exceptions at this location.

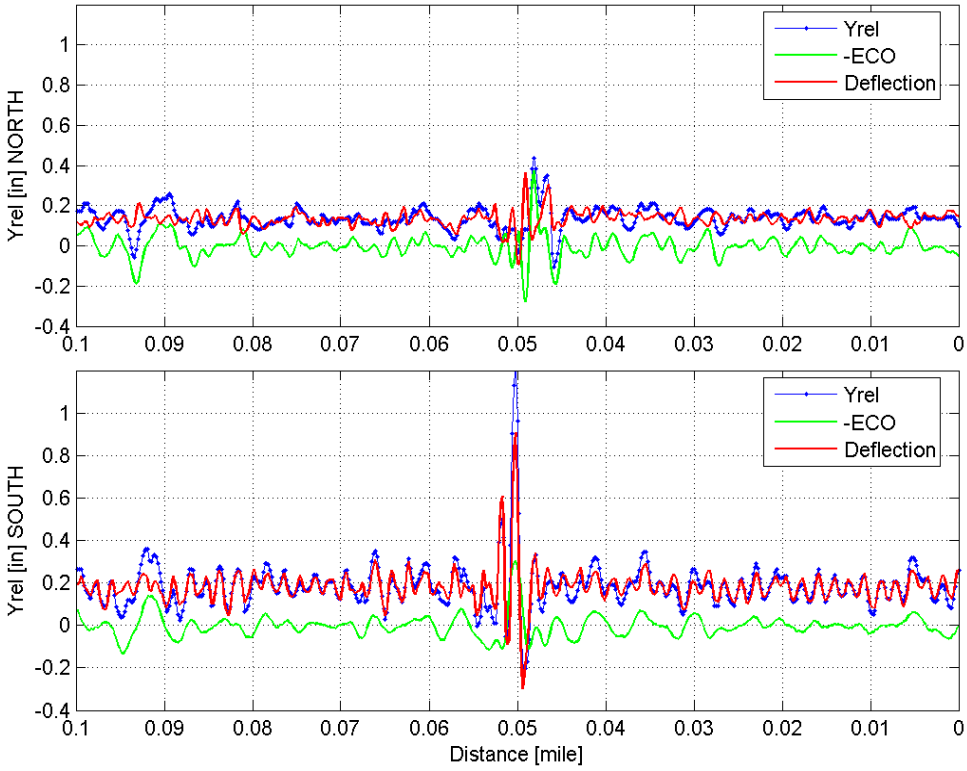

Figure 3-17. Data at site A (Lu, 2008).

The large difference between *Yrel* and *ECO* indicates that although there are not any significant geometry variations at this location, the deflection of the rail must be quite significant. Such differences have proven to be a common trait for data exceptions located at poor joints such as those shown in Figure 3-18. In fact, large differences between *Yrel* and *ECO* have proven to be one of the most important exception criteria (Lu, 2008). However, this type of magnitude and shape in the data is not necessarily exclusive to poor joints, as revealed by the next site.

Figure 3-18. Failing insulated joint at site A (Lu, 2008).

3.4.2 Site B: Broken Concrete Ties

Several broken concrete ties are present at the location of site "B." The data and photo of this site are shown in Figure 3-19 and Figure 3-20 respectively. Both rails have peaks in *Yrel* exceeding 0.8". While the *ECO* peak matches *Yrel* on the south rail, an *ECO* peak of only 0.37" is present on the north rail.

These data shapes highlight some of the complexity involved in setting thresholds based on one criterion alone. This site was flagged based mainly on the north rail data because of the large difference between *Yrel* and *ECO*. Yet the peaks in the data measured on the south rail are also a result of the broken ties. Such results emphasize the correlation between geometry and poor support conditions on railroad track. The reasons why some exception sites exhibit large differences between *Yrel* and *ECO* while at other sites they are the same is not completely understood. Mathematical simulations may provide some clues as discussed in a later chapter.

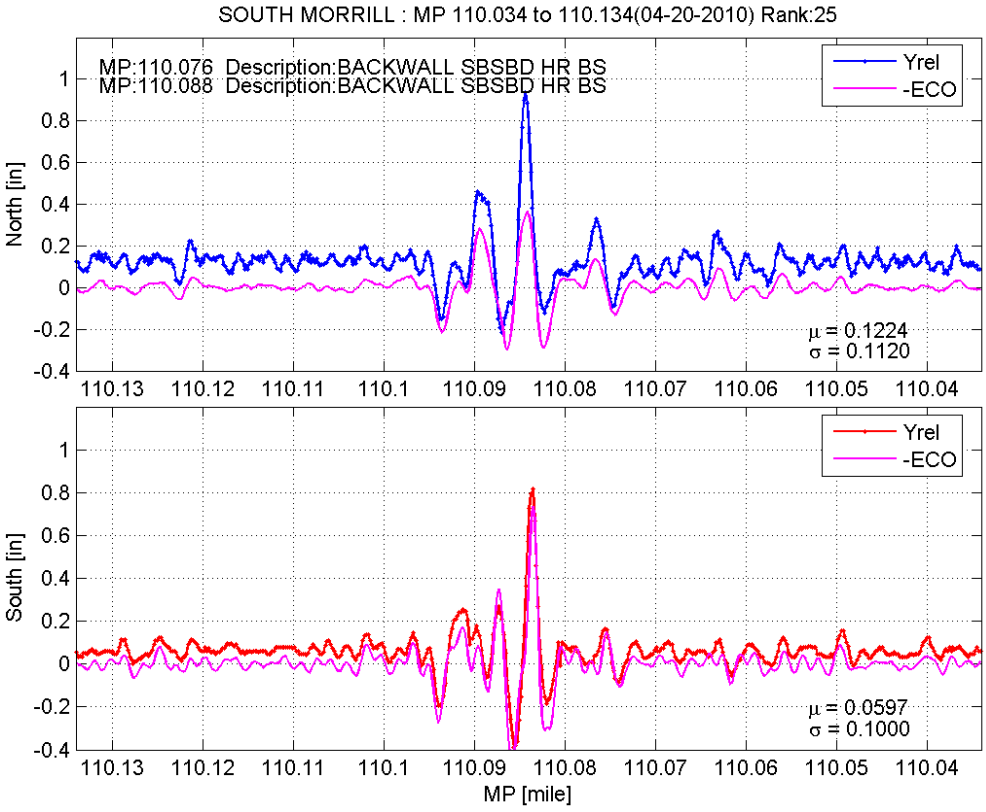

Figure 3-19. Data at site B.

Figure 3-20. Broken ties at site B.

3.4.3 Site C: Mud Hole at Crossing

The *Yrel* and *ECO* data match very well at site "C" as displayed in Figure 3-21. The *Yrel* and *ECO* data both peak at about 0.92" on the south rail with a *Yrel* peak of 0.68" and *ECO* peak of 0.38" in the data for the north rail. The matching data indicates that a dip in the vertical track geometry might exist at a location of poor support.

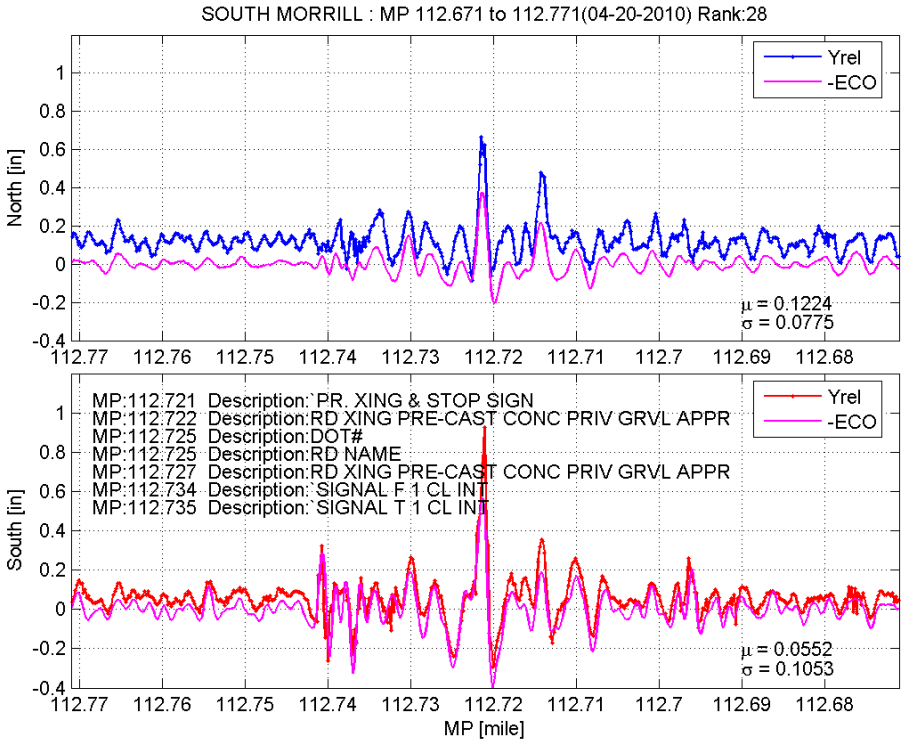

Figure 3-21. Data at site C.

During a site visit, a 31 ft mid-chord offset (MCO) of 0.875" was recorded. The MCO is measured by placing a 31 ft string on top of the rail and measuring the difference in height between the top of the rail and the string at its midpoint. The site visit revealed a mud hole with severe pumping across several concrete ties as displayed in Figure 3-22.

Figure 3-22. Mud hole at site C.

3.4.4 Classifying Exceptions Based on Data

The connection between poor track support and track geometry is complex. Sites with poor support such as site "C" often exhibit both large *Yrel* and *ECO* peaks. However, sites "A" and "B" reveal that defective geometry is not always present at locations of poor track support. Previous research has shown that large differences in *Yrel* and *ECO* provide good exception estimates. However, this same research theorizes that both poor support and poor geometry are usually needed to generate large peaks in *Yrel* data (Lu, 2008).

Classifying exceptions based on the data shapes has proven difficult. Although current criteria have proven useful in identifying exceptions, several separate indicators may be needed for categorization. Mathematical techniques, such as the finite element method described later, may provide assistance in understanding this complex issue. For example, the interaction between poor support, geometry, and joints may lead to a specific shape in the data indicative of a certain level of maintenance need.

Chapter 4, RAIL BENDING STRESS

Flexural bending stress in the vertical plane has historically been recognized as one of the significant contributions to fatigue failure of rail (Greisen et al., 2009). Despite this recognition, current measurement practices do not include any methods to measure the bending stress in rail over significant distances of actual track. Such a method would provide key insights that would be useful for track maintenance as well as input into the various software programs developed by the Association of American Railroads (AAR).

The UNL vertical track deflection measurement system has demonstrated a robust method to determine track deflection over significant distances. As already shown, this measurement can be directly related to the track support modulus using the Winkler or cubic track models. Recent studies suggest that this system has the additional capability to determine the actual bending stress in the rail. The following chapter outlines the relationship between the UNL measurement and rail bending stress. Field tests verify this relationship, which expands the versatility of the UNL system.

4.1 Relationship to UNL Measurement

The UNL system establishes three points of the rail shape beneath the loaded wheels and over a distance of 10 ft. Applying any of the track models described in Chapter 2, this partial rail shape can be mapped into the bending stress in the rail. For this investigation, the method chosen is the classic Winkler model. The rail shape estimated by the Winkler model for two axles beneath the UNL test car (and other axles of a trailing car) is shown in Figure 4-1.

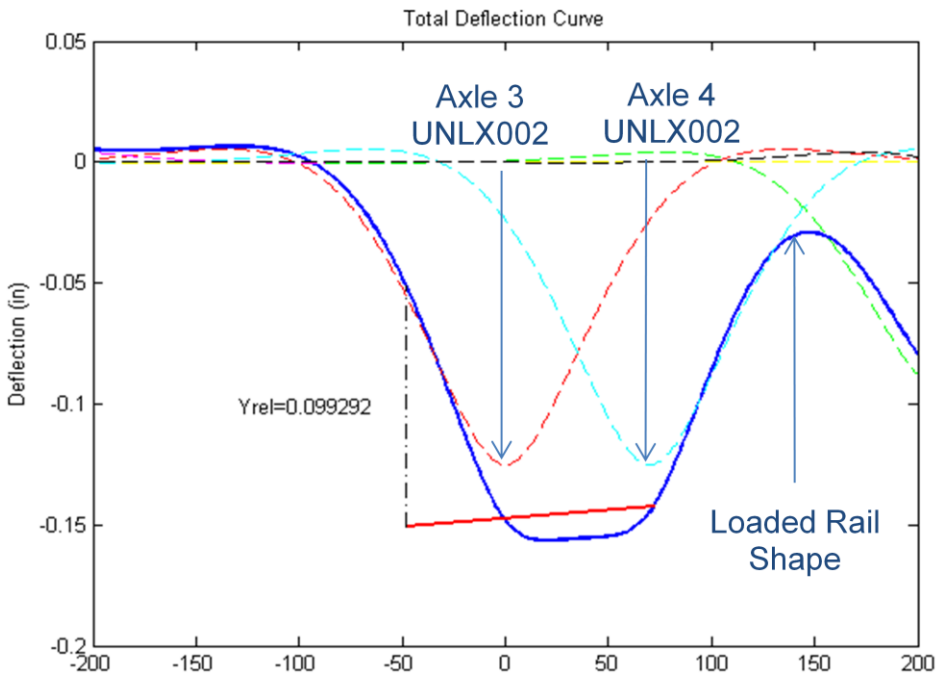

Figure 4-1. Winkler shape of rail beneath UNL car showing *Yrel* measurement.

The Winkler shape of the rail in Figure 4-1 is found by superposition of the axle loads and application of Equation 2-6. Previous research has shown that the Winkler model provides acceptable agreement with field measurements (Zarembski & Choros, 1980; Kerr, 2003). The bending moment, *M(x)* that results from the deflection estimated by the Winkler model is given by:

$$M(x) = EIw''(x) = \frac{P}{4\beta} e^{-\beta|x|}\left[\cos(\beta|x|) - \sin(\beta|x|)\right] \qquad \text{Equation 4-1}$$

where: $\beta = \sqrt[4]{\frac{u}{4EI}}$ Equation 4-2

P is the load on the track

u is the track modulus

E is the modulus of elasticity of the rail

I is the second moment of area of the rail section

x is the longitudinal distance along the track

The bending strain is then calculated at $x = 0$, matching the location of axle three in Equation 4-1. This location matches the position where *Yrel* is measured from the UNL test car. Knowledge of the bending moment is combined with classical beam theory to calculate the bending strain in the rail. The bending strain, ε_B, that results is defined as:

$$\varepsilon_B = \frac{Mz}{EI} \qquad \text{Equation 4-3}$$

where: *z* is the distance from the neutral axis

The preceding derivation allows the Winkler model to be used to calculate theoretical *Yrel* and bending strain values for a known set of loading conditions. For a particular rail profile and set of axle loads the only variation in the calculations is the track modulus. Varying the track modulus and calculating the corresponding *Yrel* and bending strain values allows for the creation of a look-up table, which is displayed graphically in Figure 4-2. The bending stress is directly related to the bending strain through Hooke's law.

$$\sigma_B = E\varepsilon_B \qquad \text{Equation 4-4}$$

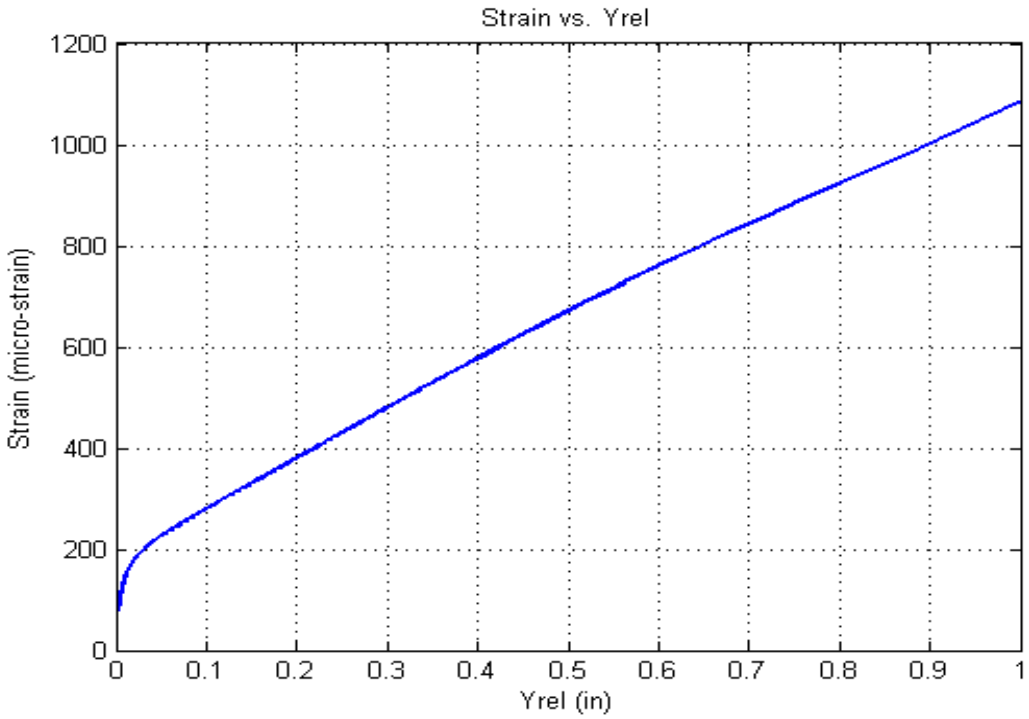

Figure 4-2. Relationship between *Yrel* and bending strain.

4.2 Field Testing

4.2.1 Method of Measurement

Field tests were conducted on the UPRR's Yoder subdivision to verify the theoretical mapping of *Yrel* measurements into bending strain values. The tests consisted of mounting strain gages on top of the rail's bottom flange and measuring a value of *Yrel* with the UNL measurement system. The strain gages were placed symmetrically on each side of the rail in a Wheatstone bridge configuration as shown in Figure 4-3. This strain gage bridge configuration eliminated any transverse loading effects.

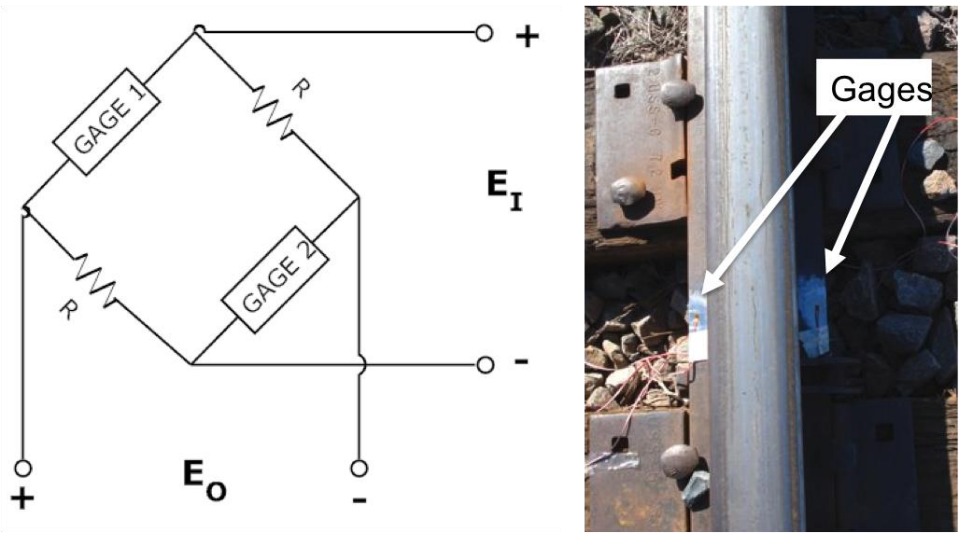

Figure 4-3. Wheatstone bridge configuration and strain gage placement.

The output from the bridge was input into a Vishay Model 2150 strain indicator and signal conditioner shown in Figure 4-4. The data were recorded with a standard analog-to-digital USB input card in conjunction with a laptop computer.

Figure 4-4. Vishay model 2150 strain gage signal indicator (Vishay).

The strain output from the strain indicator, ε_B, is expressed as:

$$\varepsilon_B = \frac{\varepsilon_q}{k} = \frac{\varepsilon_q}{2} = \frac{2\Delta E_o}{F(E_i - 2\Delta E_o)} \qquad \text{Equation 4-5}$$

where:

ε_q is the strain output for a quarter-bridge Wheatstone bridge

ΔE_o is the change in output voltage recorded from the indicator

E_i is the excitation input into the bridge (10 volts)

F is the gage factor (~2.1 for all gages used in the tests)

K is the bridge factor (2 for the bridge configuration used)

The test-car consist (configuration of rail vehicles) used in the Yoder subdivision test passed over the strain gages at constant velocity, yielding the results displayed in Figure 4-5. The locomotive and test car axles are clearly visible in the data. Larger bending strains are present beneath the locomotive axles due to its larger weight. The effect of adjacent axles is apparent in the strain with the overall curve analogous to the deflections found when superimposing adjacent axles in the Winkler model as shown in Figure 2-4.

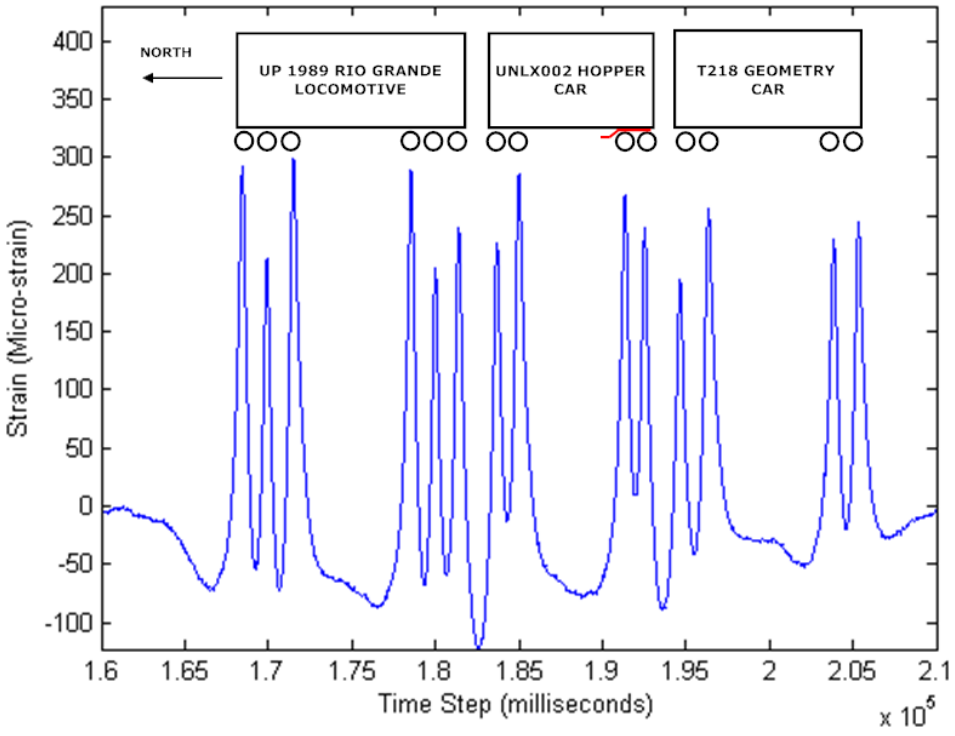

Figure 4-5. Strain gage measurements of testing consist.

In order to make an accurate comparison with the *Yrel* strain calculation, the measurement car was spotted with axle three (shown in Figure 4-1) directly above the strain gage location. The resulting strain measurement is displayed in Figure 4-6. Increases in strain are observed as the locomotive axles pass over the strain gages followed by axles one and two of the test car. The data spreads out as the car comes to rest since the abscissa represents a time axis. As axle three is placed directly over the strain gages, the strain increases from 0 με to 290 με.

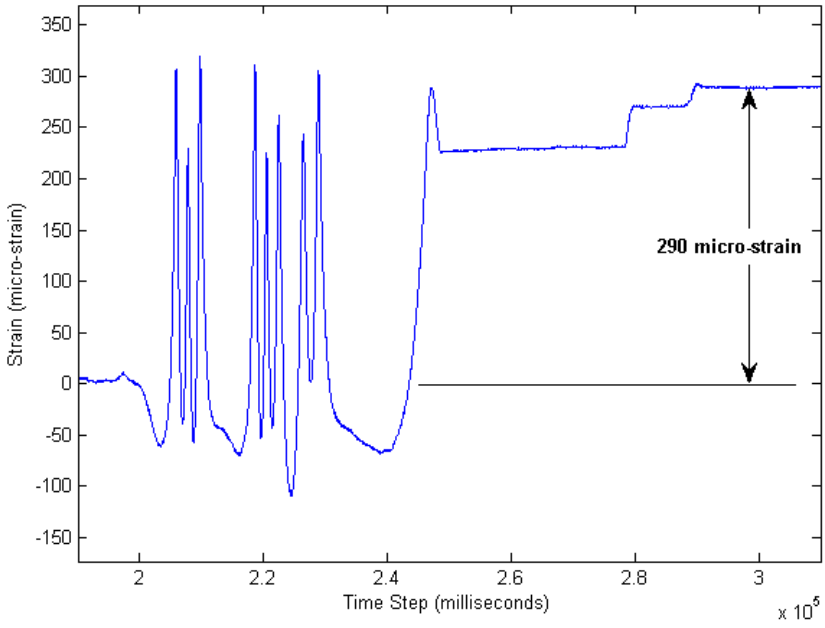

Figure 4-6. Spotting of UNL car and measurement of strain beneath inboard axle.

The strain measurement starts at zero in Figure 4-6 since the strain gages were mounted to the unloaded rail. Temperature-based axial strain did not affect the data since the ambient temperature did not vary between gage placement and spotting of the car. Furthermore, any residual stresses are not measured since they would have been present prior to attaching the gages.

The strain gage measurement represents the change in bending strain relative to the unloaded rail profile. This fact is important to note because some initial bending strain is present in the rail since the unloaded rail profile is not perfectly straight. In order to account for this initial strain, a measurement of the unloaded rail profile was completed with an independent instrument. A surveyor's transit was used to independently measure the unloaded and loaded profiles of the rail before and after spotting the car as shown in Figure 4-7.

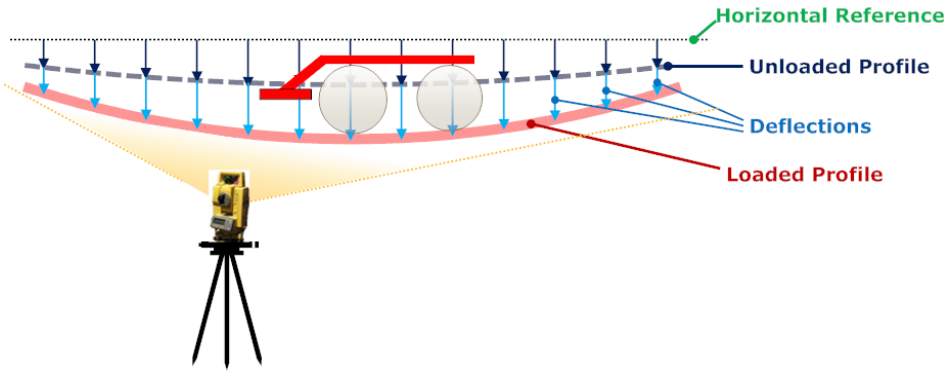

Figure 4-7. Absolute measurement of loaded and unloaded rail profile (Lu, 2008).

In order to measure the rail profile while the train car wheels were in place, magnetic steel rulers, rather than a prism, were used as the references. This new method is shown in Figure 4-8. Before the rail was loaded, the surveyor's transit was used to record a reference value on the steel rulers. After the spotting train loaded the rail, the transit was again used to record the deflection of the steel rulers. Therefore, the deflection of the ruler indicates the change in rail profile between the unloaded and loaded states. The change in profile is added to the unloaded profile to produce a measurement of the loaded profile relative to an absolute horizontal reference.

Figure 4-8. Magnetic rulers used to measure rail profile with surveyor's transit.

As mentioned earlier, the field tests were conducted on UPRR's Yoder subdivision in southeast Wyoming. This subdivision handles approximately 2 MGT per year in rail traffic. The measurements were made on October 15, 2008. Two specific sites were instrumented with strain gages for comparison with the strain estimated by the UNL system. The first site at MP 231.6 was comprised of stiff tangent track. The second site at MP 228.6 consisted of a soft mud hole. Both locations were constructed of 131 lb rail with wood crossties.

4.2.2 Strain Results at Stiff Tangent Track Site

The measurement results from the section of stiff tangent track at MP 231.6 are shown in Figure 4-9. The UNL *Yrel* measurement of 0.15" indicates that this track was well supported. Based on the chart in Figure 4-2, the absolute bending strain is estimated to be 332 με. The strain gage reading relative to the unloaded profile was 290 με. However, some existing bending strain must be present based on the unloaded profile of the rail. In order to directly compare the *Yrel* estimated strain with the strain gage reading, the unloaded bending strain must be removed from the *Yrel* measurement.

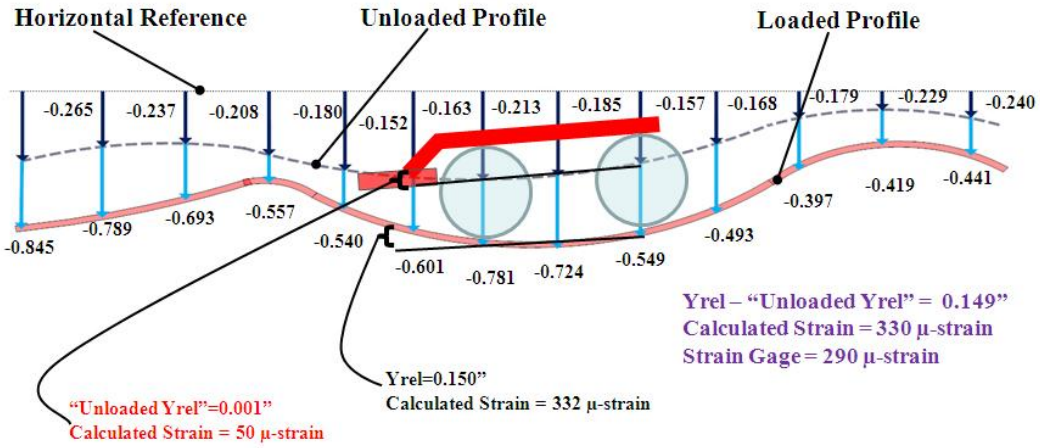

Figure 4-9. Strain comparison at the location of a stiff section of tangent track.

As displayed in Figure 4-9, both the unloaded and loaded profiles were measured with the values of each displacement shown next to the arrows in inches. These profile measurements are used to calculate a change in *Yrel*, referred to as *ΔYrel*. This *ΔYrel* is determined by subtracting a *Yrel* value calculated with the unloaded profile from the *Yrel* value measured with the UNL car. Then, using the data in Figure 4-2, the strain estimated with the *ΔYrel* value can be compared directly with the strain gage data.

Since the track is well supported at this location, the unloaded *Yrel* value is only 0.001", resulting in a *ΔYrel* of 0.149". Therefore, the change in bending strain from loaded to unloaded is 330 με. This measurement differs from the strain gage recording of 290 με by only 13.7%.

Based on the preceding results and discussion, it is theorized that the original value of *Yrel* from the UNL measurement car provides a true estimation of the bending strain present in the rail. However, the *ΔYrel* value is needed to compare the strain gage readings since they are not mounted to the rail while it is in a strain-free state. This premise becomes more apparent at the following site.

4.2.3 Strain Results at Soft Mud Hole Site

The measurement results from a poorly supported section of track with muddy ballast and pumping crossties are shown in Figure 4-10. The UNL system recorded a *Yrel* value of 0.73" indicating softer track. This results in an estimated bending strain of 868 με. The strain gages at this location measured a change of 580 με from the unloaded to the loaded state.

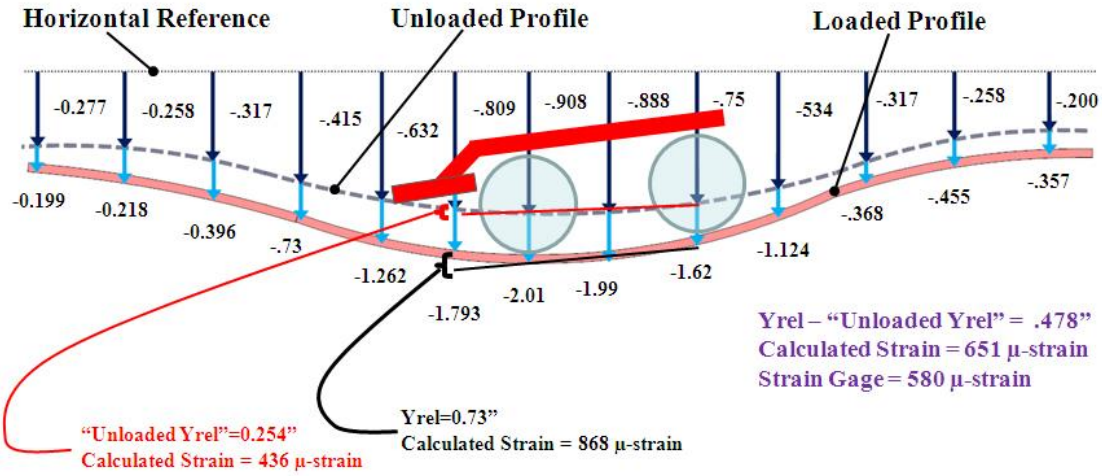

Figure 4-10. Strain comparison at the location of a soft mud hole.

As shown in Figure 4-10, a significant dip in the rail profile was present at this site. Using the unloaded profile, a *Yrel* value of 0.254" is calculated. Repeating the method described for the previous site, a *ΔYrel* of 0.478" is then determined by subtracting the unloaded *Yrel* from the *Yrel* value measured by the UNL car. The bending strain estimated from the *ΔYrel* value is 651 με. This differs by only 12.2% from the measured strain of 580 με.

Again, the absolute bending strain is considered to be estimated most accurately by the *Yrel* value measured with the UNL system. The *ΔYrel* value is only needed to compare the measurement with the strain gage readings for validation purposes. Had the

strain gages been mounted to the rails while they were in a strain-free state, this step would be unnecessary.

The results from both sites are displayed in Table 4-1.

Table 4-1. Strain measurement validation.

	MP231.6	*MP228.6*
Strain from ΔYrel	330	651
Strain from gage	290	580
% Error	**13.7%**	**12.2%**

The field validation results display a strong correlation between the strain gage measurements and the strains estimated with the *Yrel* measurement. The differences of 13.7% and 12.2% are well within the errors present in both the model and field measurements. At both locations, the calculated strain was slightly above that of the measured strain. The lower measured value may have resulted from slight misalignment of the strain gages with the axis of the rail. Furthermore, the axle may not have been parked exactly above the strain gages such that the gages did not record the maximum strain present directly beneath the axle.

These early results expand upon the capability and versatility of the UNL vertical track deflection measurement system. Increased understanding of how the UNL system relates to the track response will further its ability as a maintenance tool. The next chapter reveals how finite element methods may clarify the relationship between measured *Yrel* data and the mechanical response of the track.

Chapter 5, FINITE ELEMENT ANALYSIS

As described in Chapter 2, several analytical models have been developed for use in railroad track design and to characterize the track response under load. Despite the usefulness of some of these models, they lack the complexity needed to fully characterize real track. Advancements in finite element analyses (FEA) have provided more realistic representations of the track response. These FEA programs often need to be formulated with a specific objective in order to minimize computational costs. Therefore, a FEA program suitable for solving one problem may not adapt well to another goal.

Custom FEA programs offer realistic solutions to well-defined problems. One particular FEA program titled GBEAM was developed to better understand track dynamics (Carr, 1999). This program analyzed the motion of a single mass rolling along the track. The track was modeled as an Euler beam resting on a damped, elastic foundation. The results highlighted the importance of measuring track deflection and concluded that track dynamics become important in high-speed simulations (Carr, 1999).

The following sections describe the development and results of a new custom FEA program created to characterize track response from the perspective of the UNL system. Nonlinear foundation characteristics are examined with the commercial FEA software, ALGOR®. The purpose of this analysis is to provide better understanding of the data collected by the UNL system. Improved evaluation of this data would enhance its potential as a resource for maintenance planning.

5.1 FEA Model Development

5.1.1 FEA Objectives & Specifications

The main objective of the FEA analysis developed in this thesis investigation is to characterize track response based on the UNL measurement system's point of view. This system measures the vertical deflection of the track from a moving reference frame attached to a three-piece truck on a modified hopper car. Variations in the track support and in short-wavelength track geometry affect the UNL measurement. The exact nature of how these track characteristics relate to the UNL data is important for maintenance planning.

The UNL system, described in detail in Chapter 3, yields relative track deflection data defined as *Yrel*. This measured deflection is used in conjunction with a 10 ft end-chord-offset (*ECO*) calculated from the vertical rail profile to identify areas of poor track support. The difference between *Yrel* and *ECO* is used as one exception criterion for identifying locations needing further inspection (Lu, 2008). This criterion is used along with relative thresholds for the magnitudes of the *Yrel* and *ECO* measurements.

Certain track locations yield identical shapes and magnitudes for both *Yrel* and *ECO* as shown in the top of Figure 5-1. Other locations result in large peaks in *Yrel* data with relatively minor *ECO* peaks as illustrated in the bottom of Figure 5-1. Corresponding site visits have shown that each case can result in the identification of track defects. However, some visits have revealed track that is not in need of maintenance despite large magnitudes in the peaks of *Yrel* data.

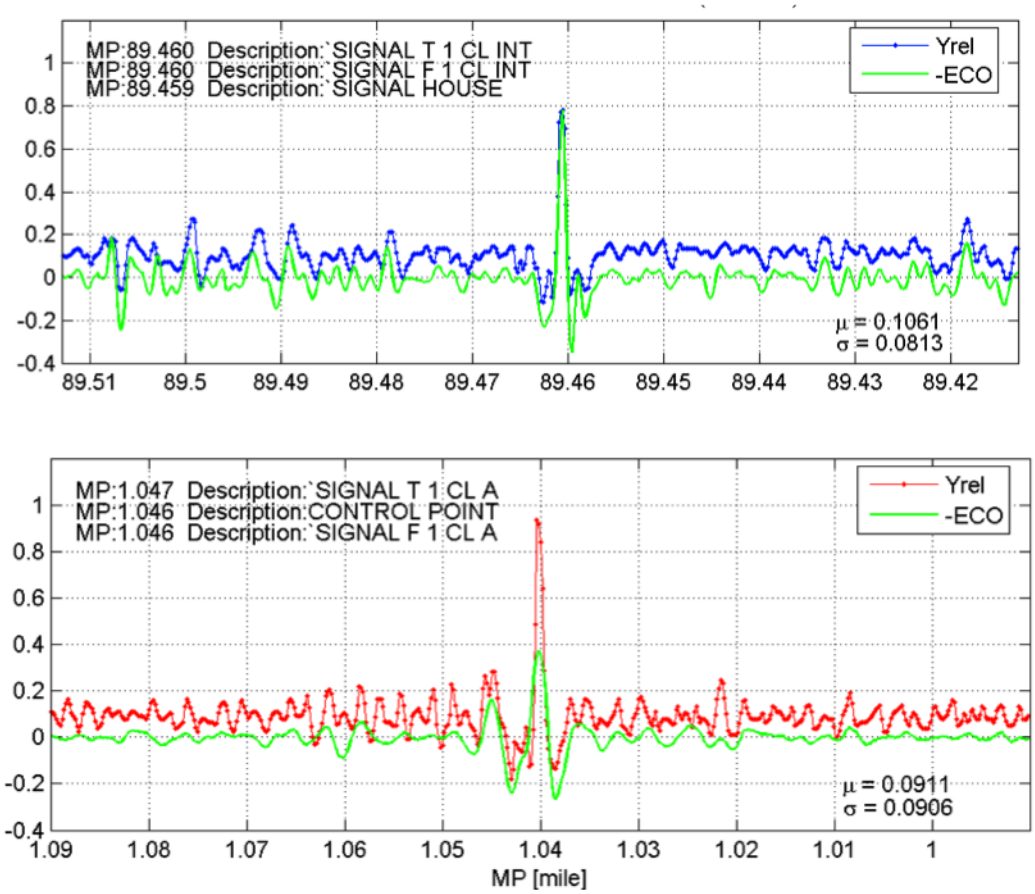

Figure 5-1. Different shapes in *Yrel* and *ECO* data.

Using the FEA program to characterize the track response based on the *Yrel* and *ECO* measurements may provide insights into which track features lead to certain measurement results. For example, different combinations of poor track support, poor track geometry, and failing joints may lead to either case shown in Figure 5-1 as well as intermediate situations. Therefore, the particular program developed should have the ability to vary each of these items individually and analyze the corresponding effects on the UNL measurement results.

Several specifications simplify the structure and focus of the FEA program. The FEA program assumes a Winkler foundation. However, the program allows for variation in support modulus along the track. More complicated, nonlinear foundations are

examined with ALGOR®. The model is constructed in two dimensions and considers only one rail. Fixed boundary conditions are used, and the length of the model ensures that the boundaries do not affect the deflection results. The dimensions correspond to a standard coal train traveling over 132 lb rail. The elements are only one inch in length so that enough nodal deflections are calculated to reproduce the *Yrel* measurement. Dynamic effects are ignored and the deflections needed to reproduce the *Yrel* data are obtained using a quasi-static approach.

5.1.2 Governing Equation & Program Development

The assumption of a Winkler foundation leads to the governing differential equation defined previously in Equation 2-2. This equation is rewritten in a form more suitable for the derivation of the necessary finite element equations as displayed in Equation 5-1. The equation represents a beam supported by a series of continuous, independent springs. Equilibrium of a differential length of the beam yields:

$$\frac{d^2}{dx^2}\left(EI\frac{d^2w}{dx^2}\right)+uw-q=0 \qquad \text{Equation 5-1}$$

The derivation of the finite element equations follows a variational formulation based on the principle of minimum potential energy and the calculus of variations. The following simplifying techniques based on the method in (Thompson, 2005) are used in the derivation:

1. The governing equation is placed in its "weak" form (from the calculus of variations) rather than directly into the potential energy functional.
2. The general element approximating functions are defined by a local coordinate system with the origin at the element's left end.

3. Equations and calculations are completed in matrix notation more suitable for programming.
4. Known boundary values are included in the calculations as if they were unknowns and only accounted for after the final matrix equation is created.

The governing equation defined in Equation 5-1 requires that the fourth derivative of *w* exists. In order to reduce these requirements, the equation is placed in its weak form giving:

$$\int_0^L \delta w \left[\frac{d^2}{dx^2}\left(EI \frac{d^2 w}{dx^2} \right) + uw - q \right] dx = 0 \qquad \text{Equation 5-2}$$

where δw represents a small variation in w

L is the length of a general element

Placing the governing equation in its weak form reduces the requirements for higher order derivatives in the solution. Integrating by parts twice and substituting the expressions for shear and moments found in elementary beam theory yields Equation 5-3 (Thompson, 2005).

$$\delta w_L V_L - \delta w_O V_O - \left(\frac{d\delta w}{dx} \right)_L M_L + \left(\frac{d\delta w}{dx} \right)_O M_O + \int_0^L \left\{ \left[\frac{d^2 \delta w}{dx^2} EI \frac{d^2 w}{dx^2} \right] + \delta w k w - \delta w q \right\} dx = 0 \qquad \text{Equation 5-3}$$

where

$$M = EI \frac{d^2 w}{dx^2} \qquad \text{Equation 5-4}$$

$$V = \frac{d}{dx}\left(EI \frac{d^2 w}{dx^2} \right) \qquad \text{Equation 5-5}$$

Based on the weak formulation of the governing differential equation, only the second derivative of *w* is required to exist, as illustrated by Equation 5-3. The condition

for existing second derivatives requires that the approximating shape functions be continuous and have continuous first derivatives. Hermite cubics are used as the approximating functions to accomplish these objectives. Each function is defined in terms of the nodal values for *w* and *dw/du* at the ends of each element. These functions are expressed in terms of their Gaussian coordinates as displayed in the following equations.

$$N_1 = \left(\frac{1}{4}\right)(u+2)(u-1)^2 \qquad \text{Equation 5-6}$$

$$N_2 = \left(\frac{1}{4}\right)(u+1)(u-1)^2 \qquad \text{Equation 5-7}$$

$$N_3 = -\left(\frac{1}{4}\right)(u-2)(u+1)^2 \qquad \text{Equation 5-8}$$

$$N_4 = \left(\frac{1}{4}\right)(u-1)(u+1)^2 \qquad \text{Equation 5-9}$$

where *u* defines the Gaussian coordinates

With respect to the nodal values and matrix notation the approximation becomes:

$$w(u) = \lfloor N_1(u) \;\; N_2(u) \;\; N_3(u) \;\; N_4(u) \rfloor \begin{Bmatrix} W_a \\ dW_a/du \\ W_b \\ dW_b/du \end{Bmatrix} \qquad \text{Equation 5-10}$$

where *a* and *b* represent the left and right nodes respectively

u defines the Gaussian coordinates

Gaussian coordinates are used since Gaussian quadrature is the numerical integration method used to solve the finite element equations. Gaussian quadrature is a method of determining an integral by using a weighted average of the integrand evaluated at specific sampling points (Thompson, 2005). In this case, four-point Gaussian

quadrature is used since four points are needed to exactly integrate a cubic polynomial. The execution of this integration scheme is revealed in the FEA program code written in MATLAB® and included in the appendix.

The approximating shape functions are depicted graphically with respect to the Gaussian coordinates as shown in Figure 5-2.

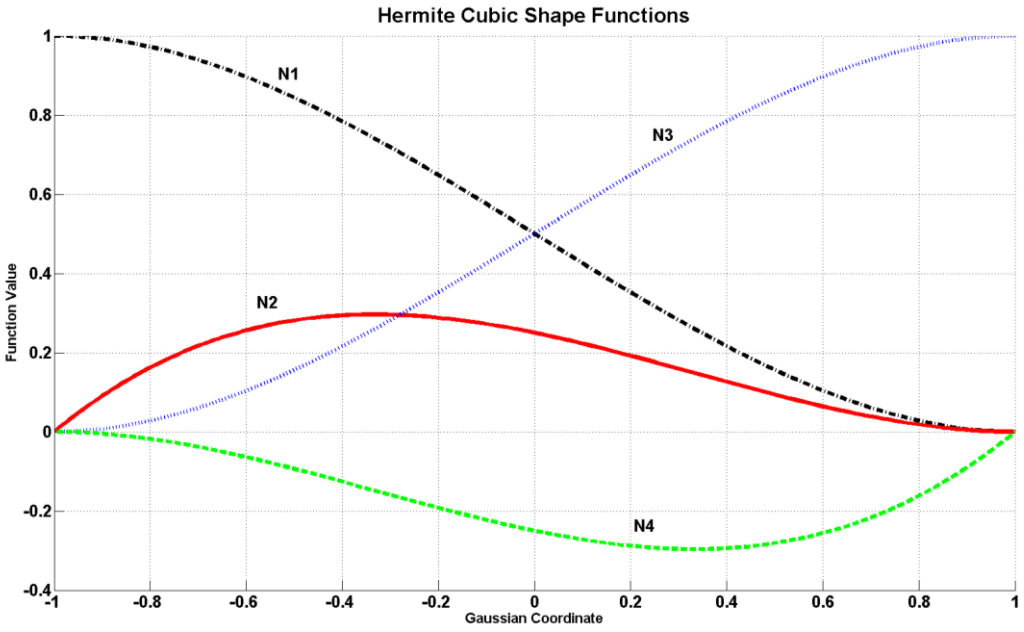

Figure 5-2. Hermite cubic shape functions.

Since the shape functions are expressed in Gaussian coordinates, the integration limits of ±1 do not correspond with the *x*-axis of the elements. A change of variables is needed to map the functions and their derivatives into the *x*-axis of the element coordinate system. This mapping is completed with the following linear transformation:

$$x = \left(\frac{a+b}{2}\right) + \left(\frac{b-a}{2}\right)u \qquad \text{Equation 5-11}$$

$$dx = \left(\frac{b-a}{2}\right)du \qquad \text{Equation 5-12}$$

$$du = \left(\frac{2}{b-a}\right)dx \qquad \text{Equation 5-13}$$

where *a* and *b* represent the left and right nodes respectively

u represents the Gaussian coordinates

The actual transformation for each shape function and its derivatives is formulated in (Thompson, 2005) and used in the FEA program code shown in the appendix. The solution and its variation can then be expressed in terms of the shape functions as follows:

$$\begin{aligned} w &= \lfloor N \rfloor \{W\} & \delta w &= \lfloor N \rfloor \{\delta W\} \\ w' &= \lfloor N' \rfloor \{W\} & \delta w' &= \lfloor N' \rfloor \{\delta W\} \\ w'' &= \lfloor N'' \rfloor \{W\} & \delta w'' &= \lfloor N'' \rfloor \{\delta W\} \end{aligned} \qquad \text{Equation 5-14}$$

where W and δW represent the arrays of nodal values

Substituting the expressions in Equation 5-14 into the integral term of Equation 5-3 yields the following integral expressions for each element:

$$\begin{aligned} [S_1]_e &= \int_0^L \{N''\}^T EI \lfloor N'' \rfloor dx \\ [S_2]_e &= \int_0^L \{N\}^T k \lfloor N \rfloor dx \\ \{f\}_e &= \int_0^L \{N\} q dx \end{aligned} \qquad \text{Equation 5-15}$$

where $[S_1]_e$, $[S_2]_e$, and $\{f\}_e$ correspond to the first, second, and third terms of the integral in Equation 5-3

These expressions are evaluated and assembled for each element. The shear and moment terms appearing in Equation 5-3 are used to define the boundary conditions. The $[S_1]_e$ and $[S_2]_e$ terms define the stiffness matrices and the $\{f\}_e$ term represents the loading. After collecting the element matrices into a global matrix, the resulting expression shown

in Equation 5-16 can be solved for the nodal deflections. The matrices that result from this model are banded and symmetric allowing for a compact storage arrangement. The FEA program written in MATLAB® and shown in the appendix uses Gaussian elimination to solve the overall matrix equation.

$$[SK]\{W\} = \{Q\} \qquad \text{Equation 5-16}$$

where [SK] is the global stiffness matrix

{W} is the array of nodal deflections

{Q} is the forcing vector

The FEA program constructed in MATLAB® completes the integrations specified in Equation 5-15 over the array of elements, assembles the global matrices and solves for the nodal deflections in Equation 5-16. A flowchart illustrating the execution of this program is displayed in Figure 5-3.

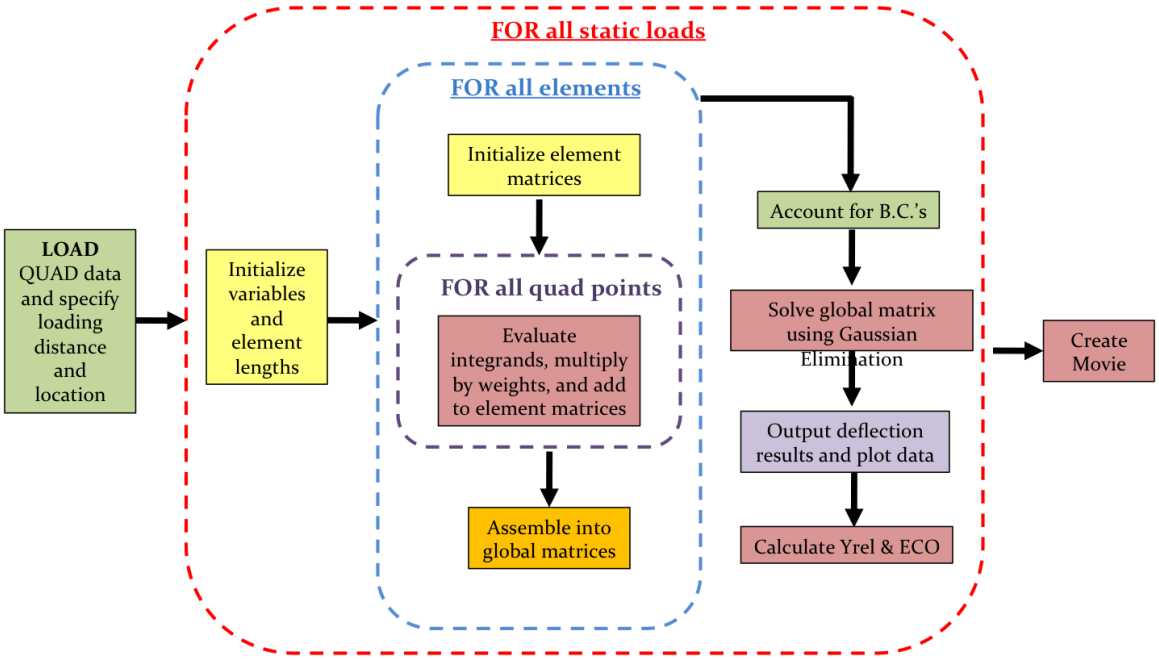

Figure 5-3. Flowchart of custom FEA computer program.

The FEA program is an extension and adaptation from similar programs developed in (Thompson, 2005). The actual code, shown in the appendix, is divided into four separate MATLAB® files designated as `FEM.m`, `INITIAL.m`, `SF.m`, and `sGAUSS.m`. The main file, `FEM.m`, controls the program flow, integrates the element matrices, and plots the results. The execution of the program begins by loading the quadrature weights and points from a separate text file, `QUAD`, stored in the program directory. The loading is defined in the file `INITIAL.m`, which also specifies the model dimensions and initializes all variables. A program loop is used to traverse through a series of static loads as specified by the diagram in Figure 5-3. This method of quasi-static loading is described in the next section and allows for a simple calculation of the *Yrel* measurement found with the UNL system.

Within each loading cycle, the element matrices are constructed and then integrated within the main program using the `SF.m` file. This file defines the approximating shape functions and their derivatives. The element matrices are successively assembled into the global matrix. Once the global matrix is constructed, the boundary conditions are taken into account and the nodal deflections determined using the `sGAUSS.m` file. The main program displays deflection plots of the track for each loading cycle. These plots include graphics of the *Yrel* and *ECO* measurements and the data that would be found by the UNL system. After the specified section of track has been traversed, a movie is created by merging together the individual plot frames.

5.1.3 Quasi-Static Loading & *Yrel* Computation

The main goal of the FEA program is to analyze the track response from the perspective of the UNL measurement system. The data is collected from a moving

railcar and expressed by the *Yrel* measurement defined previously. In order to simulate the movement of the railcar along the track, a quasi-static, rather than a dynamic, approach is utilized. Placing static loads at specific locations along the track and computing the corresponding nodal deflections completes this method. The static loads are then translated a specified amount (12”) and the deflections recomputed. This process is repeated until the static loads have traversed far enough to cover a particular track feature allowing for the calculation of the corresponding *Yrel* and *ECO* data.

The quasi-static approach significantly simplifies the FEA model. In order to capture the resolution needed to compute *Yrel* and *ECO* data, the elements need to be small (one inch length). In addition, a relatively large number of elements are needed to capture realistic track features. Therefore, the quasi-static simplification is expected to significantly decrease computation time compared with a dynamic model.

5.1.4 Model Parameters & Visual Representation

The FEA model is visually represented by the diagram shown in Figure 5-4. Deflections occur along the *y* direction while the track extends along the *x* direction.

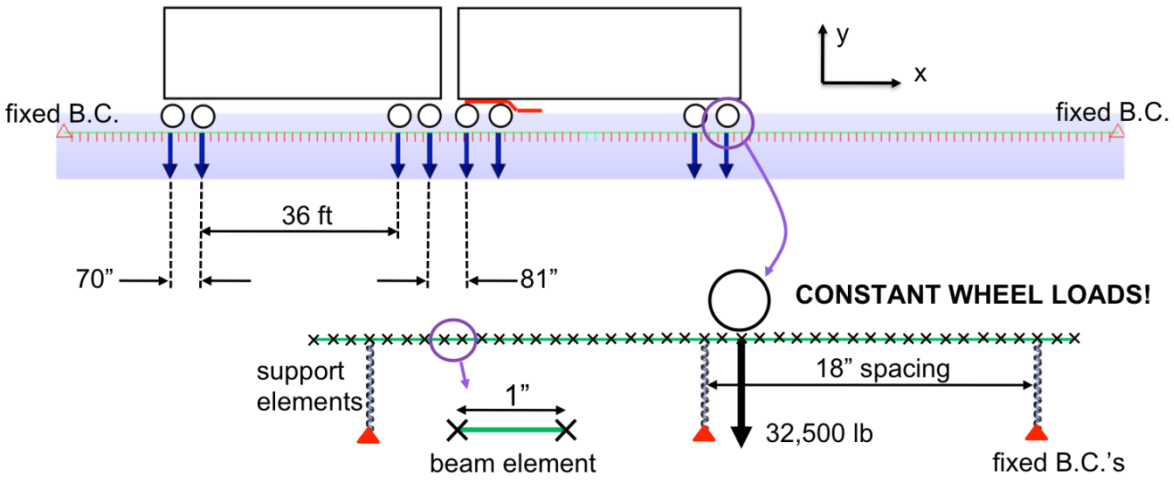

Figure 5-4. Visual diagram of FEA model.

Each beam element is one inch in length. The element length was chosen through experimentation to ensure a fine enough resolution in the deflection curve to capture short-wavelength peaks in the *Yrel* and *ECO* data. The model encompasses 193.5 ft of track resulting in a total of 2,322 beam elements. This length makes certain that the loads are applied far enough away from the boundaries so that the fixed boundaries do not influence the deflection results. The beam element properties represent the 132 RE rail often found on heavy-haul coal lines as shown in Figure 5-5.

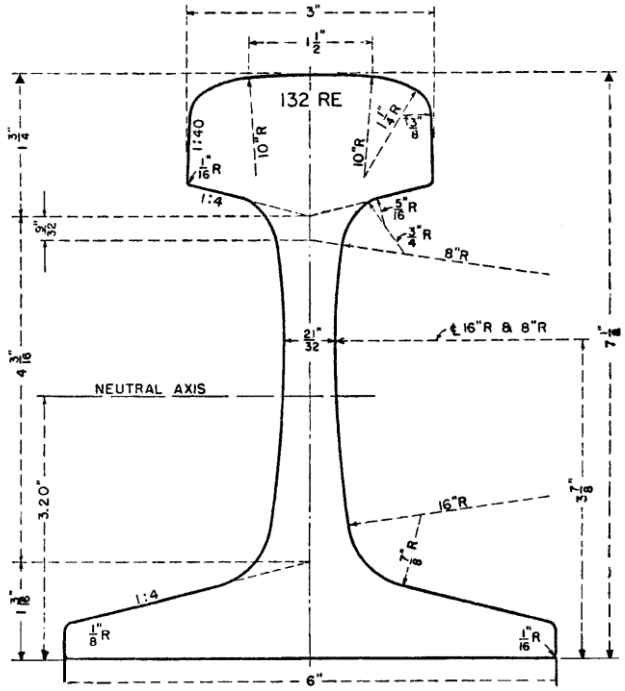

Figure 5-5. 132 RE rail section properties.

The static loads are configured to represent two adjacent hopper cars with the dimensions displayed in Figure 5-4. Constant load magnitudes of 32,500 lbs are applied for each static load. In order to collect enough data to traverse typical track features, 72 static load groups are applied. The loads are translated 12" between each cycle. Therefore, the closest any load will be to a fixed-end boundary is 60 ft.

The support elements shown in Figure 5-4 are located 18” apart to simulate the tie spacing of real track. Stiffness, rather than modulus, is defined in the FEA model. In order to simulate the correct stiffness, the desired modulus is multiplied by the distance between the support elements. The support stiffness for the beam elements between the support elements is set to zero. Each support element can have a unique stiffness value along the track.

The custom FEA program written in MATLAB® is applicable for linear elements only. More complicated nonlinear support elements and support elements used to represent voids are simulated in the commercial FEA software, ALGOR®. The advantage of the custom FEA program is a significant reduction in computation time as well as automatic calculation and plotting of the *Yrel* and *ECO* results for each simulation. When ALGOR® is used for a simulation, the deflection results must be manually exported to text files. These text files are then imported into MATLAB® for the analysis of *Yrel* and *ECO*. The overall process is much less cumbersome with the custom program.

All of the parameters defined in Figure 5-4 are adjustable within the custom FEA program. The element dimensions, element properties, load magnitudes, and support stiffness can all be varied between individual simulations. A schematic of all possible simulation variables and combinations using either the custom FEA program or ALGOR® is illustrated in Figure 5-6.

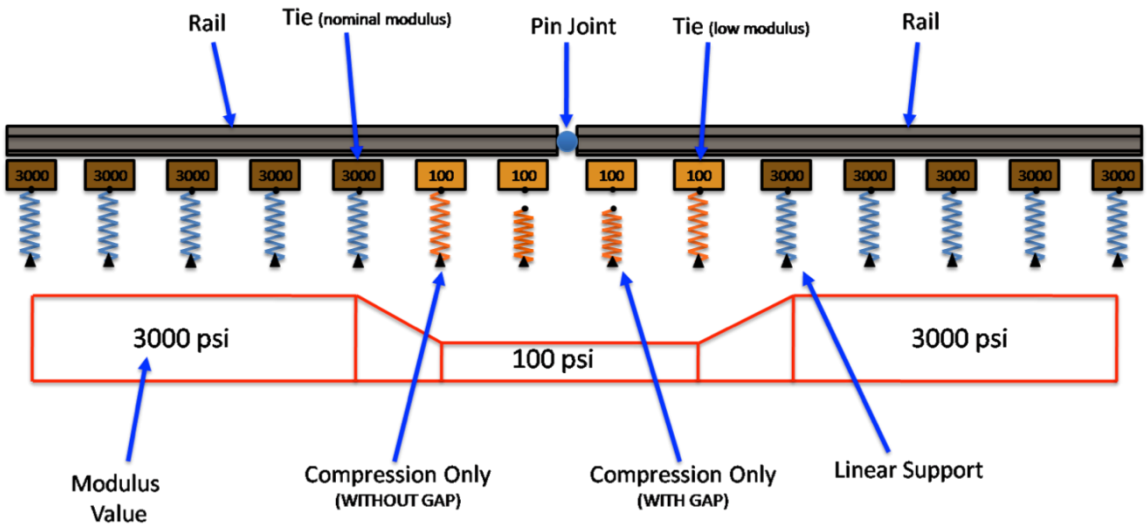

Figure 5-6. Schematic representation of model input variables.

The diagram in Figure 5-6 illustrates all of the simulation possibilities but does not characterize one particular simulation. This type of diagram is used to visualize each simulation in the sections that follow. The blue springs signify linear stiffness elements. The dark brown ties correspond to a nominal modulus of 3000 psi while the lighter ties indicate areas with a softer supporting foundation. The orange springs represent nonlinear support elements. The gaps between some of the springs and ties denote areas of track with voids where some deflection occurs before the foundation provides support. The modulus profile is shown at the bottom of the figure with the specific values listed.

Another feature that can be included in the model is the pin joint shown in Figure 5-6. This element represents a joint that transfers shear forces but cannot transfer any bending moment. The pin joint is modeled using a feature known as a "beam end release" in ALGOR®. In the custom FEA program, the pin joint is modeled by creating a very small beam element (1.0E-10"). Then, the flexural modulus and stiffness for this element are set to zero. The deflection of the nodes are kept equal by assigning a large value (1.0E+12) to the (1,1), (1,3), (3,1), and (3,3) elements of the $[S_1]$ beam-element matrix.

The other values in the $[S_1]$ matrix are set to zero, which allows the slopes of the adjoining elements to be decoupled. This procedure is outlined in (Thompson, 2005).

5.2 Verification of FEA Model

Before proceeding with more complicated simulations, the finite element programs are verified by comparing them with the traditional Winkler model. First, the simulation of a single load in the custom FEA program is compared with the Winkler model as illustrated in Figure 5-7. In this case, a 32,500 lb load was exerted on a foundation modulus of 3,000 psi. As shown by the main figure and in the enlarged inset, the FEA results closely match the Winkler model.

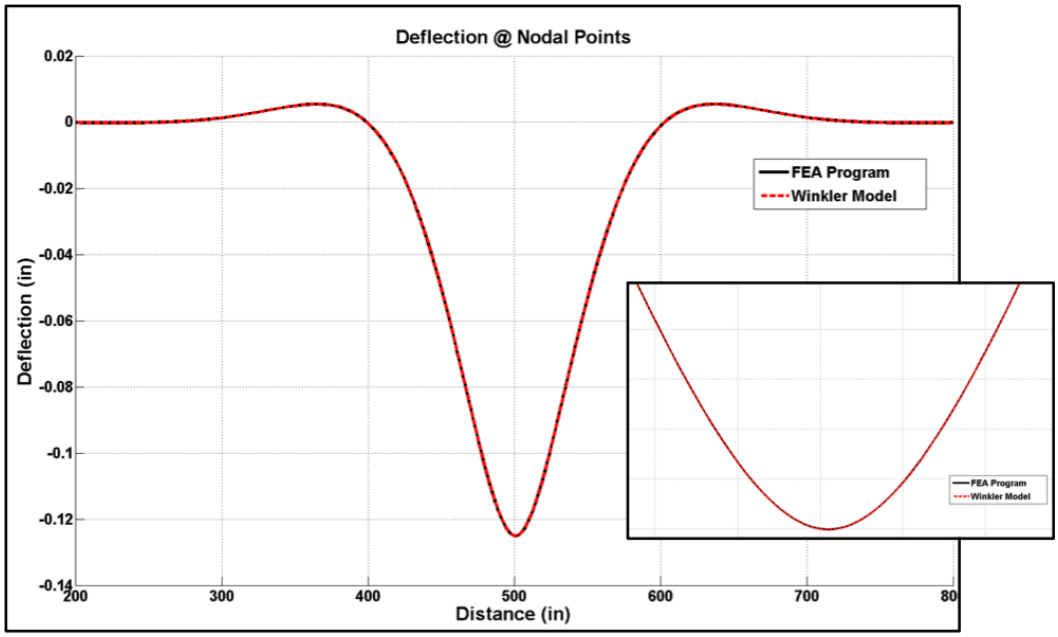

Figure 5-7. Single-load simulation with FEA program compared to Winkler model.

Next, two 32,500 lb loads were simulated in the custom FEA program, representing adjacent axles of a hopper car. Again, the results correspond very well with the deflections found using the Winkler model as displayed in Figure 5-8.

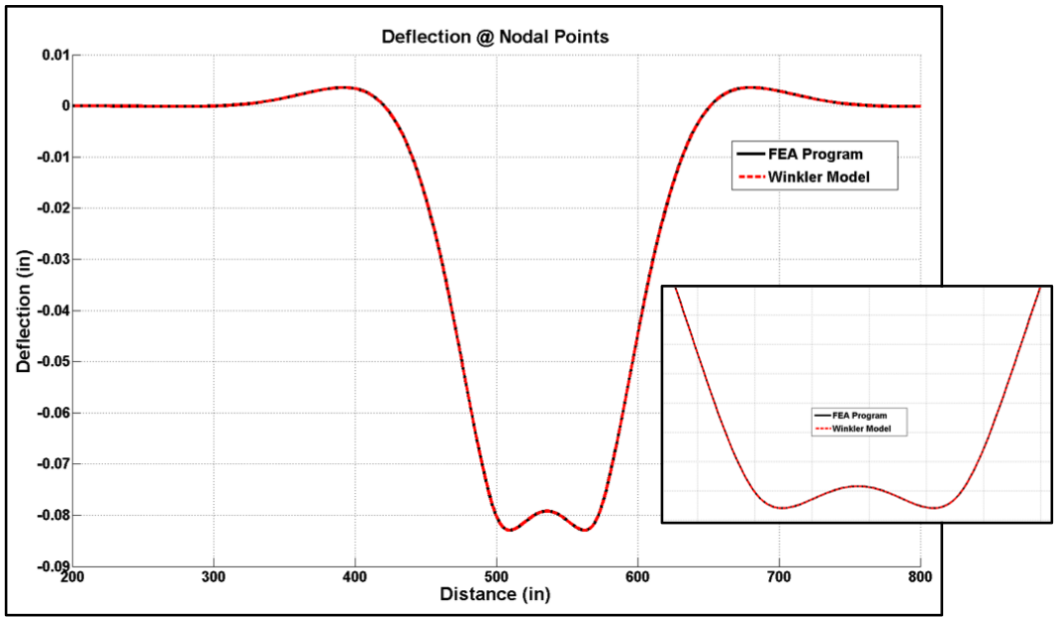

Figure 5-8. Two-load simulation with FEA program compared to Winkler model.

Verification of the custom FEA program's more advanced features is not possible using the Winkler model. For example, the Winkler model is unable to simulate varying modulus, pre-existing geometry, or joints in the rail. However, these features are precisely why the model was created. More complex simulation results are presented in the following section.

Another simulation was performed using the commercial FEA software ALGOR® and the results compared with the Winkler model. In this case, nonlinear gap elements, rather than linear elements, were used as the supporting elements in the foundation. These elements provide linear support in compression only and cannot be loaded in tension. The effect is that the foundation does not "pull down" on the rail in the areas where the track lifts up from the foundation. The results of the simulation are shown in Figure 5-9.

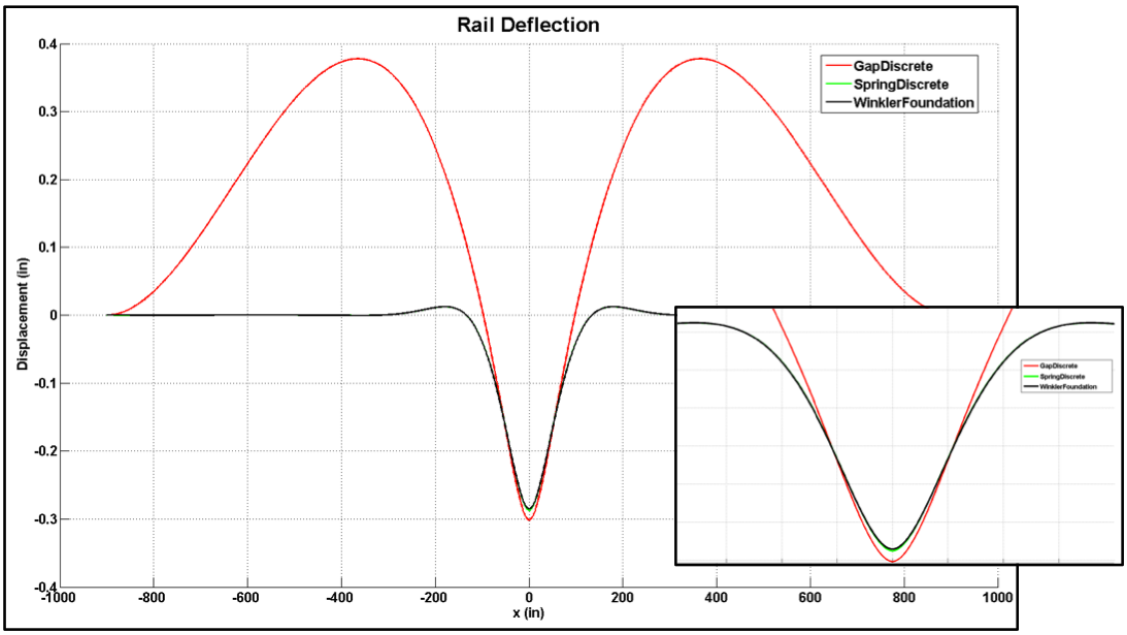

Figure 5-9. Gap element simulation in ALGOR® compared to Winkler model.

Within the vicinity where the load is applied, the results match closely with the Winkler model. However, beyond approximately 5 ft on either side of the load, the track lifts up with a much steeper slope than in the Winkler model. An important fact to note is that the weight of the rail has not been included in this simulation. Rather the simulation was completed to observe how the nonlinear gap elements compare with a linear foundation. Due to the slightly larger peak deflection and the increased track lift, more advanced simulations using these elements are expected to yield different *Yrel* and *ECO* results. Simulations using these elements are described in the following section.

5.3 FEA Analysis & Results

This section describes several simulations performed with the custom FEA program written in MATLAB® as well as some nonlinear simulations performed in ALGOR®. The purpose of each simulation is to examine how a particular track feature, or combination of features, affects the shapes and magnitudes of *Yrel* and *ECO* data. For

example, which combination of features might lead to the differences in measured data found in Figure 5-1? The features simulated include pin joints, soft foundation support, pre-existing geometry, voids, and several combinations of the parameters.

5.3.1 Pin Joint

The custom FEA program was used to simulate a single pin joint as illustrated in Figure 5-10. In this case, the pin joint transfers shear loads but not bending moments. Therefore, this model represents the properties of a failing joint (Kerr, 2003). The foundation is modeled using linear support elements with a modulus of 3,000 psi. The length of the model is not represented in the diagram of Figure 5-10 or any of the other simulation schematics to follow. These diagrams are for visualization purposes only.

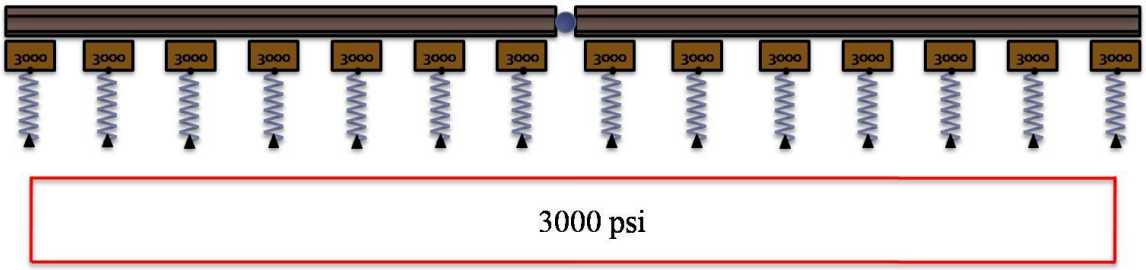

Figure 5-10. Schematic of FEA model with pin joint.

As mentioned earlier, the custom FEA program loops through a series of static loads in order to obtain the data needed to compute *Yrel* and *ECO*. The nodal deflections due to each load are plotted in individual frames and compiled into a movie for visualization as shown in Figure 5-11. The movie illustrates the loads moving from right to left along the track and plots the *Yrel*, *ECO*, and loaded-profile curves. The *Yrel* data is computed from the instantaneous rail deflection while the *ECO* data is determined from the loaded profile. The loaded profile is calculated from the deflection of the leading axle (the inboard axle beneath the red beam on the UNL hopper car).

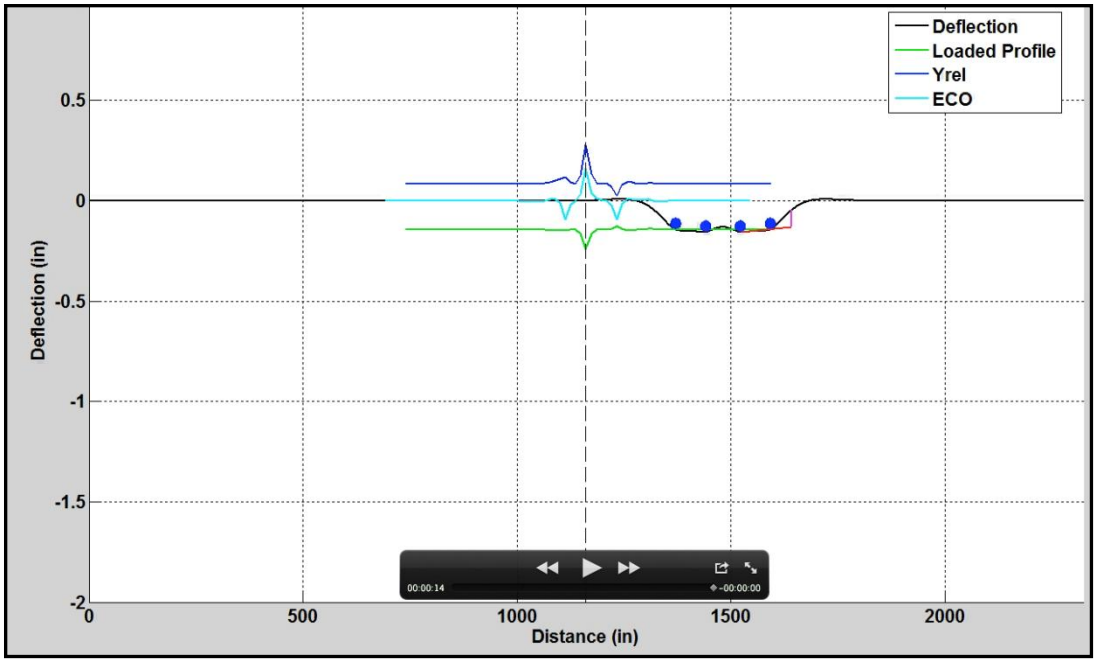

Figure 5-11. Movie frame from FEA simulation with pin joint.

The final *Yrel* and *ECO* results are shown in Figure 5-12. The ratio of *ECO* to *Yrel* is 0.54 with a maximum *Yrel* peak of 0.25" and the maximum *ECO* at 0.15". The shapes of each curve closely match those measured in the field by the UNL system.

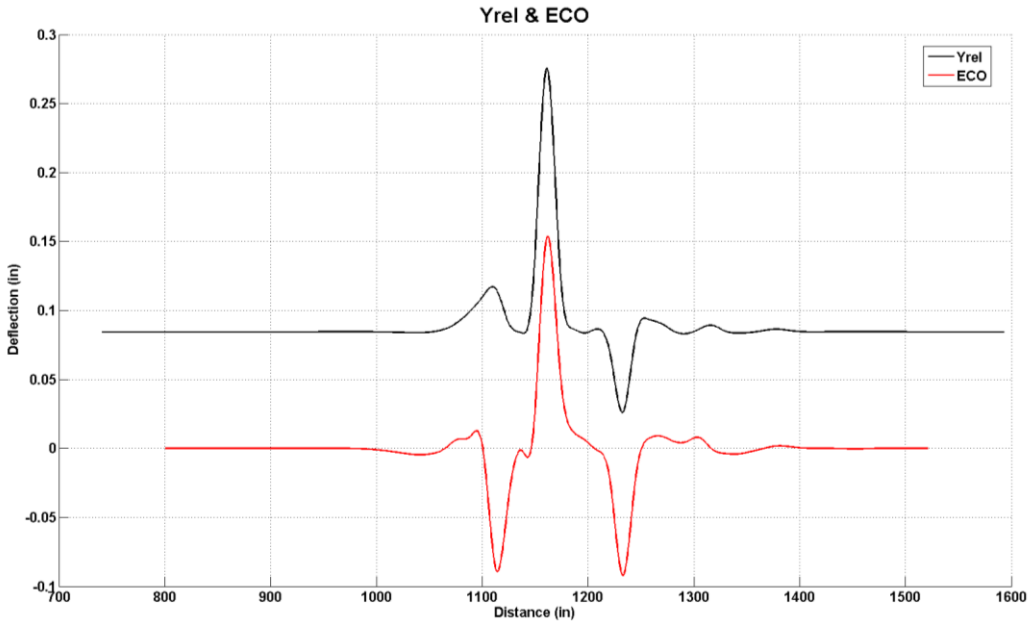

Figure 5-12. *Yrel* and *ECO* results from FEA simulation with pin joint.

The results in Figure 5-12 reveal an interesting point concerning failing joints. Field measurements with the UNL system include large *Yrel* peaks (one inch or more) at the location of very poor joints. Certainly, a joint that does not transfer any bending moment would be considered to be in very poor condition. However, this feature alone did not produce the magnitude of peak expected. In order to analyze this phenomenon further, the following simulation was completed.

5.3.2 Pin Joint with Bad Ties

The custom FEA program was again used to simulate a pin joint but with the addition of two poorly supported ties. The linear foundation support was reduced to 100 psi for each tie on either side of the joint as displayed in Figure 5-13.

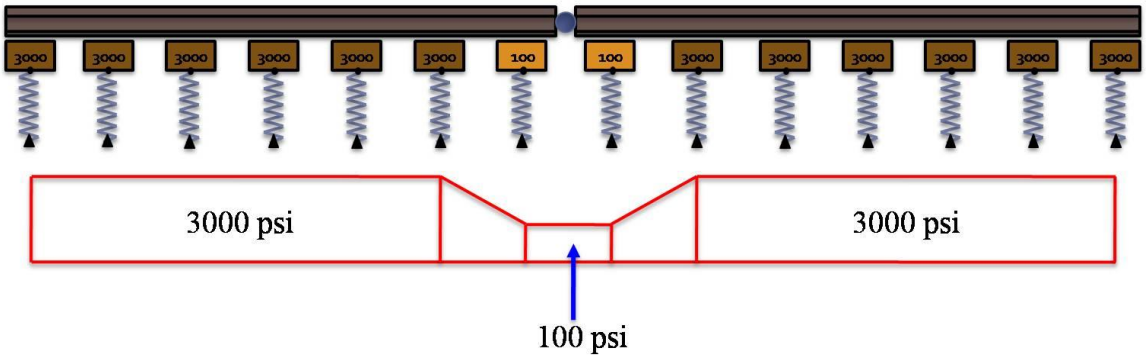

Figure 5-13. Schematic of FEA model with pin joint and two bad ties.

As before, a movie was plotted during the simulation to visualize the results. The movie frame shown in Figure 5-14 was plotted shortly after the leading axle traversed the pin joint. This image reveals the usefulness of the custom FEA program. The deflection of each axle is apparent in the movie along with the chord used to compute *Yrel*. The image provides a way to correlate the axle deflections and *Yrel* chord with the *Yrel* and *ECO* data for a particular location.

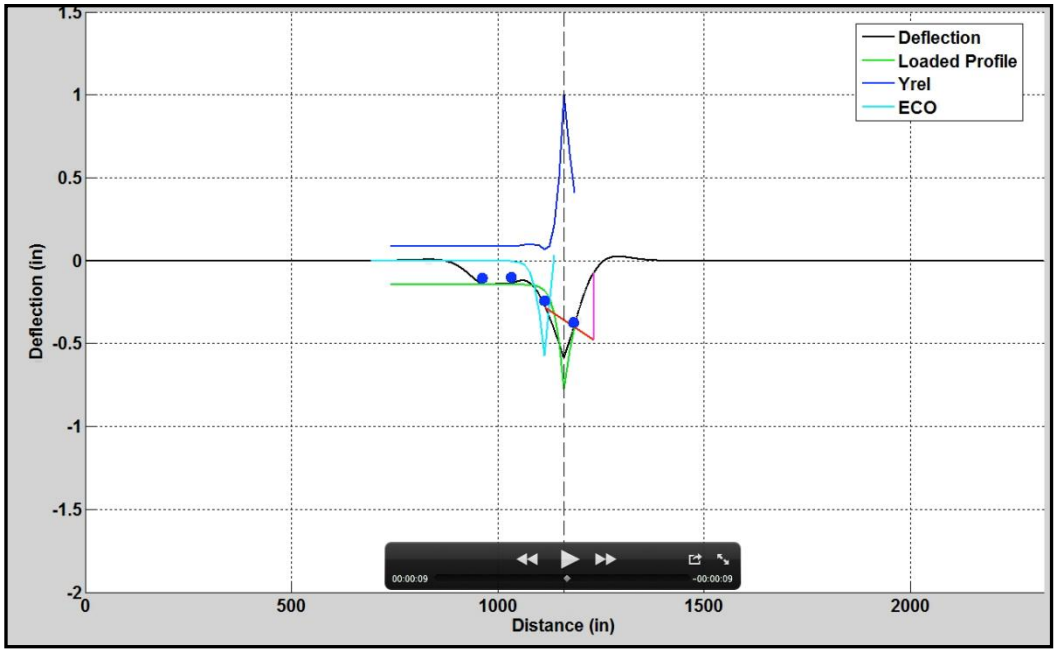

Figure 5-14. Movie frame from FEA simulation with pin joint and two bad ties.

The final *Yrel* and *ECO* results are shown in Figure 5-15. The ratio of *ECO* to *Yrel* is 0.91 with the maximum *Yrel* peak at 1.0" and the maximum *ECO* peak at 0.91". Obviously the addition of two poorly supported ties around the joint led to significantly higher peaks in the *Yrel* and *ECO* data. The sharpness and magnitude of the *Yrel* peak is similar to data measured in the field at the location of failing joints. However, the peak in *ECO*, which nearly matches the one in *Yrel*, is not always expected as displayed in the bottom portion of Figure 5-1. In fact, as described in earlier chapters, pre-existing geometry is expected to be the main contribution in the calculation of *ECO*. Yet, this simulation did not include any geometry effects. This result is discussed in more detail at the end of the section.

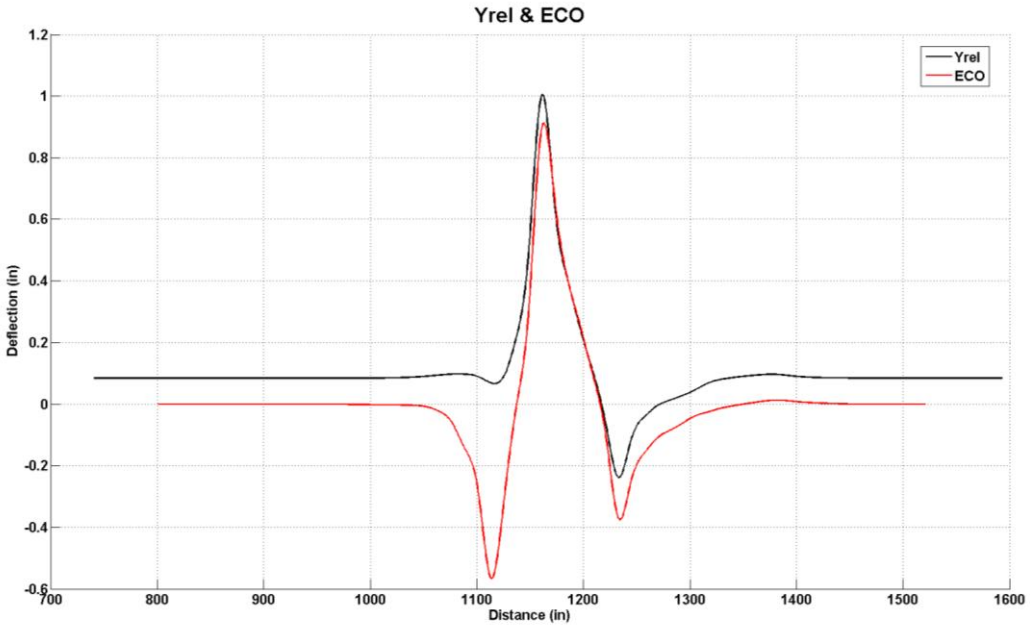

Figure 5-15. *Yrel* and *ECO* results from FEA simulation with pin joint and two bad ties.

5.3.3 Pin Joint with Voids

The complexity of the simulation is further increased with the inclusion of voids and nonlinear elements as shown in Figure 5-16. The voids and nonlinear elements are modeled with gap elements in ALGOR®. The size of each void is listed beneath the corresponding element in Figure 5-16. A maximum void of one inch occurs beneath the pin joint. The support modulus is also slowly decreased to a minimum beneath the joint.

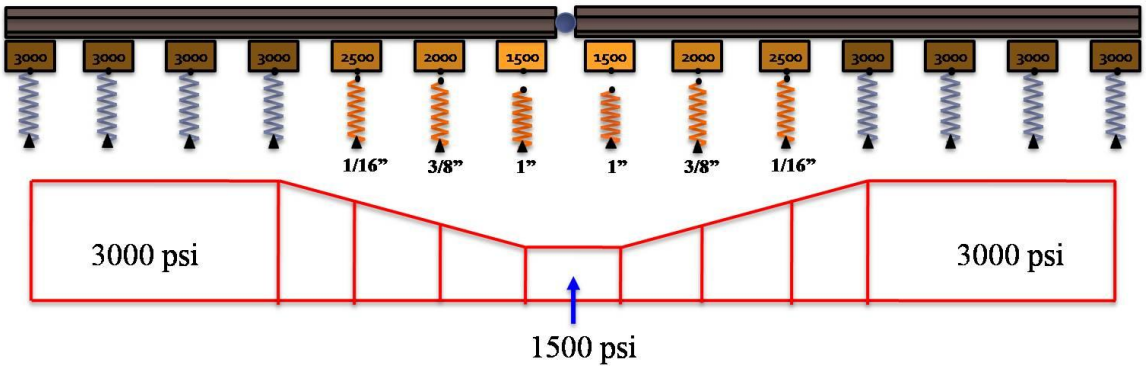

Figure 5-16. Schematic of FEA model with pin joint, bad ties, and voids.

The use of gap elements prevents the foundation from "pulling down" on the track where it lifts up from the foundation. The configuration of the gap elements with voids leads to a nonlinear deflection curve as shown in Figure 5-17. This sort of nonlinear deflection curve is similar to the one measured by (Zarembski & Choros, 1980) and displayed in Figure 2-5. Despite the traditional use of linear models, the actual response of the track is expected to be somewhat nonlinear (Sussman et al., 2001; Lu, 2008). The response shown in Figure 5-17 represents the softer support associated with the seating load followed by the stiffening of the track as the various components compress together.

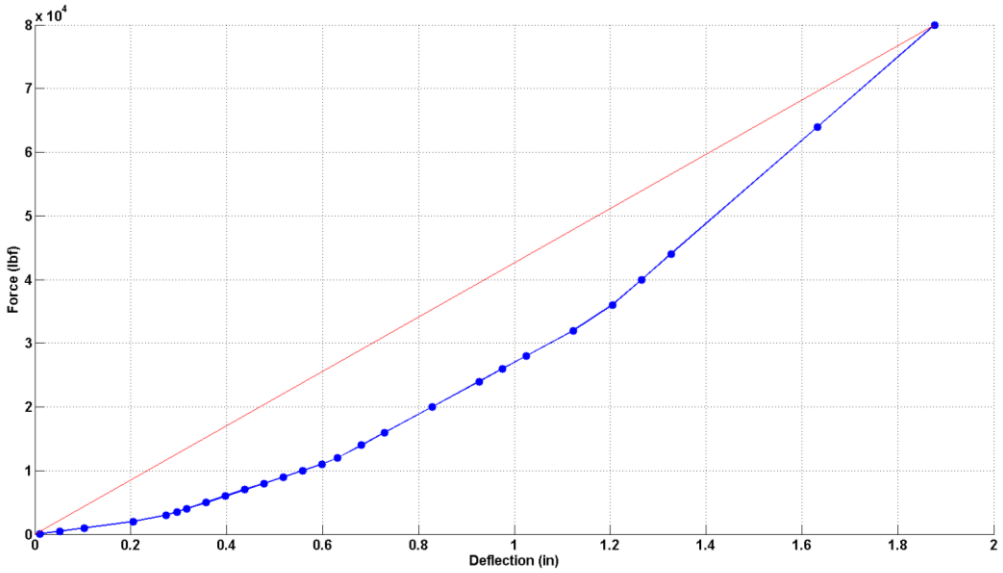

Figure 5-17. Nonlinear deflection curve for FEA model with voids.

The final *Yrel* and *ECO* results are shown in Figure 5-18. The ratio of *ECO* to *Yrel* is 0.93 with the maximum *Yrel* peak at 1.4" and the maximum *ECO* peak at 1.3". The decrease in support led to an increase in the *Yrel* peak as might be expected. However, the ratio between *Yrel* and *ECO* remained essentially the same. Therefore, the

discrepancy between *Yrel* and *ECO*, found in real measured data and shown in the bottom of Figure 5-1, must result from some other effect not yet present in the simulations.

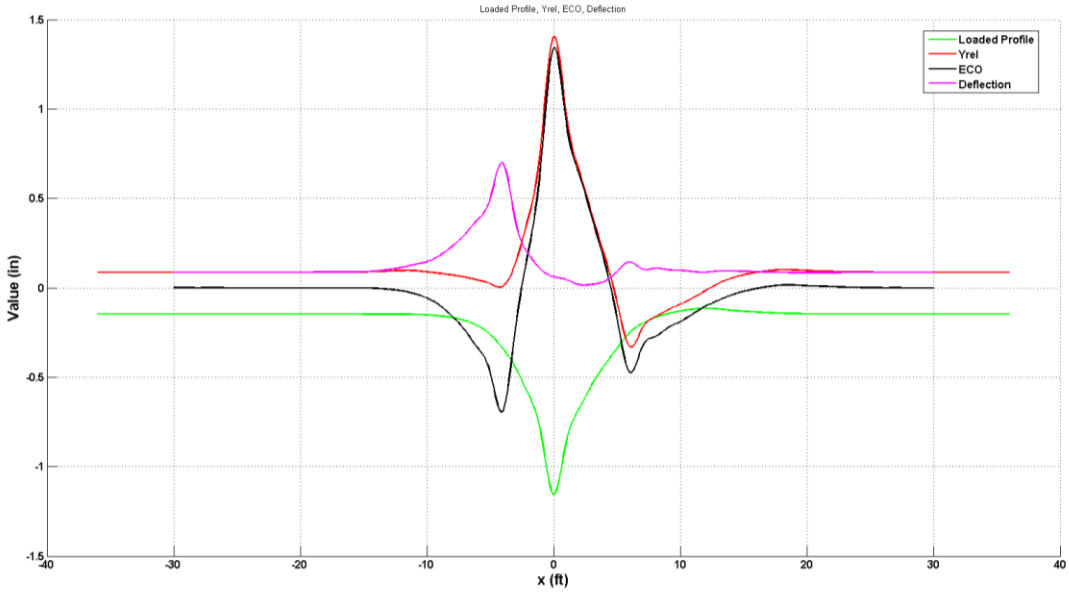

Figure 5-18. *Yrel* and *ECO* results from FEA simulation with pin joint, bad ties, and voids.

5.3.4 Pre-Existing Geometry

In order to study how pre-existing geometry influences *Yrel* and *ECO* data, a one-inch rise over 30 ft was simulated in the track as displayed in Figure 5-19. Again, the diagram is not drawn to scale. The foundation modulus was kept constant at 3,000 psi.

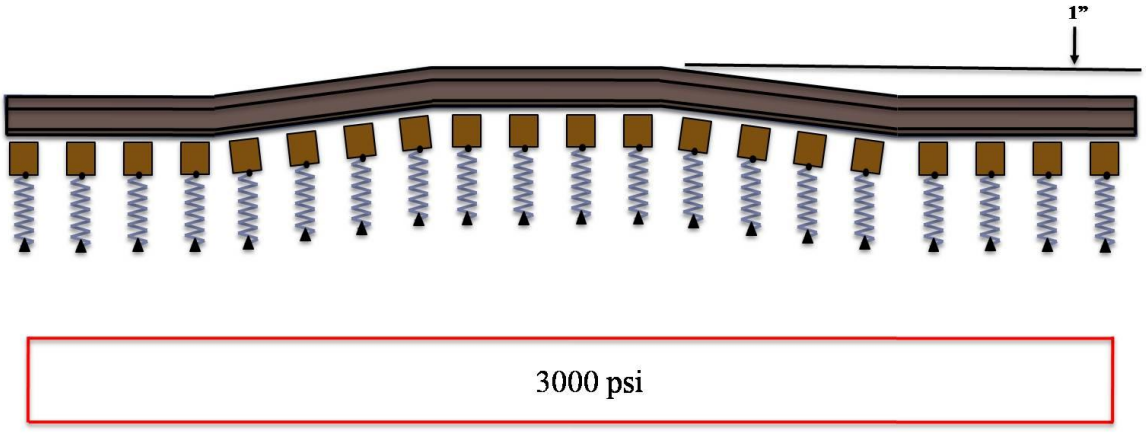

Figure 5-19. Schematic of FEA model with pre-existing geometry.

The final *Yrel* and *ECO* results from the simulation are shown in Figure 5-20. The ratio of *ECO* to *Yrel* is 0.8 with the maximum *Yrel* at 0.46" and the maximum *ECO* at 0.37". The data is symmetric about the geometry feature. The geometry was created with two sloped and one horizontal track segments as shown in Figure 5-19. These regions are evident in the data as both the *Yrel* and *ECO* curves peak as the loads move into and out of the sloped regions.

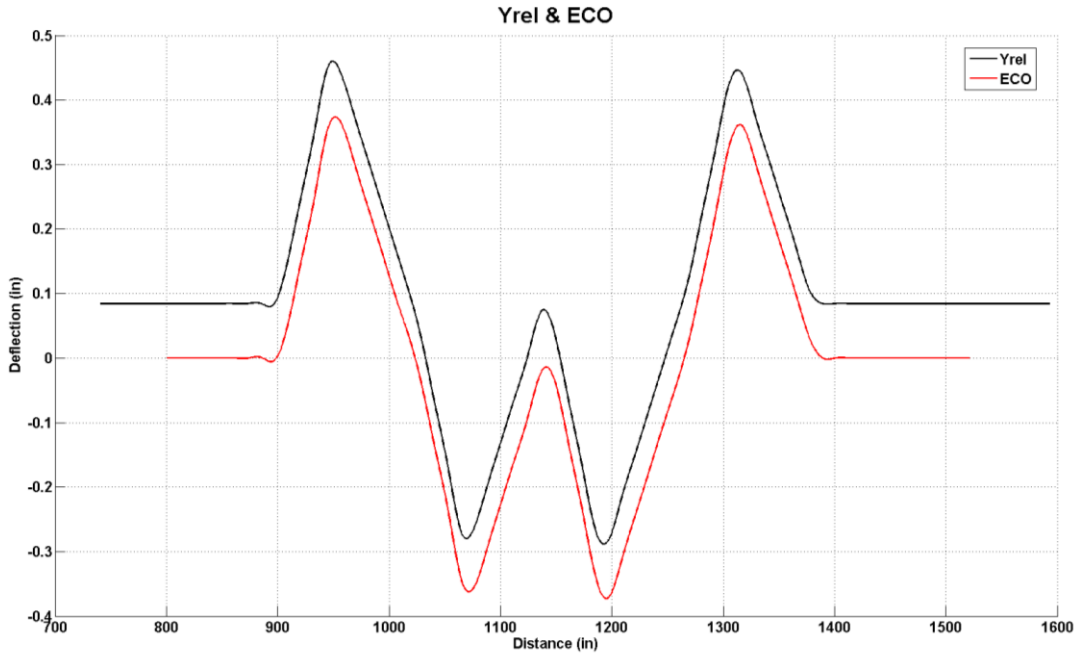

Figure 5-20. *Yrel* and *ECO* results from FEA simulation with pre-existing geometry.

The simulation results verify that relatively short wavelength geometry can affect the *Yrel* measurement. As shown in Figure 5-20, the *Yrel* and *ECO* data match very closely. Therefore, these results also validate the method of eliminating the effect of pre-existing geometry as described in section 3.1.3. Since both curves are nearly the same, subtracting *ECO* from *Yrel* should remove the geometry component in the *Yrel* measurement. However, the interaction between these two measurements with respect to

modulus and geometry is complex. For example, *ECO* closely matches *Yrel* in the other simulations as well despite the absence of pre-existing geometry.

5.3.5 Large Mud Hole

The last simulation is completed to examine the effect of poor support over an extended region of track. The diagram for this simulation is shown in Figure 5-21. In this case, 10 ties have a reduced support modulus of 250 psi.

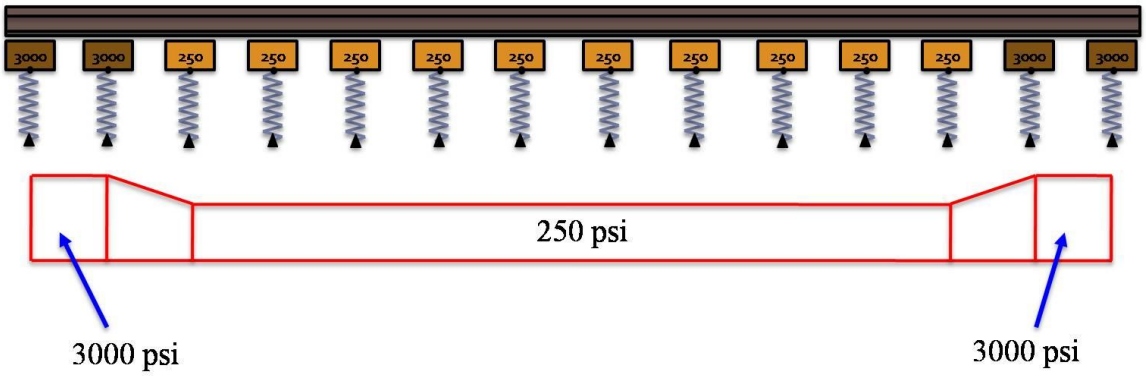

Figure 5-21. Schematic of FEA model with 10 bad ties.

The *Yrel* and *ECO* results from the simulation are shown in Figure 5-22. The ratio of *ECO* to *Yrel* is 0.91 with the maximum *Yrel* at 0.53" and the maximum *ECO* at 0.48". Wider peaks in the data result from the long section of low support modulus. Of particular interest is that the *ECO* peak is shifted with respect to the *Yrel* peak. This effect is present in all simulations when the section of low support modulus is longer than the 10 ft chord used to calculate *Yrel* and *ECO*.

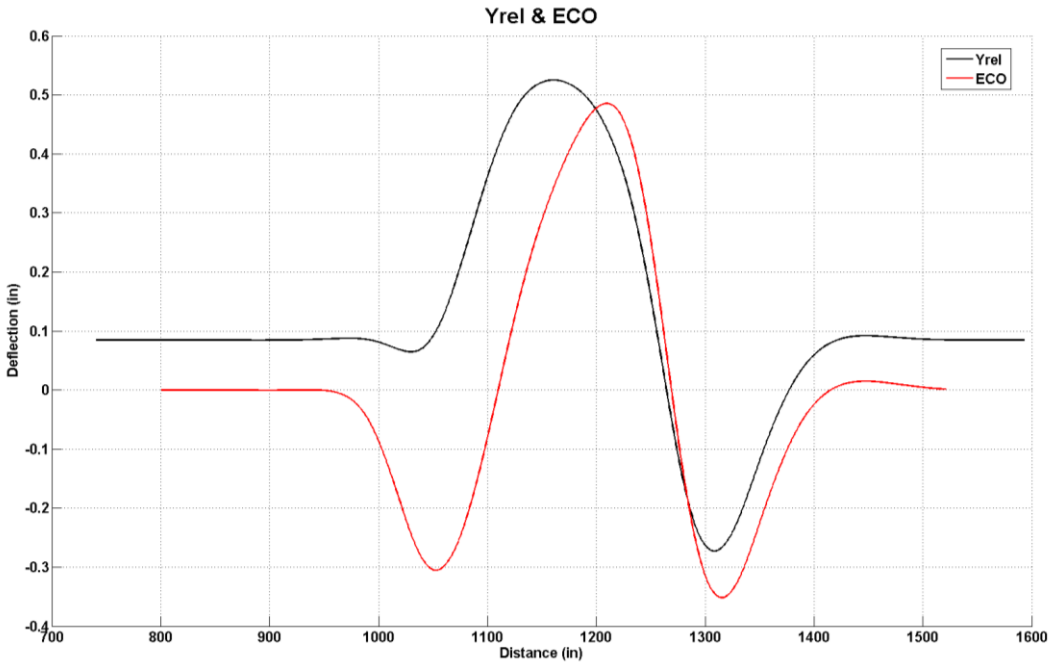

Figure 5-22. *Yrel* and *ECO* results from FEA simulation with 10 bad ties.

5.4 Suggestions For Further Development

The results from all of the simulations discussed in the previous section are displayed in Table 5-1 below.

Table 5-1. Results of FEA simulations.

Simulation Scenario	Yrel (in)	ECO (in)	Ratio: ECO/Yrel
Pin joint only (linear elements)	0.28	0.15	0.54
Pin joint with two, 100 psi modulus ties on each side (linear elements)	1.0	0.91	0.91
Pin joint with 1” gap between joint and supporting foundation	1.4	1.3	0.93
Continuous rail with pre-existing geometry (3,000 psi modulus)	0.46	0.37	0.8
Continuous rail with 10 ties of 250 modulus (linear elements)	0.53	0.48	0.91

The simulation results provide good insight into how specific track features might affect the shape and magnitude of *Yrel*. Of particular interest, however, is that the *ECO* data nearly matched the *Yrel* values in each case. This effect is certainly observable in real measured data with the UNL system. Yet, these results do not indicate why certain track features lead to large peaks in *Yrel* with much smaller peaks in *ECO* as shown in the lower portion of Figure 5-1. Therefore, some parameter or combination of parameters present during the actual measurement of this data is not represented in the simulations.

Considering how the FEA model is created in comparison to how the real *Yrel* and *ECO* data is measured may provide a basis for further development of the simulations. The most obvious discrepancy is the exclusion of dynamic interactions between the measurement vehicle and the deflection of the track. Dynamic effects were not included in the model to reduce its complexity and corresponding computation time. However, previous research has shown that at higher speeds, the dynamics should be included in the model (Carr, 1999). Since the measurement vehicle travels up to revenue speeds, the missing dynamics may be the reason that the data shown in the bottom portion of Figure 5-1 could not be reproduced. The dynamic response of *Yrel* and *ECO* to short wavelength perturbations may be different, leading to the missing peak in the *ECO* data. Therefore, it is recommended that further development of these FEA simulations should include the dynamics of the railcar interacting with the deflection of the track.

Another possible contribution to the discrepancy between *Yrel* and *ECO* peaks may be in the method with which *ECO* is calculated. The *ECO* measurement is

calculated from space curve data provided to UNL from track geometry vehicles. Track geometry vehicles use multiple high-precision accelerometers to measure geometric properties of the track. The vertical accelerations can be integrated to determine the vertical rail profile. This profile is then used to calculate the 10-ft *ECO*.

The method with which *ECO* is calculated raises the possibility that sampling and frequency issues may result in missing data peaks for short-wavelength track features. The accelerometers used to measure the rail space curve have a specific sampling rate. This data is then filtered to remove low frequency (<0.3 Hz) and high frequency (>60 Hz) noise. The resulting signal is then integrated, filtered, and integrated again to obtain the vertical displacement of the rail profile. Finally, the *ECO* data is computed from the resulting space curve profile. This procedure may result in lower peaks of *ECO* than *Yrel* at the location of short-wavelength track perturbations such as failing joints.

In order to study how the real computation of *ECO* compares with the *ECO* measurement found in the simulations, accelerometers have been added to the UNL system as described in Chapter 3. These accelerometers are mounted to the bearing adapters above the inboard axle (axle 3 of the UNL car) and are displayed in Figure 3-11. These accelerometers have been used in a few tests, but as of yet, have not produced conclusive results. Ongoing development is underway to match the UNL accelerometer output with data provided by track geometry vehicles. The goal is that these instruments will eliminate the need for data provided by the track geometry vehicles and verify the computation of *ECO* used in the UNL deflection measurement system.

Chapter 6, CONCLUSION

The increased demands placed on the railway industry have led to a corresponding increase in railroad traffic volumes, speeds, and axle loads. As a result, the need for improved maintenance methods and a better understanding of the mechanical response of railroad track is higher than ever before. Over the past few decades, measurement technology and analytical models have improved dramatically but some pieces of the puzzle have remained missing.

In recent years, UNL has developed a system to measure the vertical deflection of the railroad track in real-time from a vehicle traveling at revenue speeds. Previous research has already shown that the vertical track deflection provides an excellent tool for track maintenance. However, this thesis reveals recent updates to the UNL system and how it is also capable of estimating the actual bending strain in the rail in real-time continuously over long distances.

The UNL system establishes three points of the rail shape beneath the loaded wheels and over a distance of 10 ft. The direct measurement of the rail shape can then be mapped into rail bending strain through curvature of the rail and beam theory. Field tests were conducted on the UPRR's Yoder subdivision to verify this relationship. Bondable resistance strain gages were mounted to the lower rail flange at several locations. The track was then loaded as the UNL car traversed these locations at various speeds. The unloaded and loaded profiles were recorded with surveying instruments and the

relationship between the UNL deflection measurement and rail bending strain was then verified.

The field test results show a strong correlation between the strain calculated from the UNL deflection measurement and the strain gage data. The differences of 13.7% and 12.2% found at two different test sites are well within the modeling errors of the measurement and the error present in the field tests. Misalignment of the strain gage axes and the inability to park the UNL car exactly above the strain gages may have led to the lower measured values at both test sites.

In order to improve the UNL system's capacity as a maintenance tool, an enhanced understanding of how its measurement relates to specific track features is required. Finite element analyses have been used to characterize the mechanical response of the railroad track from the perspective of the UNL measurement system. The resulting simulations have revealed how certain track features influence the shapes and magnitudes of *Yrel* and *ECO* data found with the UNL method. Although these simulations have been useful, specific exception locations displaying large *Yrel* peaks and low *ECO* peaks have not been reproduced. Therefore, some parameters or combination of parameters present in the actual measurement are missing in the simulations. Further developments of the FEA models include recommendations to add the railcar and track dynamic features. The method used to determine the rail space curve may also influence the lower peaks of *ECO* data and is worth additional examination.

APPENDIX

The code from the custom FEA program is included in this appendix. The code is divided into four files: `FEM.m`, `INITIAL.m`, `SF.m`, and `sGAUSS.m`. The `FEM.m` file is the main program that controls the program flow, integrates the element matrices, calculates *Yrel* and *ECO*, and plots the results. The `INITIAL.m` file initializes all of the variables. The SF.m file included the shape functions and their derivatives. The `sGAUSS.m` file uses Gaussian elimination to solve the global matrix for the nodal deflections. The weights and points used for the Gaussian quadrature numerical integration scheme are included in a separate text file named `QUAD`, also shown in this appendix. The operation of the code is summarized in the thesis text. Comment lines are included throughout the code for more details regarding the code's execution. This code has been developed as an extension and adaptation from similar FEA codes found in (Thompson, 2005).

A.1 FEM.m

```
%--------------------------
% program FEM.m
%--------------------------
 clear;
 close;
 clc;
 tic
%-------------------------------------------------------------------------
%LOAD QUADRATURE POINTS & WEIGHTS
load QUAD -ASCII
%-------------------------------------------------------------------------

% ----------------------------
% USER-SPECIFIED DISTANCE & INCREMENT
% ----------------------------
ZINCR=12;           %Loading increment in inches
ZDIST=72;           %Total distance moved in feet

count=1;            %Count for movie frames
```

```
for Z=1:(12*ZDIST/ZINCR);

% %$$$$$$$$$$$$$$$$$$$$$$$$$$$$$$$$$$$$$$$$$$$$$$$$$$$$$$$$$$$$$$$$
% %Call Initial to load pre-processing data

  INITIAL

%END OF INPUT DATA
%$$$$$$$$$$$$$$$$$$$$$$$$$$$$$$$$$$$$$$$$$$$$$$$$$$$$$$$$$$$$$$$$$

%/////////////////////////////////////////////////////////
% FORMATION OF STIFFNESS MATRIX and RIGHT HAND SIDE

  for I=1:NUMEL

% ----------------------------
% Initialize Element Variables/Matrices
% ----------------------------
    for J=1:4
      for K=1:4
         S1(J,K)=0.0;
         S2(J,K)=0.0;
       end
       Qe(J)=0.0;
    end

% ----------------------------
% Calculate element coordinate
% information.
% ----------------------------
     Xa = XORD(I);          %x-coordinate of left element node
     Xb = XORD(I+1);        %x-coordinate of right element node
     RL=Xb-Xa;              %length of element
     DxDu=RL/2.0;
     DuDx=2.0/RL;

% -------------------------
% Begin Gaussian Quadrature
% -------------------------
  for J=1:NQPTS
     u  = GPTS(J);          %Gaussian coordinate
     Wt = GWTS(J);          %Gaussian weight

%    --------------------
%    Global coordinate of current Gauss point
     Xg = (Xa+Xb)/2 + (RL/2.0)*u;

% ----------------------------
% INCLUDE COEF.m  (Defines: EIx, Kx, and Qx)
% ----------------------------
%      COEF

%-----------------------------
%Calculate  shape functions wrt
%x at current Gauss point
```

```
%------------------------------
     No(1) = SF(0,1,u);
     No(2) = SF(0,2,u)*(DxDu);
     No(3) = SF(0,3,u);
     No(4) = SF(0,4,u)*(DxDu);

     Nxx(1) = SF(2,1,u)*(DuDx)^2;
     Nxx(2) = SF(2,2,u)*(DuDx)^2*(DxDu);
     Nxx(3) = SF(2,3,u)*(DuDx)^2;
     Nxx(4) = SF(2,4,u)*(DuDx)^2*(DxDu);


% ----------------------------
% Element stiffness matrices
% ----------------------------
    Wt = GWTS(J);

    for K=1:4
        for L=1:4
            S1(K,L)=S1(K,L) + ...
                Wt*Nxx(K)*EIx(I)*Nxx(L)*DxDu;

                S2(K,L)=S2(K,L) + ...
                    Wt*No(K)*Kx(I)*No(L)*DxDu;
        end
        Qe(K)=Qe(K) + Wt*No(K)*Qx(I)*DxDu;
    end
  end

    B = 1.0E+12;
    if NPcode(I)==1 && NPcode(I+1)==1
        S1=zeros(4,4);
        S1(1,1)=B;S1(1,3)=-B;S1(3,1)=-B;S1(3,3)=B;
    end

% --------- Quadrature now complete

%   --------------------------
%   Assemble element matrices
%   into global matrix
%   --------------------------
    K1=2*I-2;
    for K=1:4
      K1=K1+1;
      L1=0;
      for L=K:4
        L1=L1+1;
        SK(K1,L1)=SK(K1,L1) + ...
                  S1(K,L)+S2(K,L);
      end
      RHS(K1) =  RHS(K1) + Qe(K);
    end
   end
%  ---- Global Matrices are assembled
%////////////////////////////////////////////////////////
```

```
% -------------------------
% BOUNDARY CONDITIONS
% -------------------------
  B = 1.0E+06;
  for I=1:NUMNP
   if NPBC(I) == 1 | NPBC(I) == 3
     I1 = 2*I-1;
     SK(I1,1)=SK(I1,1)*B;
     RHS(I1)=LHS(I1)*SK(I1,1);
   end
   if NPBC(I) == 2 | NPBC(I) == 3
     I2=2*I;
     SK(I2,1)=SK(I2,1)*B;
     RHS(I2)=LHS(I2)*SK(I2,1);
   end
  end


% -------------------------
% CALL EQUATION SOLVER
% -------------------------
  LHS = sGAUSS(SK,RHS,NUMEQ,IB);

% LHS=SK\RHS;

% ---------------------------
%extract nodal deflection values only
% ---------------------------
for z=0:length(LHS)/2-1
    DEFLNOD(z+1)=LHS(1+2*z);
end

% ---------------------------
%extract data for loaded profile
% ---------------------------

lp(Z)=DEFLNOD(LAX2+1);

DEFL(Z,:)=DEFLNOD;

lpaxis(Z)=LAX2*LGTHNOM;

% ---------------------------
%extract data for yrel
% ---------------------------

a=LAX2;
b=LAX2-70/LGTHNOM;
c=LAX2+48/LGTHNOM;

Yrel(Z)= -(((5/3)*DEFLNOD(a+1))-((2/3)*DEFLNOD(b+1))-DEFLNOD(c+1));
```

```
% ---------------------------
%extract data for eco
% ---------------------------
if length(lpaxis) > 10*(12/ZINCR) &&...
        length(lpaxis) < (12*ZDIST/ZINCR)-4*(12/ZINCR)
    a_eco=Z-4*(12/ZINCR);
    b_eco=Z-10*(12/ZINCR);
    c_eco=Z;

    ecoR(Z)= -(((5/3)*lp(a_eco))-((2/3)*lp(b_eco))-lp(c_eco));
else
    ecoR(Z)=0;
end

ecoRaxis=lpaxis-48;
ae=LAX2-48/LGTHNOM;
be=LAX2-120/LGTHNOM;
ce=LAX2;

%-------------------------------------------
%Plot Results

% -------------------------
% Define figure axes limits
% -------------------------
    xmin = min(XORD);
    xmax = max(XORD);
    ymin = -1;
    ymax= 1;
%~~~~~~~~~~~~~~~~~~~~~~~~~~~~~~~~~~~~~~~~~~~~~~~~~~~~~~~~~~~~~~~~~~~~~~~~~~~~~~~
%~~~~~~~~~~~~~~~~~~~~~~~~~~~~~~~~~~~~~~~~~~~~~~~~~~~~~~~~~~~~~~~~~~~~~~~~~~~~~~~
%~~~~~~~~~~~~~~~~~~~~~~~~~~~~~~~~~~~~~~~~~~~~~~~~~~~~~~~~~~~~~~~~~~~~~~~~~~~~~~~
%~~~~~~~~~~~~~~~~~~~~~~~~~~~~~~~~~~~~~~~~~~~~~~~~~~~~~~~~~~~~~~~~~~~~~~~~~~~~~~~
    clf;

    f1=figure(1);
    set(f1, 'units','normalized','outerposition',[0.1 0.1 0.8 0.8])

    hold on;

    plot(XORD, DEFLNOD, 'k','LineWidth', 2.0);
    plot(lpaxis, lp, 'g','LineWidth', 2.0);
    plot(lpaxis, Yrel, 'b','LineWidth', 2.0);
    plot(ecoRaxis, ecoR, 'c','LineWidth', 2.0);
    plot([c*LGTHNOM b*LGTHNOM], [DEFLNOD(c+1)-Yrel(Z) DEFLNOD(b+1)],...
        'r', 'LineWidth', 2.0);
    plot([c*LGTHNOM c*LGTHNOM], [DEFLNOD(c+1)-Yrel(Z) DEFLNOD(c+1)],...
        'm', 'LineWidth', 2.0);
    plot([LOCJTS(1) LOCJTS(1)], [-5 5], '--k');


xlim([xmin xmax]);
ylim([ymin ymax]);

a2=a*LGTHNOM;
```

```
% Trailing Car axle 3 arrow
xa = [a2-221 a2-221];
ya = [DEFLNOD(a-221/LGTHNOM)+0.05 DEFLNOD(a-221/LGTHNOM)];
[xaf yaf]=ds2nfu(xa, ya);
annotation('arrow',xaf,yaf, 'LineStyle', 'none', 'HeadStyle',...
    'ellipse', 'HeadWidth', 10, 'HeadLength', 10, 'Color', 'b');

% Trailing Car axle 4 arrow
xa = [a2-151 a2-151];
ya = [DEFLNOD(a-151/LGTHNOM)+0.05 DEFLNOD(a-151/LGTHNOM)];
[xaf yaf]=ds2nfu(xa, ya);
annotation('arrow',xaf,yaf, 'LineStyle', 'none', 'HeadStyle',...
    'ellipse', 'HeadWidth', 10, 'HeadLength', 10, 'Color', 'b');

% UNL axle 1 arrow
xa = [a2-70 a2-70];
ya = [DEFLNOD(a-70/LGTHNOM)+0.05 DEFLNOD(a-70/LGTHNOM)];
[xaf yaf]=ds2nfu(xa, ya);
annotation('arrow',xaf,yaf, 'LineStyle', 'none', 'HeadStyle',...
    'ellipse', 'HeadWidth', 10, 'HeadLength', 10, 'Color', 'b');

%UNL axle 2 arrow
xa = [a2 a2];
ya = [DEFLNOD(a)+0.1 DEFLNOD(a)];
[xaf yaf]=ds2nfu(xa, ya);
annotation('arrow',xaf,yaf, 'LineStyle', 'none', 'HeadStyle',...
    'ellipse', 'HeadWidth', 10, 'HeadLength', 10, 'Color', 'b');

    grid on;
    xlabel('Distance (in)','FontSize', 16.0, 'FontWeight', 'bold');
    ylabel('Deflection (in)','FontSize', 16.0, 'FontWeight', 'bold');
    title('Deflection @ Nodal Points','FontSize', 24.0, 'FontWeight',
'bold');
    legend('Deflection', 'Loaded Profile', 'Yrel', 'ECO');

    h=gca;
    set(h,'FontSize', 16.0, 'FontWeight', 'bold');


    M(count:count+7)=getframe(gcf);
    count=count+8;
%     close;
%~~~~~~~~~~~~~~~~~~~~~~~~~~~~~~~~~~~~~~~~~~~~~~~~~~~~~~~~~~~~~~~~~~~~~~~~~~~~
%~~~~~~~~~~~~~~~~~~~~~~~~~~~~~~~~~~~~~~~~~~~~~~~~~~~~~~~~~~~~~~~~~~~~~~~~~~~~
%~~~~~~~~~~~~~~~~~~~~~~~~~~~~~~~~~~~~~~~~~~~~~~~~~~~~~~~~~~~~~~~~~~~~~~~~~~~~
%~~~~~~~~~~~~~~~~~~~~~~~~~~~~~~~~~~~~~~~~~~~~~~~~~~~~~~~~~~~~~~~~~~~~~~~~~~~~
end

mpgwrite(M,jet,'my_movie.mpg',[1, 0, 1, 0, 10, 1, 1, 1]);

toc
t=toc;
% --------------------------
%Print data to files
```

```
% ---------------------------
fid = fopen('Loaded_Profile', 'w');
fprintf(fid, '%6.5f\n', lp(1,:));
fclose(fid);

fid = fopen('Yrel_Data', 'w');
fprintf(fid, '%6.5f\n', Yrel(1,:));
fclose(fid);

% ---------------------------
%Calculate ECO & Plot with Yrel
% ---------------------------

lpfit=fit(lpaxis', lp', 'cubicsp');

for n = 0:(12*ZDIST/ZINCR)-12*(12/ZINCR);
    a=(START*LGTHNOM+70)+ZINCR*n;
    b=START*LGTHNOM+ZINCR*n;
    c=(START*LGTHNOM+118)+ZINCR*n;

    eco(n+1)= -(((5/3)*lpfit(a))-((2/3)*lpfit(b))-lpfit(c));
end

% ecoaxis=(LAX2-(12/LGTHNOM)*(ZDIST-6)):ZINCR/LGTHNOM:LAX2-
(12/LGTHNOM)*6;

ecoaxis=lpaxis((72/ZINCR):((length(lpaxis))-72/ZINCR));

% lpaxisf=(LAX2-(12/LGTHNOM)*ZDIST):LAX2;

if ZINCR >= 1
    ecoaxisf=ecoaxis(1):0.5:ecoaxis(length(ecoaxis));
    lpaxisf=lpaxis(1):0.5:lpaxis(length(lpaxis));
else
    ecoaxisf=ecoaxis(1):ZINCR:ecoaxis(length(ecoaxis));
    lpaxisf=lpaxis(1):ZINCR:lpaxis(length(lpaxis));
end

yrelfit=fit(lpaxis', Yrel', 'cubicsp');
ecofit=fit(ecoaxis', eco', 'cubicsp');

figure(2)
hold on;
plot(lpaxisf, yrelfit(lpaxisf), 'k','LineWidth', 2.0);
plot(ecoaxisf, ecofit(ecoaxisf), 'r','LineWidth', 2.0);
grid on;
xlabel('Distance (in)','FontSize', 16.0, 'FontWeight', 'bold');
ylabel('Deflection (in)','FontSize', 16.0, 'FontWeight', 'bold');
title('Yrel & ECO','FontSize', 24.0, 'FontWeight', 'bold');
legend('Yrel', 'ECO');
h=gca;
set(h,'FontSize', 16.0, 'FontWeight', 'bold');
```

A.2 INITIAL.m

```
%------------------------------
%          INITIAL.m
%------------------------------

%$$$$$$$$$$$$$$$$$$$$$$$$$$$$$$$$$$$$$$$$$$$$$$$$$$$$$$$$$$$$$$$$$$$$$$$$$$$$

% INPUT DATA

%################################
%BEGIN MESH DATA

%^^^^^^^^^^^^^^^^^^^^^^^^^^^^^^^^^^^^^^^^^^^^^^^^^^^^^^^^^^^^^^^^^^^^^^^^^^^^
%USER-DEFINED DATA

LGTHBM = 2322;        %Overall length of beam
NUMEL = LGTHBM;         %Number of elements
IB = 4;                 %Stiffness matrix bandwidth

LGTHNOM = LGTHBM/NUMEL;  %Length of elements

NJTS=1;                  %Number of Joints
LOCJTS=[1161]/LGTHNOM;          %Location of Joints
LENJTS=1.0E-10;           %Length of Joints


LGTHBM=LGTHBM+LENJTS*NJTS;       %Modified beam length
NUMEL=NUMEL+NJTS;                %Modified # of elements

LGTHEL(1:NUMEL)=LGTHNOM;         %Nominal Element Length

for i =1:NJTS
    LGTHEL(LOCJTS(i))=LENJTS;        %Include any joints
end


%Elastic Modulus of Rail
Exx(1:NUMEL)=30E6;

%Second Moment of Area of Rail Section
Ixx(1:NUMEL)=87.9;

% Element Modulus
Kx(1:NUMEL) = 3000;

%Process any joints
%&&&&&&&&&&&&&&&&&&&&&&&&&&&&&
if NJTS > 0
    for w=1:NJTS
        Exx(LOCJTS(w))=0;
        Ixx(LOCJTS(w))=0;
        Kx(LOCJTS(w))=0;
```

```
    end
end
%&&&&&&&&&&&&&&&&&&&&&&&&&&&&&&

%Derivative
dEIx(1:NUMEL) = 0;

%Distributed Load
Qx(1:NUMEL) = 0;

%Rail Section Stiffness
EIx = Exx.*Ixx;

%^^^^^^^^^^^^^^^^^^^^^^^^^^^^^^^^^^^^^^^^^^^^^^^^

NUMNP = NUMEL+1;         %Number of nodal points
NUMEQ = 2*NUMNP;         %Number of equations


XORD=zeros(NUMNP,1);       %x-coordinate of nodal points
NPcode=zeros(NUMNP,1);     %identifies nodes at joint locations

for i=2:NUMNP
    XORD(i)=XORD(i-1)+LGTHEL(i-1);
    if LGTHEL(i-1) < 1.0E-8
        NPcode(i-1)=1;
        NPcode(i)=1;
    end
end

%END OF MESH DATA
%################################

% ----------------
% Define QUAD Data
% ----------------
  NQPTS = QUAD(1,1);
  for i=1:NQPTS
     GPTS(i)=QUAD(i+1,1);
     GWTS(i)=QUAD(i+1,2);
  end

% ---------------------------
% General initialization
% ---------------------------

LHS=zeros(NUMEQ,1);           %Left-hand side (w and dw/dx)
RHS=zeros(NUMEQ,1);           %Right-hand side (loading)
SK=zeros(NUMEQ,4);          %Global Stiffness Matrix
NPBC=zeros(NUMNP,1);          %Nodal B.C.'s

%---------------------------
%DEFINE B.C.'S
```

```
%                 w     dw/dx
% NPBC(n) = 0     U       U
%         = 1     K       U
%         = 2     U       K
%         = 3     K       K

%where
%K=known
%U=unknown
%---------------------------

NPBC(1) = 3;                % Left node B.C.
NPBC(NUMNP) = 3;            % Right node  B.C.

%---------------------------
%DEFINE LOADS

%Location of AXLE 2
% LAX2=1161;
% START=729;

START=729/LGTHNOM;                  %Starting location of UNL axle 2

% ---------------------------
% Load Increment of UNL Axle 2
% ---------------------------
LAX2=START+(ZINCR/LGTHNOM)*Z;


% RHS(2*(LAX2-723)-1) = -32500;         %axle 1 of trailing car
% RHS(2*(LAX2-653)-1) = -32500;         %axle 2 of trailing car

RHS(2*(LAX2-221/LGTHNOM)-1) = -32500;         %axle 3 of trailing car
RHS(2*(LAX2-151/LGTHNOM)-1) = -32500;         %axle 4 of trailing car

RHS(2*(LAX2-70/LGTHNOM)-1) = -32500;    %axle 1 of UNL car
RHS(2*LAX2-1) = -32500;                 %axle 2 of UNL car

% RHS(2*(LAX2+432)-1) = -32500;         %axle 3 of UNL car
% RHS(2*(LAX2+502)-1) = -32500;         %axle 4 of UNL car
```

A.3 SF.m

```
function s  = SF(D,Fnct,u)
%-------------------------------------------------------------
%/////////////////////////////////////////////////////////////
%-------------------------------------------------------------
%  Shape Functions
%    D = derivative
%      = 0 function itself
%      = 1 first derivative of function
%      = 2 second derivative of function
```

```
%      = 3 third derivative of function
%  Fnct= Shape function number
%    node = shape function number (1, 2, 3, or 4)
%       u = local coordinate
%-------------------------------------------------------------

 if Fnct == 1  % Shape function 1
    if D == 0
       s = (1/4)*(u+2)*(u-1)^2;
    elseif D == 1
       s = (1/4)*(3*u^2-3);
    elseif D == 2
       s = (1/4)*(6*u);
    elseif D == 3
       s = (1/4)*(6);
    end

 elseif Fnct == 2  % Shape function 2
    if D == 0
       s = (1/4)*(u+1)*(u-1)^2;
       s = (1/4)*(1-u^2)*(1-u);
    elseif D == 1
       s = (1/4)*(3*u^2-2*u-1);
    elseif D == 2
       s = (1/4)*(6*u-2);
    elseif D == 3
       s = (1/4)*(6);
    end

 elseif Fnct == 3  % Shape function 3
    if D == 0
       s = -(1/4)*(u-2)*(u+1)^2;
    elseif D == 1
       s = -(1/4)*(3*u^2-3);
    elseif D == 2
       s = -(1/4)*(6*u);
    elseif D == 3
       s = -(1/4)*(6);
    end

 elseif Fnct == 4  % Shape function 4
    if D == 0
       s = (1/4)*(u-1)*(u+1)^2;
    elseif D == 1
       s = (1/4)*(3*u^2+2*u-1);
    elseif D == 2
       s = (1/4)*(6*u+2);
    elseif D == 3
       s = (1/4)*(6);
    end
 end
```

A.4 sGAUSS.m

```
function s  = SF(D,Fnct,u)
```

```
%-------------------------------------------------------------
%/////////////////////////////////////////////////////////////
%-------------------------------------------------------------
%  Shape Functions
%    D = derivative
%      = 0 function itself
%      = 1 first derivative of function
%      = 2 second derivative of function
%      = 3 third derivative of function
%  Fnct= Shape function number
%    node = shape function number (1, 2, 3, or 4)
%       u = local coordinate
%-------------------------------------------------------------

 if Fnct == 1  % Shape function 1
    if D == 0
       s = (1/4)*(u+2)*(u-1)^2;
    elseif D == 1
       s = (1/4)*(3*u^2-3);
    elseif D == 2
       s = (1/4)*(6*u);
    elseif D == 3
       s = (1/4)*(6);
    end

 elseif Fnct == 2  % Shape function 2
    if D == 0
       s = (1/4)*(u+1)*(u-1)^2;
       s = (1/4)*(1-u^2)*(1-u);
    elseif D == 1
       s = (1/4)*(3*u^2-2*u-1);
    elseif D == 2
       s = (1/4)*(6*u-2);
    elseif D == 3
       s = (1/4)*(6);
    end

 elseif Fnct == 3  % Shape function 3
    if D == 0
       s = -(1/4)*(u-2)*(u+1)^2;
    elseif D == 1
       s = -(1/4)*(3*u^2-3);
    elseif D == 2
       s = -(1/4)*(6*u);
    elseif D == 3
       s = -(1/4)*(6);
    end

 elseif Fnct == 4  % Shape function 4
    if D == 0
       s = (1/4)*(u-1)*(u+1)^2;
    elseif D == 1
       s = (1/4)*(3*u^2+2*u-1);
    elseif D == 2
       s = (1/4)*(6*u+2);
    elseif D == 3
```

```
        s = (1/4)*(6);
    end
end
```

A.5 QUAD

```
%-----------------------------------------------
%       Number of points      dummy number
%-----------------------------------------------
        4                     0
%===============================================
%       Coordinates           Weights
%-----------------------------------------------
    -0.861136311594953     0.347854845137454
    -0.339981043584856     0.652145154862546
     0.861136311594953     0.347854845137454
     0.339981043584856     0.652145154862546
%-----------------------------------------------
```

REFERENCES

Cai, Z., Raymond, G. P. & Bathurst, R. J. (1994). Estimate of static track modulus using elastic foundation models. *Transportation Research Record 1470,* 65-72.

Carr, G. A. (1999, September*). Dynamic response of railroad track induced by high speed trains and vertical stiffness transitions with proposed method of measurement.* Tufts University.

Chang, C. S., Adegoke, C. W. & Selig, E. T. (1980, November). GEOTRACK model for railroad track performance. *Journal of the Geotechnical Engineering Division,* 106, No. GT11, 1201-1218.

Ebersöhn, W. & Selig, E. T. (1994). Track modulus on a heavy haul line. *Transportation Research Record 1470,* 73-83.

Ebersöhn, W., Trevizo, M. C. & Selig, E. T. (1993). Effect of low track modulus on track performance. *Proceedings of Fifth International Heavy Haul Conference,* 379-388.

Federal Railroad Administration (2006, August). *Preliminary Evaluation of T-18's Gage Restraint Measurement System Tests*. (Publication No. RR06-11). Retrieved June 7, 2010 from research publication downloads via http://www.fra.dot.gov/downloads/Research/rr06_11.pdf.

Greisen C., Lu, S., Duan, H., Farritor, S., Arnold, A., GeMeiner, W., Clark, D., Toth, T., Hicks, K., Sussman, T., Fateh, M., El-Sibaie, M. "Estimation of Rail Bending Stress from Real-Time Vertical Track Deflection Measurement." *Proceedings of the 2009 IEEE/ASME Joint Rail Conference*, Pueblo, CO, March 3-5, 2009.

Hetényi, M. Beams on Elastic Foundation: Theory with Applications in the Fields of Civil and Mechanical Engineering. Ann Arbor: University of Michigan, 1946.

Hogan, C., (2007, August). *Design of a System to Measure Vertical Railroad Track Deflection From a Moving Railcar and Implementation to Dynamic Railcar Simulation*. University of Nebraska - Lincoln.

Hogan, C., Dick, M., Lu, S., Farritor, S., Arnold, R., GeMeiner, W., Clark, D., "Track Stiffness Measurement with Implementation to Rail/Vehicle Dynamic Simulation." *Proceedings of the AREMA 2008 Annual Conference*, Salt Lake City, UT, September 21-24, 2008

Kerr, A. D. (1964, September). Elastic and Viscoelastic Foundation Models. *Transactions of the ASME, Journal of Applied Mechanics,* pp. 491-498.

Kerr, A. D. & Shenton, H. W. (1985, December). On the reduced area method for

calculating the vertical track modulus. *American Railway Engineering Bulletin,* 86, 416-429.

Kerr, A. D. Fundamentals of Railway Track Engineering. Omaha, NE: Simmons-Boardman Books, Inc., 2003.

Klauser, P. (2007, January). "Vampire Pro New User Training Course Notes." Copyright 2004-2007 Peter Ernst Klauser.

Li, D., Hass, K. & Meddah, A. (2002, June). Moving closer to performance-based track geometry inspection. *Railway Track & Structures*, 15-17.

Lu, S. (2008, December). *Real-Time Vertical Track Deflection Measurement System*. University of Nebraska - Lincoln.

Lu, S., Arnold, R., Farritor, S. (2007). *On the Relationship between Load and Deflection in Railroad Track Structure*. Department of Mechnical Engineering, University of Nebraska - Lincoln.

Norman, Christopher. (2004, May). *Measurement of Railroad Track Modulus from a Moving Railcar*. University of Nebraska - Lincoln.

McVey, B. (2006, May). *A Nonlinear Approach to Measurement of Vertical Track Deflection From a Moving Railcar.* University of Nebraska-Lincoln.

Priest, J.A. & Powrie, W. (2009). Determination of Dynamic Track Modulus from Measurement of Track Velocity during Train Passage. *Journal of Geotechnical & Geoenvironmental Engineering*, 135 (11), 1732-1740.

Selig, E. T. & Li, D. (1994). Track modulus: its meaning and factors influencing it. *Transportation Research Record 1470*, 47-54.

Spotts, M. F., Shoup, T. E. and Hornberger, L. E., Design of Machine Elements, Eighth Edition. Pearson-Prentice Hall, Upper Saddle River, NJ, 2004.

Steele, R. K. and Muhlenberg, J. A. (1992, May). Validation of Rail Fatigue Life, Crack Growth and Deformation Behavior Predications. *Association of American Railroads Report WP-153*.

Steele, R. K. and Joerms, M. W., (1988, September). A Fatigue Analysis of the Effects of Wheel Load on Rail Life. *Association of American Railroads Report R-689.*

Sussman, T. R., Ebersöhn, W. & Selig, E. T. (2001). Fundamental nonlinear track load-deflection behavior for condition evaluation. *Transportation Research Record 1742*, 61-67.

Thompson, Erik G. Introduction to the Finite Element Method: Theory Programming, and Applications. New York: John Wiley & Sons, Inc., 2005.

Thompson, R., and Li, D. (2002, February) Automated Vertical Track Strength Testing Using TTCI's Track Loading Vehicle. *Technology Digest*.

Union Pacific Railroad. "Union Pacific Saves Fuel While Increasing Efficiency." 28 April 2006. 2 June 2010. <http://uprr.com/newsinfo/releases/environment /2006/0428_fuel_economy.shtml>

Zarembski, A. M. & Choros, J. (1980). On the measurement and calculation of vertical track modulus. *Proceedings of the American Railway Engineering Association*, 81, 156-173.